

Ultrafast charge carrier dynamics of ZnO thin films and BaTiO₃-ZnO heterostructures

Dissertation

zur Erlangung des akademischen Grades
doktor rerum naturalium (Dr. rer. nat.)

vorgelegt der

Naturwissenschaftlichen Fakultät II
der Martin-Luther-Universität Halle-Wittenberg



von

Snigdhatanu Acharya

geb. am 24. Januar 1985 in Tezpur, Indien

Gutachter :

- 1. PD Dr. Gerhard Seifert*
- 2. Prof. Dr. Wolf Widdra*
- 3. Prof. Dr. Carsten Ronning*

Verteidigt am: 20th März 2013

Contents

CHAPTER 1 INTRODUCTION	1
CHAPTER 2 GENERALITIES	5
2.1 INTRODUCTION TO SEMICONDUCTORS	5
2.2 INTERACTION OF LIGHT WITH SEMICONDUCTORS	6
2.2.1 Propagation	6
2.2.2 Absorption and emission.....	7
2.2.3 Lifetime of photo-excited states.....	10
2.2.4 High-intensity effects.....	12
2.3 COUPLING OF SEMICONDUCTORS WITH FERROELECTRICS.....	15
CHAPTER 3. SAMPLES PROPERTIES	17
3.1. GENERAL PROPERTIES OF ZNO	17
3.1.1 Structural properties	17
3.1.2 Intrinsic defects in ZnO.....	18
3.2. SALIENT FEATURES OF BaTiO ₃ (BTO) AND THE BTO/ZNO HETEROSTRUCTURE	19
3.2.1 Structural and ferroelectric properties of BTO	19
3.2.2 Defects and doping in BTO.....	20
3.2.3 Physical effects observed in BTO/ZnO heterostructures	20
3.3. FABRICATION AND CHARACTERIZATION OF SAMPLES.....	21
3.3.1 Fabrication of samples via PLD and sample specification	21
3.3.2 Characterization techniques	22
3.4. SAMPLE PROPERTIES.....	22
3.4.1 Crystal structure	22
3.4.2 Surface morphology.....	23
3.4.3 Defect characterization.....	24
3.4.4 Ground state optical properties	25
CHAPTER 4. FEMTOSECOND TIME-RESOLVED SPECTROSCOPY ON ZNO AND BTO/ZNO THIN FILMS	27
4.1 EXPERIMENTAL DETAILS.....	27
4.1.1 Experimental set- up	27

4.1.2 Technical aspects	29
4.1.3 Data Acquisition.....	30
4.1.4 Time-zero and chirp correction.....	31
4.2 ANALYSIS OF TIME-RESOLVED DATA	32
4.2.1 Transient transmission spectra of samples (Z-365 and BZ-370)	32
4.2.2 Theoretical model.....	34
4.2.3 Fitting routine for optimization of parameters	38
4.2.4 Simulation of transient-transmission spectra.....	40
CHAPTER 5. ULTRAFAST DYNAMICS OF ZNO	45
5.1 EXCITATION OF CARRIERS BY PU-400.....	46
5.2 TIME-RESOLVED RESULTS	47
5.3 PHYSICAL CONTRIBUTIONS TO THE TRANSIENT SPECTRA OF ZNO.....	49
5.3.1 Bleaching due to population of exciton states.....	50
5.3.2 Stimulated emission.....	51
5.3.3 Band gap renormalization (BGR)	54
5.3.4 Refractive index change	56
5.3.5 Carrier cooling and lattice heating.....	57
5.4 INTERPRETATION OF DYNAMICS BASED ON THE TIME-BEHAVIOUR OF CONTRIBUTING PROCESSES	59
5.4.1 Exciton formation by the 400 nm pump-pulse.....	59
5.4.2 Sequence of processes in the dynamics of ZnO.....	61
5.5 INTENSITY DEPENDENCE OF DYNAMICS	64
5.5.1 Exciton-bleaching and stimulated emission:.....	64
5.5.2 Intensity dependence of band-gap renormalization:.....	66
5.5.3 Intensity dependence of refractive index change and rise of lattice temperature	67
5.6 EFFECT OF LAYER THICKNESS ON THE FEMTOSECOND RESPONSE OF ZNO FILMS	69
5.6.1 Exciton bleaching for different ZnO films.....	70
5.6.2 Influence of thickness on band-gap renormalization	70
5.6.3 Increase of stimulated emission with the increasing thickness	71
5.6.4 Thickness dependence of modulations	72
5.7 SUMMARY	73
CHAPTER 6. ULTRAFAST DYNAMICS OF BATIO₃/ZNO HETEROSTRUCTURES.....	75
6.1 FEMTOSECOND DYNAMICS OF BTO	75

6.1.1 Experimental response of BTO	75
6.1.2 Interpretation of transient data	76
6.2 TIME-RESOLVED DYNAMICS OF BTO/ZNO THIN FILM SAMPLES	80
6.2.1 Time resolved results from BZ-370	81
6.2.2 Interpretation of transient data via model analysis	83
6.2.3 Intensity and thickness dependence of contributions to transient spectra	86
6.3 SUMMARY	88
CHAPTER 7 SUMMARY.....	89
REFERENCES	93

Chapter 1 Introduction

ZnO, a II-VI semiconductor has attracted widespread attention because of its unique combination of properties like a high band-gap energy of 3.37 eV, a large exciton binding energy of 60 meV, environment friendliness, radiation hardness and many more which make it an ideal candidate for applications in novel exciton-related optical devices as well as in fabrication of LEDs, solar-cell windows, photo-detectors etc. [1]. Moreover, optically pumped stimulated emission has been widely reported in ZnO at room temperature which makes it useful for lasing applications [2-4]. ZnO being chemically compatible and stable in contact with other oxides is suitable for integration with ferroelectric, magnetic or other semiconducting materials to form multifunctional oxidic heterostructures. Among others integration of ZnO with a remarkable ferroelectric like BaTiO₃, is of great interest for future electronics and opto-electronic applications [5, 6]. Both BaTiO₃ and ZnO exhibit spontaneous polarization along the lattice c-axis; the polarity of which can be electrically reversed in BaTiO₃ but not in ZnO. Therefore, heterostructures of BaTiO₃ and ZnO envision exciting opportunities for ferroelectric state variables as an additional degree of freedom for device applications [7]. A precise knowledge of the carrier dynamics in such structures is crucial for the design, optimization and ultimately the success of the above mentioned applications.

In recent years, considerable research has been directed towards the study of ultrafast processes in ZnO using a wide range of experimental techniques such as time-resolved pump-probe spectroscopy, time-resolved photoluminescence and optical Kerr gate method to mention a few [8, 9, 3, 10], and it has been observed that at room temperature, excitons play a vital role in the emission processes of ZnO. The lifetime of the excitons on the other hand vary with crystal quality, becoming longer as the quality improves. Non-radiative and radiative excitonic recombination lifetimes of 170 ps and 864 ps for high quality bulk ZnO samples has been reported by Teke et al [11]. Epitaxial ZnO layers have been observed to exhibit shorter carrier lifetimes (few tens of picoseconds) [12], since they usually suffer from higher defect densities as compared to their bulk counterparts. The effective lifetime has been reported to be further reduced under conditions of stimulated emission. Investigations on stimulated emission and lasing mechanisms showed discrepancy in different reports and this has been attributed to the difference in the structural properties of the investigated samples [3]. The intensity of excitation has been seen to have a significant impact on the electron-hole interactions in ZnO. So much so that, when high intensity excitation creates a large density of excited carriers, exciton states cease to exist and electron and holes exist in the plasma state. Reported lifetimes for the electron-hole plasma state range from a few picoseconds to few tens of picoseconds [13-15]. Another crucial parameter which has been found to

significantly affect the ultrafast dynamics in ZnO is the wavelength of excitation or the energy of the impinging photon. It has been reported that stimulated emission upon exciton-resonant excitation show a temporal behaviour which is unlike that upon excitation with energies much larger than resonance [16, 17]. The pump photon-energy dependence of the ultrafast exciton dynamic behaviour in ZnO has also been verified by Wang et.al [18]. Most of the above mentioned reports are based on either resonant excitation of ZnO or excitation with photon energies above the forbidden-gap. The dynamics initiated by below band-gap off-resonant excitation in ZnO still remains to be described by relevant studies.

Heterostructures of BaTiO₃ and ZnO has been intensively investigated with respect to its electrical and electro-optic properties [19-21] but not much is known about its optical properties. Among the few, Böntzen et al. and Voora et.al have recently studied the optical properties of BaTiO₃/ZnO heterostructures with the help of spectroscopic ellipsometry [22, 7].

This work which is intended towards the partial fulfilment of the goals defined by the joint project SFB 762 “Functionality of oxidic interfaces”, is aimed at investigating the relaxation dynamics of photo-excited carriers generated by below band-gap off-resonant excitation of ZnO thin films, and that of ZnO and BaTiO₃ in a double-layered BaTiO₃/ZnO heterostructure configuration. It must be mentioned here that the field was opened by a first PhD thesis focussed on investigation of dynamics in ZnO [23], which revealed a number of issues which could not be resolved and remained open for discussion. Moreover, the study indicated that an in-depth study of the structural properties of the samples is essential for a concise interpretation of the dynamics. In this context, several experiments and the consequent analysis had to be re-done (this time with samples intensively characterised for their relevant properties), to finally disentangle the open questions and find a self-consistent and plausible explanation for ZnO alone, before turning to the double-layer system.

This project is in collaboration with the semiconductor physics group of the University of Leipzig, who have provided the samples used in this study. Femtosecond time-resolved pump-probe spectroscopy in the transmission mode was employed to study the charge carrier dynamics of the samples. Transient transmission changes were induced in the samples by 400 nm femtosecond pulses, which in turn endow with a means to unravel their carrier dynamics. The complex transient data was interpreted with the help of a model analysis based on the dielectric function of the respective materials and complementary experiments performed with an ultraviolet pump centred at 266 nm. The entire work is documented in this dissertation. The following paragraphs briefly outline the contents of this thesis:

Chapter 2 provides a theoretical background comprising key physical concepts of semiconductors and light-semiconductor interaction with a special focus on the probable physical processes induced in a semiconductor by high intensity light pulses. This is followed by a small description of the integration of semiconductors with ferroelectric materials. The concepts introduced in this chapter are expected to help the reader in understanding the results of the work presented later in the thesis.

Chapter 3 describes the relevant properties of the samples used in this work beginning with a brief update of the salient features of ZnO and BaTiO₃. A detailed description of the crystalline properties and surface morphology of the samples are

presented in addition to ground state optical properties like linear transmission and optical constants. The chapter also includes a succinct account of the intrinsic defect states on the basis of photoluminescence measurements performed on the samples.

Chapter 4 deals with the technical aspects related to the experimental technique and analysis of the transient data. This section of the thesis documents all the technical aspects of the pump probe measurements such as processing and acquisition of time resolved data, accuracy of the measurements, correction for chirp, fluences used etc. Subsequent to this, a detailed discussion of the theoretical model and the fitting routine used for optimization of parameters is made. The chapter ends with a presentation of the key results which the aforesaid model must be able to describe and an illustration of its implementation.

Chapter 5 is devoted to the time-resolved results and discussion of ultrafast dynamics in ZnO thin films. The opening section of this chapter conceptualizes the mechanism of carrier-excitation by the off-resonant perturbation of ZnO, which is followed by an overview of its femtosecond response. Thereafter an intensive analysis of the photo-physical mechanisms contributing to the transient response is made, based on which a comprehensive picture of the relaxation dynamics in ZnO is proposed. The influence of the input intensity and thickness of the sample layer on the ultrafast dynamics of ZnO is described in the last two sections of this chapter.

Chapter 6 is dedicated to the analysis and interpretation of charge carrier dynamics of BaTiO₃ and BaTiO₃/ZnO thin films. The first section of this chapter deals with the response of single layered BaTiO₃ sample to femtosecond pulsed excitation. The subsequent section documents the results of time resolved measurements performed on the double layered BaTiO₃/ZnO films. A conscientious analysis of the transient data is presented, which reveals the contributions from each layer and effects due to the sharing of interface by the constituting materials of the heterostructure. Thereafter, a comparative study of the dynamics of ZnO in the single-layered ZnO films and in the double-layered heterostructure configuration is made, in order to extract information on the possible influence of BaTiO₃ on the dynamics of ZnO.

Chapter 7 draws the thesis to its conclusions by giving a summary of the findings of this work.

Chapter 2 Generalities

This chapter is aimed at providing an assortment of topics which aids to the interpretation and understanding of the research work presented later in this thesis. The following is mainly a compilation of knowledge of the books [1, 24-29], which will not be cited repeatedly for any individual finding. The first section describes the salient features of a semiconductor material which is followed by a brief account of light-semiconductor interaction. A separate subsection is devoted to describing the response of semiconductors towards high intensity femtosecond laser pulses, which were used for the pump-probe measurements. A small discussion on the coupling of semiconductors with ferroelectric materials is presented at the end of the chapter.

2.1 Introduction to semiconductors

A semiconductor is a material which has a conductivity intermediate between that of a conductor and an insulator. At ambient temperature, it conducts electricity more easily than an insulator, but less readily than a conductor. The electronic energy levels in a crystalline material form continuous bands of energy. These bands are separated by regions in energy for which no wavelike electron orbitals exist. Such a forbidden region is known as the band-gap of the material. In a pure semiconductor, states below the band gap (valence band) are fully occupied, while states above the band gap (conduction band) are empty. Since the valence bands are fully occupied, electrons in these states have no available momentum states to move into and hence do not contribute to conductivity. Only electrons excited into the upper (conduction) band are involved in the conduction process. It is possible to tune the conductivity of a semiconductor by introducing mobile electrons into the conduction band by doping or by photo-injection. When the semiconductor is excited by photons having energy larger than its band-gap, electrons undergo transition from the valence band to the conduction band leaving behind vacancies generally known as holes. The motion of holes also adds to the conductivity of a semiconductor.

The minimal energy-state in the conduction and the maximal energy-state in the valence band are characterized by a certain crystal momentum (k -vector) in the Brillouin zone. A semiconductor is classified as a direct band-gap semiconductor when the valence band maximum and conduction band minimum are at the same k -vector and as an indirect band-gap semiconductor when they exist at different k -vectors. In a direct band-gap semiconductor, transfer of carriers during absorption or emission of photons occur at the same wave vector at Γ point ($k = 0$) in the momentum space. Vertical optical transitions are possible; therefore phonons do not participate in these transitions. However due to the law of conservation of energy and momentum, such transitions are forbidden in indirect semiconductors. Since the

wave vector k of the phonons is much larger than that of the photons, phonon transitions accompany the indirect transitions to satisfy the momentum conservation law. ZnO is a direct band-gap semiconductor having large band-gap energy of ~ 3.37 eV and the BaTiO₃ samples used in this study also exhibit a direct band-gap of ~ 3.68 eV. Henceforth, the discussion hereafter has been primarily focussed on the properties of direct band-gap semiconductor materials.

2.2 Interaction of light with semiconductors

2.2.1 Propagation

The response of a semiconductor to light is of decisive importance for determining its potential utility. The propagation of light in a semiconductor is governed by the medium's complex index of refraction n^* . The complex-refractive index is wavelength dependent and is given by equation (2.1). The real part signifies the change in phase velocity while the imaginary part accounts for the loss due to absorption experienced by the beam on traversing through the medium. The reflectance R and transmittance T can be calculated with the help of Fresnel's formula [30].

$$n^* = n + i\kappa \quad (2.1)$$

$$R = \left(\frac{n_i - n_s}{n_i + n_s} \right)^2 \quad (2.2)$$

$$T = \frac{2n_i n_s}{n_i(n_i + n_s)} \quad (2.3)$$

$$\alpha = \frac{4\pi\kappa}{\lambda} \quad (2.4)$$

Both reflectance and transmittance (given by equation (2.2) and (2.3) for normal incidence) is a function of the real refractive index n . The fraction of light intensity absorbed in unit length of a semiconductor medium is defined by the absorption coefficient α , which is primarily dependent on the extinction coefficient κ and wavelength λ (equation (2.4)). The complex index of refraction and the absorption coefficient are strongly related to the complex dielectric function $\varepsilon(\lambda)$ of the medium. Both n and κ can be numerically calculated from wavelength-dependent real (ε_1) and imaginary (ε_2) parts of the dielectric function using equations (2.6) and (2.7) respectively.

$$\varepsilon(\lambda) = \varepsilon_1(\lambda) + i\varepsilon_2(\lambda) \quad (2.5)$$

$$n(\lambda) = \sqrt{\frac{\sqrt{\varepsilon_1^2(\lambda) + \varepsilon_2^2(\lambda)} + \varepsilon_1(\lambda)}{2}} \quad (2.6)$$

$$\kappa(\lambda) = \sqrt{\frac{\sqrt{\varepsilon_1^2(\lambda) + \varepsilon_2^2(\lambda)} - \varepsilon_1(\lambda)}{2}} \quad (2.7)$$

It is clear from the above discussion that the dielectric function, which is the fundamental property of a material, contains significant information about the optical properties of a semiconductor material. The dielectric function can be determined by spectroscopic ellipsometry which is an excellent technique for the investigation of the dielectric properties of thin films [31]. The key feature of ellipsometry lies in the fact that the polarization of light is changed upon reflection and the intrinsic properties of the material namely the dielectric function and the thickness play a critical role in determining the nature of this change. Hence, it is possible to determine these fundamental properties by an intensive analysis of the polarization state of the reflected light. The electric field vector of the incident light can be decomposed into s and p polarized components (the s component oscillating perpendicular to the plane of incidence, while the p component oscillates parallel to the plane of incidence). The two components experience different attenuation and phase shift in accordance to the Fresnel's equations. The complex ratio ρ between the reflection coefficients of the s and p polarized components (termed as r_s and r_p respectively) is measured by ellipsometry. The complex reflectance ratio can be further parameterized by the amplitude change ψ and the relative phase difference Δ as shown in equation (2.8).

$$\rho = \frac{r_p}{r_s} = \tan \psi \cdot e^{i\Delta} \quad (2.8)$$

However, ellipsometry is an indirect method, i.e. the measured values cannot be converted directly into the optical constants of the studied material and a model analysis has to be performed. The dielectric function and thickness parameters of all individual layers including the correct layer sequence in the thin film sample have to be considered. A number of model dielectric function for semiconductors have been proposed by researches on the basis of detailed theoretical calculations [32, 33]

2.2.2 Absorption and emission

The light-semiconductor interaction and more specifically the absorption of light by a semiconductor largely depends on the photon energy (or wavelength) of the incident light beam. Photons having energy larger than the band-gap of the semiconductor can be absorbed by ground state electrons which will lead to direct transition of charge carriers from the valence band to the conduction band. This process is called linear absorption or single photon absorption (1PA). Under the parabolic band approximation i.e. when bands are described with an energy-independent effective mass, the coefficient of linear absorption for direct band gap semiconductors can be given by the equation (2.9) [28].

$$\alpha \propto \sqrt{E - E_g} \quad (2.9)$$

where α is the absorption coefficient, E is the photon energy and E_g is the band-gap of the semiconductor. However instead of the ideal square root dependence of the band-edge absorption on $(E - E_g)$, an exponential tail has often been observed for experimentally obtained absorption spectra. This tail is known as the Urbach tail and is attributed to transitions between states which exist below the band edges [29]. Disordering of the perfect crystal resulting from intrinsic defects or doping as well as

fluctuation of electronic energy bands due to lattice vibrations can lead to the formation of these states which extend the bands into the band-gap region. The trailing of valence and conduction band-edge is schematically shown in Figure 2.1(a) where the dashed lines show the distribution of states in the ideal case.

An electron excited to the conduction band by photon absorption and a hole in the valence band can further form a bound electron-hole pair due to the mutual Coulomb interaction. Such a quasi-particle is known as exciton. The motion of the centre of mass (of the constituent electron and hole) is separate and the relative motion yields hydrogen like states having energy $E \propto n^{-2}$ ($n \geq 1$). The band-structure is modified due to the presence of excitons. Exciton states have been observed to exist just below the conduction band; the energy being determined by the binding energy of the excitons which is unique to each semiconductor. The oscillator strength of the exciton states i.e. the probability of excitonic absorption decays in proportion to n^{-3} .

When the incident photons have energies smaller than the band-gap and excitonic resonances, a charge carrier cannot bridge the energy gap by absorbing a single photon. In this situation, the generation of photo-excited carriers may take place by multi-photon absorption processes where several photons are absorbed in an elementary event. The minimum number of photons absorbed at once usually depends on the total energy needed to equal or exceed the band gap of the semiconductor. However, the main difficulty in observing multi-photon processes is their extraordinarily low probability of occurrence as compared to single-photon processes. It is a non-linear process and is crucially dependent on the intensity of the excitation beam. The term ‘nonlinear’ means that the strength of light-matter interaction increases with the increasing light intensity. The lowest-order nonlinear process is two-photon absorption (TPA), in which the attenuation is proportional to the square of the laser intensity. The attenuation of the input intensity I along the z direction can be given by equation (2.10), where α is the linear absorption coefficient and the coefficient related to two-photon absorption is β .

$$-\frac{dI}{dz} = \alpha I + \beta I^2 \quad (2.10)$$

TPA is the simultaneous absorption of two photons of identical or different frequencies. The difference in energy between the lower and upper states involved in the transition is equal to the sum of the energies of the two photons. TPA is also possible for incident photon having energies larger than the band-gap but in such a case the absorption is normally dominated by single-photon absorption. However, it may become significant at very high intensities when the linear transitions are strongly bleached.

Photo-excitation of a semiconductor and subsequent absorption of energy leads to the creation of a non-equilibrium state in the system. Hence it naturally tends to return to equilibrium by energy release, after the external excitation is turned off. A semiconductor undergoes several stages of relaxation before returning to equilibrium [34, 24]. The first stage is the dephasing of the coherence between the optically excited carrier and the electromagnetic field that causes it. Coherent effects are observed at this stage and Boltzmann kinetics which describes the overall electron-hole distribution and effects of scattering on them is not valid in this regime. After the excited carriers loose the coherence with the driving field, comes the intra-band

or inter sub-band relaxation stage. This stage corresponds to the relaxation of the electron-hole pairs from the initial stage after excitation to a certain other stage, for example to a quasi-thermal equilibrium with the lattice and/or to the band-minima before they can recombine. This happens through carrier-carrier scattering or the energy dissipation is mediated by phonons. Fast relaxation has been observed to take place by cascade emission of longitudinal optical phonons followed by a slower relaxation via acoustic phonons [35, 16]. A schematic illustrating the relaxation of carriers excited into states higher into the conduction band to the minima of the conduction band, with the help of phonons is presented in Figure 2.1(b).

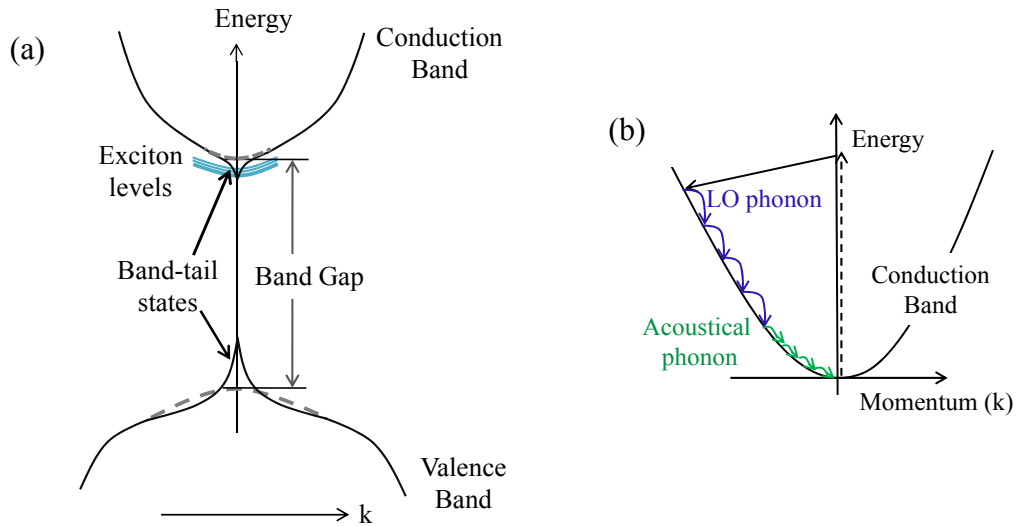


Figure 2.1 (a) Schematic band-picture depicting the tailing of band-edges and exciton levels; (b) Intra-band-relaxation of excited carriers by cascade emission of LO phonons and later by acoustical phonons

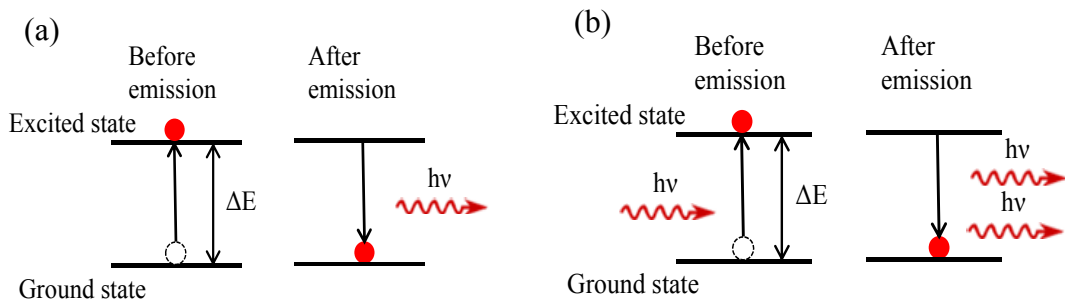


Figure 2.2 Interband relaxation by (a) spontaneous emission, (b) stimulated emission

After the carriers relax to the band-minima, the excited electrons neutralize the corresponding holes and these transitions are designated as recombination. Recombination can take place either radiatively by emission of photons or non-radiatively via phonons or recombination at the trap states like defect and surface states. Emission due to radiative recombination can be further subdivided into two

types: spontaneous emission and stimulated emission. The radiative process in which an excited electron decays in a certain lifetime by photon-emission is known as spontaneous emission. The phase and direction of propagation of the emitted photon is random and is not influenced by the incident radiation. When the incident light induces a radiative transition of an excited electron resulting in the emission of a photon which has the same wavelength, phase and directionality as the incident one, then the emission is known as stimulated emission. The emitted light is highly monochromatic, coherent and directional and amplified since the incident photon generates two output photons. The process of spontaneous and stimulated emission is schematically demonstrated in Figure 2.2 (a) and (b) respectively.

2.2.3 Lifetime of photo-excited states

Emission usually occurs shortly after a system is promoted to the excited state by photo-excitation. If an electron is excited above the ground state E_1 into a state having energy E_2 , it can spontaneously relax back to the ground state by emitting a photon having energy $h\nu$ (h is the Planck's constant and ν is the frequency of emission) given by equation (2.11). If N number of carriers exists in state E_2 , then the rate at which the carriers decay back to the ground state by spontaneous emission is written by equation (2.12), where A_{21} is the Einstein's coefficient [36] for the particular transition.

$$h\nu = E_2 - E_1 \quad (2.11)$$

$$dN = -A_{21}Ndt \quad (2.12)$$

$$dN = -A_iNdt \quad (2.13)$$

$$N(t) = N(0)e^{-At} = N_0e^{t/\tau} \quad (2.14)$$

If the carriers relax through several states having energy less than E_2 , the overall rate can be obtained by equation (2.13) where A_i is the total transition probability, the integration of which yields the time dependent population density (equation (2.14)). The number of excited carriers N thus reduces exponentially with time with the mean lifetime of the excited state given by τ . Hence, it is evident that the mean lifetime of the excited state E_2 is the time scale by which the total number of carriers in the state is reduced to $1/e$ times its initial value.

We have discussed in the previous sub-section that recombination of photo-excited carriers occur by radiative emission as well as non-radiative processes. Moreover, in addition to spontaneous emission, stimulated emission and other decay processes like inelastic scattering and Auger recombination (discussed in the next sub-section) may also contribute to the deactivation of an excited state. All these processes lead to a decay behaviour that in principle cannot be described by a single time constant but involves more complex models of recombination kinetics. In many cases multi-exponential decays (equation (2.15)) or decay behaviour in conformation with the power law (equation (2.16)) has been observed [37, 38].

$$N = \sum_i N_i e^{-t/\tau} \quad (2.15)$$

$$N = \sum_i N_i (t/\tau)^{-\alpha} \quad (2.16)$$

When the lifetime of the processes induced by the excitation is faster than its own time duration, it is not possible to trace them. The characteristic time constants for the relaxation processes can be as short as a few hundred femtoseconds to nanosecond time scales [39, 40]. This necessitates the use of ultra-short laser pulses as the excitation source for investigating the optical excitations of semiconductors in the time domain. They are able to deliver excitation energy to semiconductors as well as probe the material response to the excitation. A brief introduction to the basic physics of ultra-short pulses is provided in the following paragraph.

Ultrashort pulses

In optics, an electromagnetic pulse having time duration of a few tens of picoseconds or in the femtosecond range is commonly referred to as an ultrashort pulse. The distinctive qualities of ultrashort pulses include high peak intensities and broad spectral width [41]. The generation of ultrashort pulses is often achieved using mode-locked lasers, by optical parametric amplifiers (possibly using a supercontinuum as input) or using free electron lasers [42]. The electromagnetic pulses can be described in terms of space and time dependent complex electric field. The real part of the field oscillates with a mean angular frequency of ω_0 corresponding to the central wavelength of the pulse, while the complex field $E(t)$ can be expressed as the convolution of a time dependent intensity amplitude term $I(t)$, a phase term corresponding to mean angular frequency ω_0 and a phase function $\psi(t)$, as given by equation (2.17). The electric field in the frequency domain can be obtained by the Fourier transform of $E(t)$ as in equation (2.18).

$$E(t) = \sqrt{I(t)} e^{i\omega t} e^{i\psi(t)} \quad (2.17)$$

$$E(\omega) = F(E(t)) = \sqrt{S(\omega)} e^{i\varphi(\omega)} \quad (2.18)$$

In the frequency domain, the spectral density of the pulse is given by $S(\omega)$ while $\varphi(\omega)$ represents the spectral phase. The intensity functions $I(t)$ and $S(\omega)$ determine the pulse duration and spectral width respectively. The product of the pulse duration and spectral bandwidth is known as the time band-width product. The lower bound of the time bandwidth product of ultrashort pulses depends on the definition used for defining the its time duration as well as on the shape of the pulses and the lower limit is equal to 0.441 for Gaussian pulses ($\Delta\nu \Delta t \geq 0.441$) [43]. It is clear from the definition of time band-width product that the spectral-width is inversely proportional to the time duration of the pulses, i.e shorter the pulse, broader the spectral width. This is the reason why ultrashort pulses are characterized by a broad spectral width.

The temporal width of the pulse is critically dependent on the spectral phase $\varphi(\omega)$. The pulses are termed as band-width limited pulse when $\varphi(\omega)$ is constant or chirped when $\varphi(\omega)$ is a quadratic function of ω . The chirped pulse exhibits an instantaneous frequency sweep which may be acquired by the pulse due to dispersion as it

propagates through a medium. This results in a temporal broadening of the pulse. The high peak intensity of the ultrashort pulses usually leads to non-linear interactions in the materials through which they propagate. The non-linearly induced physical effects which may arise because of the interaction of semiconductors with high intensity pulses are discussed in the next sub-section.

2.2.4 High-intensity effects

The density of photo-excited charge carriers is crucially dependent on the energy absorbed by the semiconductor system. This is quite clear from the expression for the rate of carrier-generation per unit volume given by equation (2.19), where I is the incident light intensity, α the effective absorption coefficient, and $h\nu$ is the photon energy.

$$N = \frac{I\alpha(1-R)}{h\nu} \quad (2.19)$$

The factor $(1-R)$ accounts for the fraction of incident intensity that is reflected at the interface between the semiconductor and the surrounding medium. Hence, higher the excitation intensity, larger is the density of excited carriers (n_p). Optical nonlinearities are often observed due to the interactions among the large number of particles in the highly dense excited population. A large number of carriers are excited from the valence band to the conduction band by the high flux of incident photons. The probability of further absorption of photons decreases if the states in the conduction band are already occupied in accordance with the Pauli's principle. This effect which occurs for intermediate to high intensity excitations is known as **phase space filling** or **bleaching**. Likewise, the probability of exciton formation or the excitonic strength decreases due to the reduction in the availability of exciton states. Another phenomenon which occurs simultaneously is the decrease in the exciton binding energy due to **screening** of the coulomb attraction between the electron hole pairs as a result of the high n_p [44]. In addition there are other important effects like the **renormalization of the band-gap** which occur because of the many body-interactions among the excited carriers. A schematic diagram showing phase space filling and band-gap renormalization processes is presented in Figure 2.3.

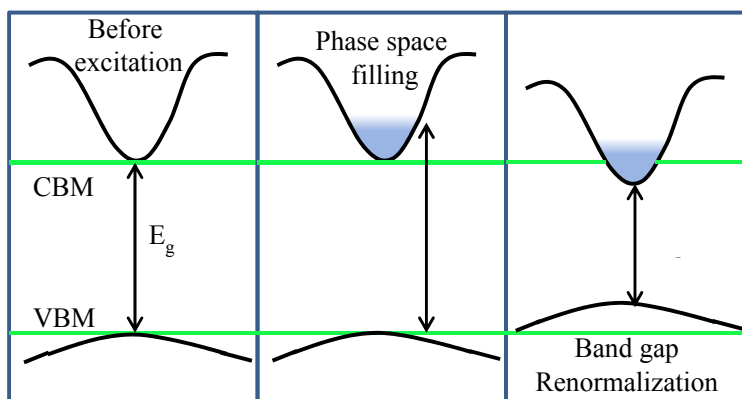


Figure 2.3 Schematic band-picture illustrating phase space filling and band-gap renormalization

The width of the forbidden gap decreases monotonically with the excited carrier density. This owes to the decrease in the self energy of carriers with increasing n_p because of exchange and correlation effects. These effects can be qualitatively explained as follows: According to Pauli's exclusion principle, the distribution of the electrons and holes is not random as two electrons with parallel spins are forbidden to reside in the same level. Consequently the average distance between electrons with parallel spin increases due to the exchange interaction and hence their total repulsive Coulomb energy reduces. The reduction in the repulsive energy leads to the lowering of the total energy of the electron system. The same arguments also hold true for the holes. On the other hand, the probability of finding a hole in the vicinity of an electron is higher than finding another electron due to Coulomb interaction. This correlation effect leads to further lowering of the total energy of the system and reduction of the band-gap energy. It should be noted that the exciton resonances do not change with the renormalization of the forbidden gap. This is due to the almost complete compensation of the red-shift (from band-gap renormalization) by the blue-shift (caused by screening of the Coulomb potential) of the exciton resonances [25].

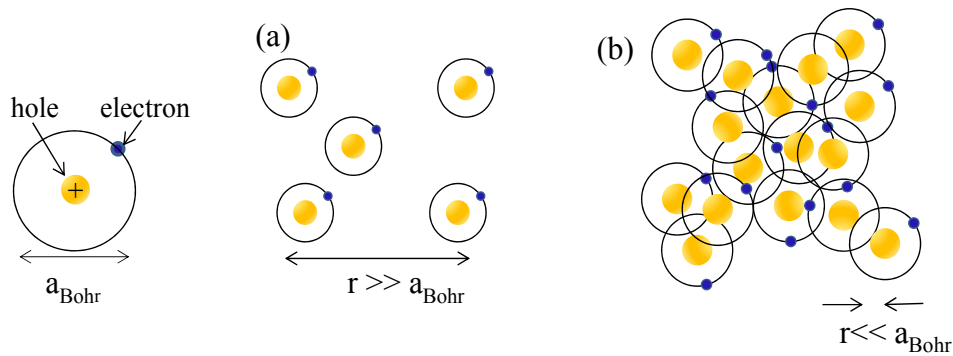


Figure 2.4 Exciton gas (a) below Mott density with the average inter-exciton distance much larger than the exciton Bohr radius; (b) above Mott density with the average inter-exciton distance smaller than the exciton Bohr radius

At very high excitation intensities, the excitons lose their identity as individual quasiparticles and an electron is no longer bounded to a hole. The collective phase so formed is known as **electron hole plasma (EHP)**. The transition of exciton gas to the EHP occurs when the number-density of excitons becomes so large that the average distance between them becomes comparable to or smaller than its Bohr radius. This density is known as the **Mott density** in semiconductors [45]. A schematic depicting the scenario for the excited-density below and above the Mott criteria is shown in Figure 2.4 (a) and (b) respectively. However, it must be mentioned that the transition from the exciton state to EHP state is not discrete but continuous. Many researchers have reported the coexistence of excitons and EHP in the vicinity of the Mott density [3, 46]. This can be conceptualised as excitons existing in a sea of electrons and holes. In this case the free carriers also contribute to the screening of the Coulomb potential of the bound electron-hole pairs.

Another effect which becomes prominent for high intensity photo-excitation of a direct band-gap semiconductor is **stimulated emission** or **optical gain**. With the increasing n_p , the interactions among the excited carriers become more frequent.

Recombination and consequently emission takes place via inelastic scattering of excitons with each other or that with free-carriers and phonons. In case of inelastic exciton-exciton scattering process two excitons (say with $n=1$) interact. One of the excitons is scattered under energy and momentum conservation into a state with $n \geq 2$ or into the ionization continuum, while the other is annihilated by recombination with its respective hole (or at trap states) emitting a photon. A schematic demonstrating the emission via exciton-exciton scattering process is presented in Figure 2.5 (a).

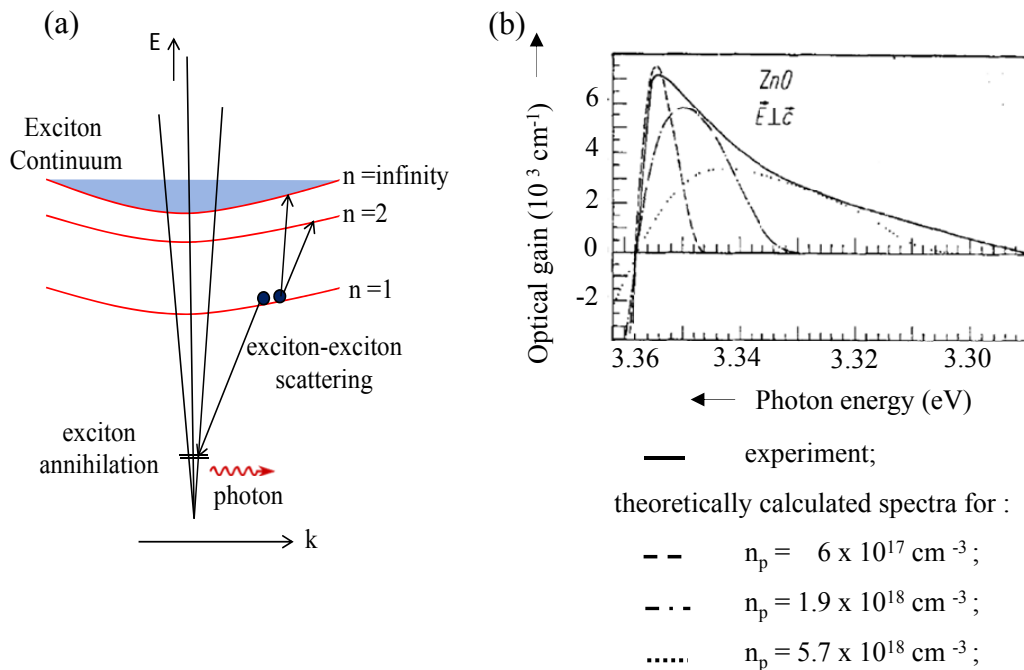


Figure 2.5 (a) Schematic of stimulated emission by exciton-exciton scattering; (b) Optical-gain spectra of ZnO as a function of excited carrier density [47]

Another scattering process which becomes important at higher temperatures is the exciton-free electron scattering where the electron is scattered to a state of higher kinetic energy and the exciton recombines by photon emission. It should be noted that at higher temperatures (usually above 80 K), one or more processes may contribute to the stimulated emission at the same spectral range. For very high carrier densities when electrons and holes exist in the plasma state, direct band-to-band recombination of electrons with holes leads to stimulated emission or optical gain. It has been observed that the gain spectrum at very high-densities is asymmetric with a tailing of the low energy edge. The optical amplification spectra of a ZnO epitaxial layer as a function of the excited carrier density is shown in Figure 2.5 (b) as an illustration [47]. The low energy tail of the gain spectrum is a resultant of scattering among the carriers as well as an energy dependent broadening known as **Landsberg broadening** (or final state damping) [48]. The final state damping occurs due to the rapid relaxation of the empty and occupied states created in the conduction and valence bands respectively on recombination of an electron with a hole in the plasma state.

The other high intensity effects include the formation of excitonic molecules or biexcitons and Auger annihilation. Similar to two hydrogen atoms forming a hydrogen molecule, two excitons can also form a bound complex known as biexciton. When a biexciton is annihilated, it disintegrates into a free exciton and a photon. The resulting emission appears on the low-energy side of the exciton peak. In Auger recombination, an electron recombines with its respective hole and the energy released is utilised to excite another electron higher into the conduction band. The energy is eventually transferred non-radiatively from the third carrier via phonon emission to the lattice. Since this process involves interaction of three particles in an elementary step, it is normally significant only when the carrier density is very high.

2.3 Coupling of semiconductors with ferroelectrics

A dielectric material can be polarized by an applied electric field. In the classical approach to the dielectric model, a material is made up of atoms. Each atom consists of a cloud of negative charge (electrons) bound to and surrounding a positive point charge at its centre. In the presence of an electric field the charge cloud is distorted. This can be reduced to a simple dipole using the superposition principle and polarisation may be defined as the total dipole moment per unit volume. The polarization vector P is directed from negative towards positive charges and the electric field due to the polarization charges has the opposite direction. Some materials may exhibit electric polarization even in the absence of an externally applied field. Such a polarisation is called spontaneous polarisation. The reason for a spontaneous polarization is the static, relative shift of positive and negative charges in the unit cell [27]. Materials are polarised along a unique crystallographic direction and the direction of this axis (or axes) is defined by the materials crystal structure. Ferroelectricity is a property of certain materials which possess a spontaneous polarization that can be switched by the application of an external electric field, yielding a hysteresis loop. A domain is a homogeneous region within the ferroelectric material where all the dipole moments in adjacent cells have the same orientation. The switching of the polarization can be qualitatively explained as follows: In an electric field E a polarised material lowers its energy by $\frac{1}{2}PE$. Any dipole moments which lie parallel to the electric field are lower in energy, while moments that lie perpendicular to the field are higher in energy and moments that lie anti-parallel are even higher in energy. Let us consider a material which is fully polarised so that all dipole moments are aligned in the same direction. When an electric field is applied in the opposite direction, all dipole moments align with the electric field in order to minimise the free energy. Hence the polarisation is switched. However it has been observed that a large switching field is required to switch the field entirely. This is because of defects in the crystal structure as well as the stray field energy initiated by the switching process.

Given the desirable qualities that both ferroelectrics and semiconductors have, it is of high interest to integrate the two types of materials in a way that takes advantage of both. Heterostructures of ferroelectric materials with semiconductors are desirable for multifunctional devices. Charges develop at interfaces where the polarization is discontinuous and the ferroelectric polarization in such heterostructures can be used to modulate the charge distribution in the semiconductor. This is schematically illustrated in Figure 2.6.

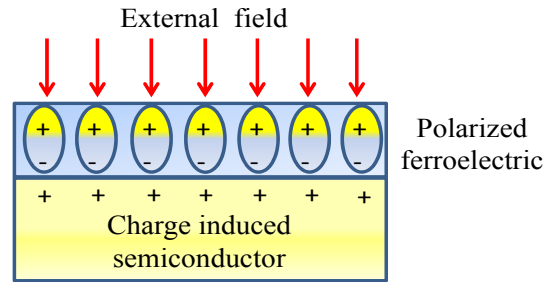


Figure 2.6 Schematic representation of ferroelectric polarization coupling with charges in a semiconductor

Negative charges near the interface attract positive charges in the semiconductor, thus creating a positive sheet charge at the interface, whose density will depend on the magnitude of the polarization charge in the ferroelectric and to a certain extent on the interface quality. In addition to that the properties of charge carriers in the individual layers of the heterostructure can be quite different from those in the bulk material e.g. extremely high mobility, high radiative recombination efficiency etc. [29].

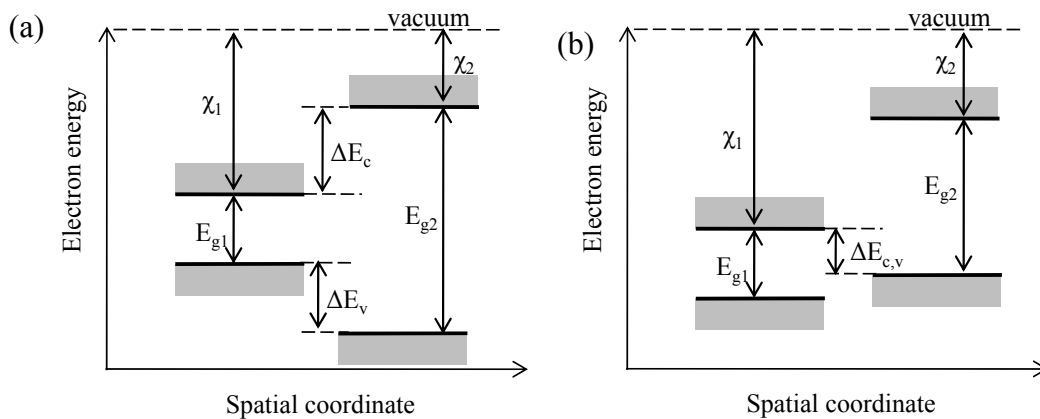


Figure 2.7 Band-alignment in (a) Type-I and (b) Type-II heterostructure [29]

Semiconductors which possess ferroelectric characteristics are known as ferroelectric semiconductors. Like in any semiconductor heterostructure, the relative position of conduction and valence band (band alignment) in a semiconductor-ferroelectric semiconductor heterostructure is determined by the electron affinities of the individual materials [49]. Two types of heterostructures (Type I and Type II) classified on the basis of their band alignment are shown in Figure 2.7. In the type-I structure (straddled band lineup) the lower conduction-band edge and the higher valence-band edge are both in the material with smaller bandgap. Thus, electrons and holes will localize there. In the type-II structure a staggered lineup is present and electrons and holes will localize in different materials.

Chapter 3. Samples Properties

ZnO thin films and BaTiO₃/ZnO thin film heterostructures used in this study were fabricated by pulsed-laser deposition (PLD) technique. In order to gain information about the structure and ground state electronic relaxation, the samples were subjected to a series of characterization measurements. While the crystal structure was investigated using X-ray diffraction, the surface morphology was probed using Optical and Atomic Force Microscopy. The ground state optical properties of the system were extensively studied by performing spectroscopic ellipsometry and linear transmission measurements. Photoluminescence measurements were also performed in order to gain knowledge about the intrinsic defect states which may be present in the samples. It should be mentioned here that fabrication of the samples, X-ray diffraction (XRD), Photoluminescence (PL) and ellipsometric measurements were done in the Semiconductor Group of the University of Leipzig. For better insight to the properties of the specimen under investigation, the general properties of the ZnO and BaTiO₃ are revised first. This revision mainly follows the review on ZnO by Özgür [50] and a few of the standard works on BaTiO₃ [51-56].

3.1. General properties of ZnO

3.1.1 Structural properties

ZnO in its natural form crystallizes in the hexagonal wurtzite phase [57]. The atomic binding of ZnO in its crystal lattice involves sp^3 hybridization of the electron states of zinc and oxygen. This leads to each zinc ion having four oxygen neighbour ions in a tetrahedral configuration and vice-versa as shown in Figure 3.1(a). At ambient conditions, the lattice parameters amount to $a = 0.325$ nm and $c = 0.512$ nm. The crystal is uniaxial and the axis is often referred to as the c -axis in ZnO. ZnO is a direct band-gap semiconductor with the fundamental absorption edge corresponding to the direct transition from the highest valence band to the lowest conduction band at the Γ point ($k = 0$). It has large band-gap energy of ~ 3.37 eV at room temperature. The lowest conduction-band edge is mainly s -like while the states located at the valence-band maximum are p -like. The valence band is split into three double degenerate bands due to spin orbit and crystal-field interactions. The denotations A, B and C are generally used for these valence bands from top to bottom. The band-edge optical absorption is strongly affected by the electron-hole correlations i.e. excitonic effects. Excitons in ZnO have a large binding energy of approximately 60 meV. Corresponding to the three valence bands, excitons A, B and C have been identified with the calculated binding energies varying over a narrow energy range to the point that they are almost identical [58]. A schematic picture depicting the

electronic band-structure in ZnO including the exciton levels is presented in Figure 3.1(b). In addition to the above mentioned energy states, native defects and impurities have been observed to introduce electronic levels within the forbidden-gap. With this regard, a briefing on the intrinsic defects and native n-type conductivity in ZnO is given in the next sub-section.

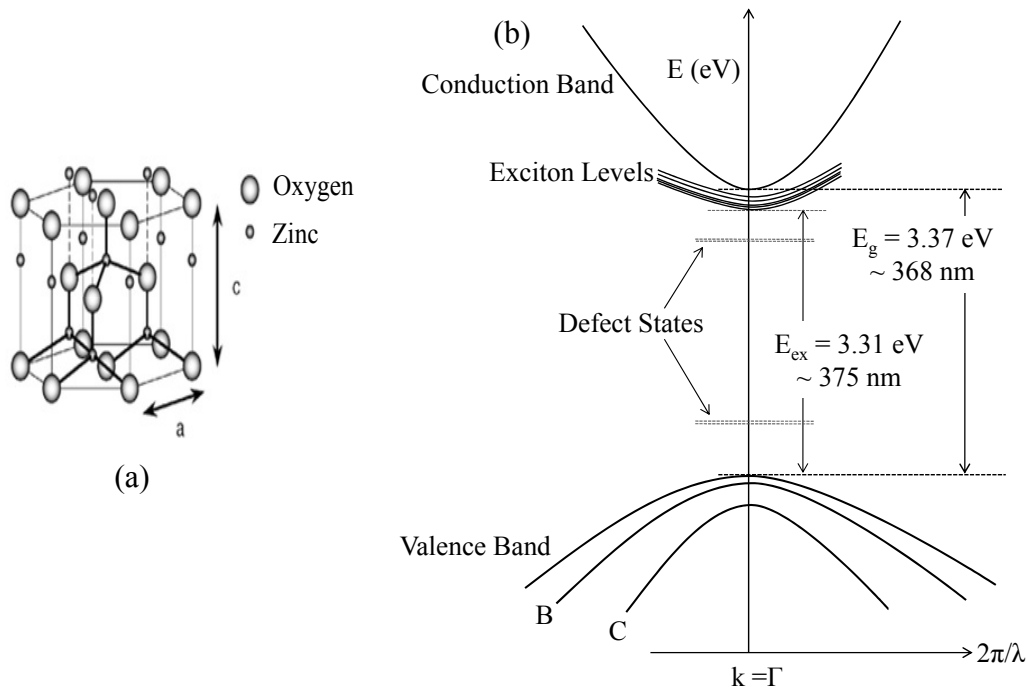


Figure 3.1 Schematic picture depicting the (a) unit cell in hexagonal wurtzite zinc oxide crystal and (b) electronic band structure of ZnO

3.1.2 Intrinsic defects in ZnO

The possible intrinsic defects in ZnO include zinc and oxygen vacancies, interstitials and anti-sites. Oxygen vacancies (V_O) and zinc interstitials (Zn_i) are common in zinc rich conditions while in oxygen rich conditions zinc vacancies (V_{Zn}) are more abundant. The defects that are favoured by zinc rich conditions behave as donors and among them V_O has the lowest energy of formation. Oxygen vacancies can exist as deep donors at ~ 1.3 eV and as shallow donors at ~ 0.3 eV respectively below the conduction band [59]. Zinc interstitials on the other hand has been reported to exist at ~ 2.9 eV above the valence band. Zinc vacancies when present in the ZnO samples act as shallow acceptors and exist at ~ 0.8 eV above the valence band [50].

Apart from the point defects, accidental impurity donors like Ga, Al, Pb, H etc. and acceptors for example N, As or Li may be present in ZnO samples. Substitutional hydrogen impurities perform as donors since it has low formation energy and can be easily ionized. Hence it would be a dominant donor in ZnO materials that were exposed to it during their growth process [60]. These findings have challenged the traditionally accepted knowledge about intrinsic defects as being the cause of n-type character in ZnO. Among others nitrogen was predicted to be the shallowest acceptor in ZnO [61]. Shallow donor-acceptor pair (DAP) transitions or electron-acceptor

transitions have been observed to give rise to a luminescence at ~ 3.23 eV [50, 62] in ZnO. Nitrogen or arsenic were reported to be the shallow acceptors involved in the DAP transitions.

Defect related emission in the visible region has been observed even for high quality ZnO samples. The most common defect related emission is the green emission band seen at around 2.5 eV and is attributed to oxygen vacancies. Other emission bands include orange emission (at ~ 2.12 eV) and yellow emission (at ~ 2.2 eV) occurring as a result of transitions from shallow donor levels to deep acceptor levels [63]. It should be mentioned here that in addition to these native defects, surface defects or line defects which may exist in the ZnO samples may also have an influence on its emission efficiency or recombination dynamics.

3.2. Salient features of BaTiO₃ (BTO) and the BTO/ZnO heterostructure

3.2.1 Structural and ferroelectric properties of BTO

BTO is a semiconductor which is renowned for its ferroelectric, optical and photorefractive properties. It is one of the most important ferroelectric oxides used in electronic applications. BTO is a perovskite with the oxygen atoms lying in the face centres, barium atoms at the vertices and a titanium atom at the centre of the cubic structure (which is found to exist above the Curie temperature (120°C for BTO)). Cooling through 120°C causes the cubic phase of barium titanate to transform to a tetragonal phase with the lengthening of the c lattice parameter accompanied by a reduction in $a = b$. A schematic diagram of a tetragonal unit cell of BTO is shown in Figure 3.2. BTO exists in the tetragonal phase at room temperature with lattice constants of $a = b = 0.399$ nm; $c = 0.404$ nm [64]. A dipole moment arises in the tetragonal phase primarily due to the displacement of Ti atoms with respect to the O atoms in the same plane. Upon application of an external electric field all dipole moments align with the electric field to minimize the free energy giving rise to a spontaneous polarization. Being a ferroelectric, it is possible to switch the polarization direction in BaTiO₃ by reversing the direction of the applied field.

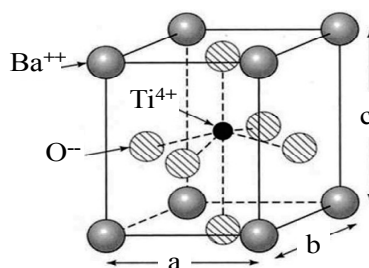


Figure 3.2: Schematic picture depicting an unit cell of BTO in the tetragonal phase

In spite of numerous theoretical investigations made for determining the electronic structure of BaTiO₃, controversies on the nature and energy of its band-gap still exists. Direct as well as indirect nature of the band-gap has been predicted depending on the approaches used for the electronic structure calculations [64, 52]. However, it has been reported that even in case of the band-gap being indirect, the uppermost

valence band is relatively flat and hence, the band-gap can be approximated to be direct [51]. Again the reported values of the direct band-gap energy vary considerably from 2.95 eV - 3.95 eV [65]. The conduction band is associated with titanium (3d) orbitals and the valence band is comprised of the oxygen (2p) orbitals. Intrinsic defects or impurities which might be present in the material create energy states within the band-gap. BaTiO₃ is one of the most widely used photo-refractive materials. A photorefractive material exhibits intensity dependent change of refractive index and absorption. The origin of this effect is thought to be due to the presence of intrinsic defect states in BTO [66]. A succinct account of the defect chemistry of undoped BaTiO₃, based on the defect model proposed by Lewis and Catlow [54], is presented in the following sub-section.

3.2.2 Defects and doping in BTO

It has been experimentally observed that nominally undoped BaTiO₃ exhibit n-type conductivity and p-type conductivity when equilibrated under low and high oxygen partial pressures respectively at room temperature. Moreover, donor doped crystals exhibit appreciable n-type conductivity at all temperatures whereas p-type conductivity (for acceptor doping) is observed only at high temperatures.

The intrinsic defects in BTO consist of vacancy states of which oxygen vacancies play the dominant role. Oxygen and barium vacancies may act as shallow electron and hole traps respectively while titanium vacancies if they exist define deep traps for holes. However, due to large formation energies per defect, purely intrinsic defect reactions are in general unfavourable. Therefore, defect related conduction in BTO is dominated by the presence of accidental impurities like Mg, Mn, Ni, Al, Fe, etc. The energies and the actual site of incorporation of the impurity ions depend on their size. Impurity cations behave as donors when substituted for barium and act as acceptors when substituted for titanium. The intrinsic charge compensation for acceptors and donors are brought about by oxygen vacancies and electrons respectively. Self-compensation is also feasible but only for trivalent cations.

3.2.3 Physical effects observed in BTO/ZnO heterostructures

BTO layers can be successfully grown on ZnO/Sapphire thin films by PLD method [21, 22] to form double-layered heterostructures. In a typical BTO/ZnO heterostructure fabricated by PLD, the ZnO layer adopt the (001) orientation while the BTO layer adopts a (111) orientation direction. Both the material has been observed to possess a high structural quality in the heterostructure configuration. In plane alignment of tetragonal BTO with respect to the hexagonal ZnO is observed in such structures. Both ZnO and BTO are semiconductors which exhibit spontaneous polarization along the lattice c-axis. Application of external electric field can switch the polarization in the perovskite BTO but the polarization is irreversible in ZnO.

The electrical properties of these heterostructures have been studied extensively [67, 19, 6] and reports are mainly focussed on the formation of stable ferroelectric domains in BTO and coupling between the spontaneous polarization of ZnO and the switchable ferroelectric polarization in BTO. Polarization hysteresis measurements on the heterostructures revealed a voltage and frequency dependent asymmetric hysteresis loop. The asymmetry in the hysteresis loop was interpreted to be due to the formation of space-charge accumulation region at the ferroelectric-semiconductor interface on application of an external electric field. Other plausible effects giving

rise to the charge accumulation were found to be the pinning of BTO polarization by ZnO and piezoelectric strain developed in the ZnO and BTO layers in such heterostructures. The coupling effects between BTO and ZnO are also reflected in the optical behaviour of the BTO/ZnO samples [20, 22]. A remnant change in the effective refractive index and thickness observed by ellipsometric measurements was attributed to the lattice charge coupling at the interface. In addition to that a remnant change in the dielectric function of ZnO was also observed due to the influence of ferroelectric polarization of BTO on ZnO.

3.3. Fabrication and characterization of samples

3.3.1 Fabrication of samples via PLD and sample specification

The PLD technique utilizes short and intensive laser pulses to evaporate the target material. In the process, the ablated particles escape from the target and condense on the substrate. The process is carried out in a vacuum chamber to minimize the scattering of the particles. In some cases, however, reactive gases are used to vary the stoichiometry of the deposit [68]. This technique possesses several favourable characteristics for growth of multicomponent materials, such as stoichiometric transfer of the target material to the substrate, compatibility with a background gas, and atomic level control of the deposition rate. While the basic-setup is simple relative to many other thin film deposition techniques, the physical phenomena of laser-target interaction and film growth are quite complex. The process of PLD can be basically divided into four stages: laser ablation of the target material and creation of plasma, dynamics of the plasma, and deposition of ablation material on the substrate followed by nucleation and growth of the film on the substrate surface. Each of these steps is crucial for the crystallinity, uniformity and stoichiometry of the resulting films. Crystal structure of the substrate and lattice matching of the substrate with the material also determines the quality of the deposited film [69]. The experimental parameters that can be tuned in a PLD process are the laser fluence, substrate to target distance, background oxygen pressure and the substrate temperature. All the samples were fabricated with a KrF excimer laser (pulse energy: 600 mJ; at a repetition rate of 15 Hz) in an oxygen atmosphere with a background pressure of 0.02 mbar and a substrate temperature of 700 °C.

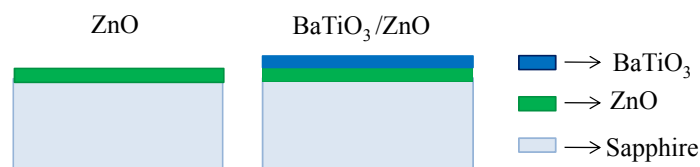


Figure 3.3 Schematic diagram illustrating the stacking of individual layers in ZnO and BTO/ZnO thin film samples

Thin films of ZnO and BTO/ZnO having different layer-thicknesses were grown on a-plane sapphire substrates. A schematic diagram illustrating the stacking of the individual layers for the ZnO and BTO/ZnO samples is shown in Figure 3.3. For the fabrication of the BTO/ZnO films, an identical triplet of ZnO/Sapphire was used as the base. Thus, the ZnO layer in the BTO/ZnO heterostructure and the ZnO films is comparable in all respects. In addition to the ZnO and BTO/ZnO samples, a thin film

of BTO was deposited on sapphire and was used for control experiments. Thicknesses of the thin films were determined by spectroscopic ellipsometry. The measured thickness of the sample layer may vary by a few nanometres from sample to sample; this however, does not have a significant influence on the experimental results. The thickness of the films (or of the respective layers) together with the nomenclature for each sample which will be followed in the rest of this thesis is tabulated in Table 3.1.

Name	Thickness of ZnO layer	Thickness of BTO layer
Z-365	~ 365 nm	x
Z-186	~ 186 nm	x
Z-100	~ 100 nm	x
BZ-370	~ 370 nm	~ 334 nm
BZ-202	~ 202 nm	~ 314 nm
BZ-91	~ 91 nm	~ 330 nm
B-82	x	~ 82 nm

Table 3.1 : Thickness of sample layers and nomenclature for the thin film samples

3.3.2 Characterization techniques

X-ray scattering experiments were performed on samples by the help of a “*Philips X-Pert diffractometer*” in reflection geometry which uses Cu K α radiation ($\lambda = 1.54 \text{ \AA}$). Optical microscopy and atomic force microscopy (AFM) were respectively done on the samples by using the optical mode and AFM mode of “*WITec Scanning near-field optical microscope (AlphaSNOM)*”.

The ellipsometric measurements were performed on a commercial “*VASE ellipsometer from the J. A. Woollam Company*”. In addition to that linear transmission measurements were carried out on a “*Jasco V-670 UV-Visible-NIR spectrophotometer*”. For recording the photoluminescence from the samples, they were excited with the 325 nm line of a CW-HeCd laser. All measurements were performed at room temperature.

3.4. Sample properties

3.4.1 Crystal structure

The θ - 2θ scans (shown in Figure 3.4) performed on the ZnO as well as the BTO/ZnO samples exhibit diffraction peaks which can be indexed to the hexagonal wurtzite phase of ZnO. The high intensity (002) peak at $2\theta = 34.3^\circ$ indicate c-axis orientation of the ZnO layers [70, 1, 50]. The diffraction pattern for the double-layered sample

show fingerprints of the tetragonal phase of BTO in addition to the ZnO peaks. However, the peaks positions related to BTO show a slight deviation from the single crystal values indicating higher c-axis lattice constants for BTO in the heterostructure configuration. This may be due to the incorporation of oxygen vacancies in the BTO layer during the PLD process causing lattice deformation [22].

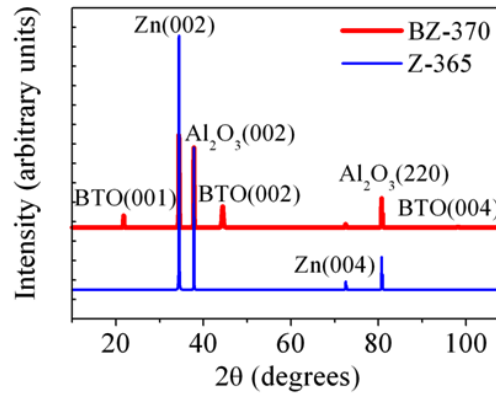


Figure 3.4 X-Ray diffraction pattern of Z-365 and BZ-370

Except for the diffractions coming from sapphire substrate, the XRD spectra are seen to have a relatively low background intensity compared to the signal peaks. This signifies high crystalline quality of the thin film samples. The Scherrer formula (given by equation (3.1)) was employed to determine the crystallite sizes (d_c) corresponding to the (002) reflection of ZnO and BTO.

$$d_c = \frac{0.9 \lambda}{\beta \cos \theta} \quad (3.1)$$

where λ : X-ray wavelength in Å; β : FWHM in radian; and θ : Bragg angle.

The increase in magnitude of the XRD peaks with increasing of film thickness can be attributed due to the presence of more crystalline material in the thicker films. The crystallite size of ZnO tends to increase with the increasing thickness of the ZnO layers in both the systems. Based on the peak position and FWHM of the diffraction peak, crystallite sizes in Z-365, Z-186 and Z-100 were calculated to be ~122 nm, 56 nm and 47 nm respectively (with a relative error of ~ 10 %). The BTO layers in the double-layered samples have a constant thickness value (only slight variation), leading to all the samples having equivalent crystallite sizes ($\sim 29 \text{ nm} \pm 3 \text{ nm}$).

3.4.2 Surface morphology

Similar micro-structural properties were revealed for all the samples by optical microscopy and AFM measurements. The recorded micrographs for Z-365 are presented in Figure 3.5 (a) and (b) as an illustration. A smooth film surface with tiny spot like features (like the ones within the area marked by the black rectangle) could be observed from the microscope images. In order to characterize the surface in more detail, a more sophisticated technique i.e AFM was applied. Dense spike-type

surface morphology with a height profile ranging between 1nm -10 nm is observed for most of the film surface (Figure 3.5 (b)). However, AFM images for areas containing the spots are found to have a broader height profile distribution (~10 nm-150 nm). The light blue pointer seen in the microscope image is the AFM tip, retracted and out of focus so as to get a clear optical image of the sample surface.

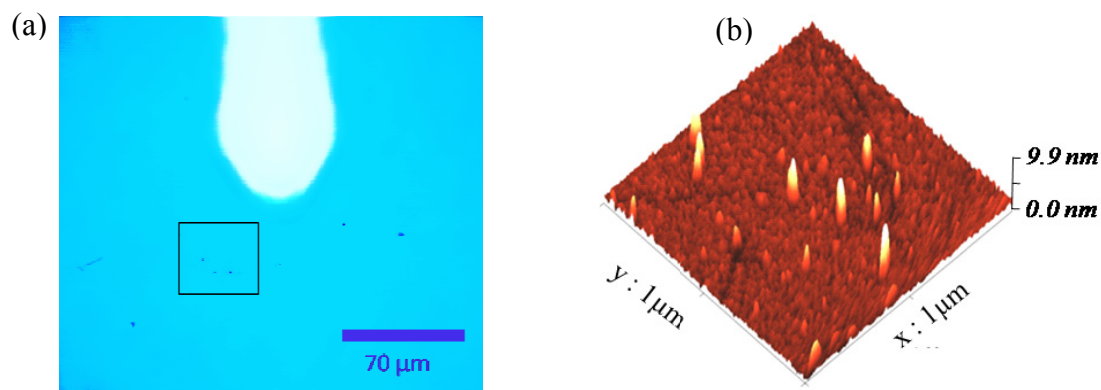


Figure 3.5 : (a) Microscope image and (b) AFM image of Z-365

During the course of measuring the time-resolved spectra from the samples, it was observed that some sample areas show a comparatively higher scattering as compared to that from the other parts of the same sample. It is quite possible that these areas correspond to the areas having broader distribution in height profiles. A broader distribution would correspond to a rough patch which may lead to higher scattering from these particular areas. Such areas of higher scattering were intentionally avoided while recording the pump-probe data. Almost equivalent values of r.m.s roughness (~ 1.5 nm) were calculated for all the samples.

3.4.3 Defect characterization

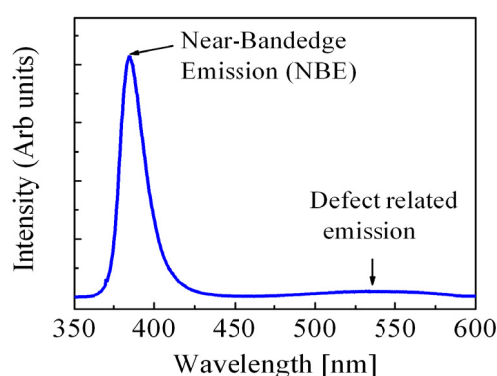


Figure 3.6 : Photoluminescence spectra of Z-365

The PL spectra of the thin film samples were recorded at room temperature in the wavelength range of 350 nm to 600 nm. The luminescence spectrum of Z-365 is shown in Figure 3.6 as a representative. The spectra for the ZnO samples exhibit a strong ultra-violet emission peak at around 380 nm and a relatively weak emission band in the visible region of the spectra. The UV emission peak is generally

attributed to exciton related activity and originates from the recombination of the free excitons in ZnO. The visible emission is associated with the transitions related to the intrinsic defects centers like oxygen or zinc vacancy or interstitials. A weak defect related emission peak is correlated with a low deep-level defect density. The PL spectra of the BTO/ZnO samples exhibit similar luminescence behavior as in the ZnO samples. No additional peaks in the spectra from BTO/ZnO samples could be identified by the PL measurements.

3.4.4 Ground state optical properties

Transmission behavior

The ground state transmission spectra of the ZnO and BTO-ZnO films measured over a wavelength range of 300 nm - 600 nm are plotted in Figure 3.7 (a) and (b) respectively. The *a-plane* sapphire substrate is transparent over the entire spectral region of interest and hence does not affect the transmission behavior of the samples. All the samples exhibit high transmission in the visible region and strong absorption below ~ 375 nm. Urbach tailing of the absorption edge is observed (inset of Figure 3.7 (a)) for ZnO as well as BTO/ZnO thin films. For both set of samples, the amount of absorption in the UV region decreases with decreasing thickness of the ZnO layer. This is because thinner the ZnO layer, lesser the amount of absorbing ZnO it harbors, resulting in a decreased absorption. Fine structures related to excitonic absorption in ZnO [71] is present in the vicinity of the absorption edge. The spectra from BTO/ZnO samples reflect the absorption edge of the ZnO layer and presence of BTO does not seem to have an influence in this region. The transmission spectrum of BTO/sapphire depicts an absorption edge far into the UV corresponding to a band-gap of 3.68 eV.

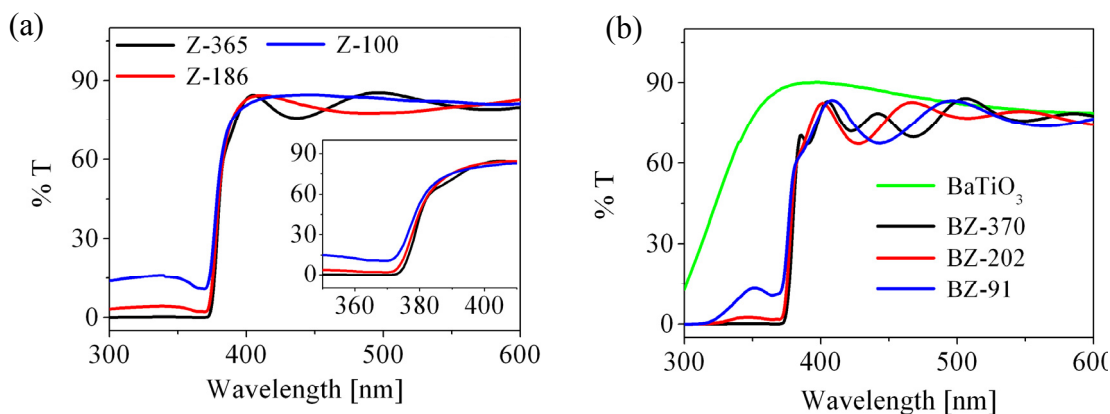


Figure 3.7: Linear transmission spectra of (a) ZnO, (b) BTO and BTO/ZnO samples

Spectral modulations observed in the range of 400 nm to 600 nm are due to fringes arising from interference of light reflected from the top and bottom surface of the thin film samples. The modulations are strongly damped below 375 nm because of the absorption from the ZnO layer in both the sample sets. It is also evident from Figure 3.7 (a) and (b) that the periods of modulations depend on the thickness of the sample layers.

Dielectric function and optical constants from ellipsometry

Ellipsometry measurements were performed on the ZnO and the BTO/ZnO films at room temperature. The ellipsometry data of ZnO was analysed with the help of the model dielectric function for ZnO suggested by Adachi et al. [32] and that for the BTO/ZnO was modelled using the known dielectric function of ZnO and BTO [22]. The time-resolved spectra of the samples were analysed with a model based on the dielectric function of ZnO and BTO. So, for convenience the model dielectric functions and the contributions to it are discussed in detail later while discussing the analysis of the time-resolved spectra from the samples. The optical refractive index and absorption coefficient numerically calculated from the obtained dielectric function as a function of wavelength is plotted in Figure 3.8 (a) and (b) for ZnO and BaTiO₃ respectively. The optical constants obtained from these measurements proved to be crucially helpful in analyzing the data obtained by time-resolved measurements on the samples.

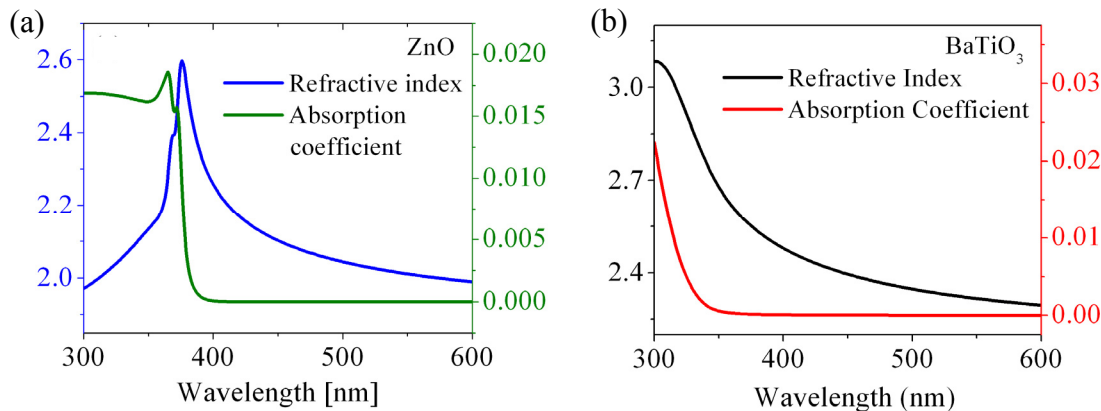


Figure 3.8 Refractive index and absorption coefficient as a function of wavelength for (a) ZnO and (b) BaTiO₃

In the next chapter time-resolved spectroscopy performed on the ZnO and BTO/ZnO thin films and its analysis has elaborately described.

Chapter 4. Femtosecond time-resolved spectroscopy on ZnO and BTO/ZnO thin films

Ultrafast pump-probe spectroscopy in the transmission mode was used to study the relaxation processes of charge carriers in ZnO and BTO/ZnO thin films. In this technique the relaxation of dynamical physical processes excited by a strong light pulse known as pump can be traced with the help of a low intensity light pulse known as probe. The probe pulse reads the relaxation of the excited states by measuring the transient transmission changes incurred in the sample by the pump pulse. A quantitative measure of the temporal evolution of the probe signal as a function of delay time hence provides information on the ultrafast relaxation dynamics of the system. In this study femtosecond pulses ($\lambda = 400$ nm and 266 nm) were used as pump and supercontinuum pulses were used as probe. A previously built pump-probe set-up was used for the time resolved measurements, and for this work the set-up was specially extended to operate also with a pump centred at 266 nm. The first section of this chapter focuses on the experimental details of the time-resolved measurements. This is followed by a detailed discussion of the methodology used for analysis and evaluation of the transient data on the basis of a physical model.

4.1 Experimental Details

4.1.1 Experimental set-up

The femtosecond pulses used for the pump-probe experiments were generated using a commercial system of mode-locked Ti-Sapphire laser with regenerative amplification produced by “*Spectra Physics*”. The system generates 800 nm pulses with a typical duration of 150 fs, and an average output power of 1 mJ per pulse with a repetition rate of 1 kHz [72, 73]. The high energy infrared pulses are then converted to pulses having wavelength 400 nm, by the second-harmonic generation in a KDP crystal.

A schematic diagram of the experimental set-up is shown in Figure 4.1. The 400 nm beam from the second-harmonic generator is split by the beam splitter BS1 in the ratio 20:80. The reflected part (80%) is used as the pump pulse while the transmitted (20%) component is used for generation of supercontinuum light pulses. The pump beam is guided by a system of optics to the lens L1 which focuses it on the sample surface with a diameter of ~ 200 μm . In order to avoid the interference of the pump light while detection of the probe signal, the pump is configured to photo-excite the sample at an angle with respect to the probe. To further this cause, a notch filter is

placed before the signal spectrometer which is specially designed to suppress light at the pump-wavelength. In addition to excitation by 400 nm pulses, measurements were also performed with an excitation wavelength of 266 nm.

Ultrashort pulses centered at 266 nm were obtained by sum frequency generation in a KDP crystal using the 800 nm beam and its frequency doubled counterpart. After efficient removal of the 800 nm part from the resultant beam, the 266 nm and 400 nm wavelength components are separated from each other by a dividing mirror (replacing BS1 in the pump-probe set-up). The 266 nm part is utilized for pumping of sample while the 400 nm component is used for supercontinuum generation. The intensity of the pump pulses can be controlled by using a combination of a $\lambda/2$ plate and a polarizer (P).

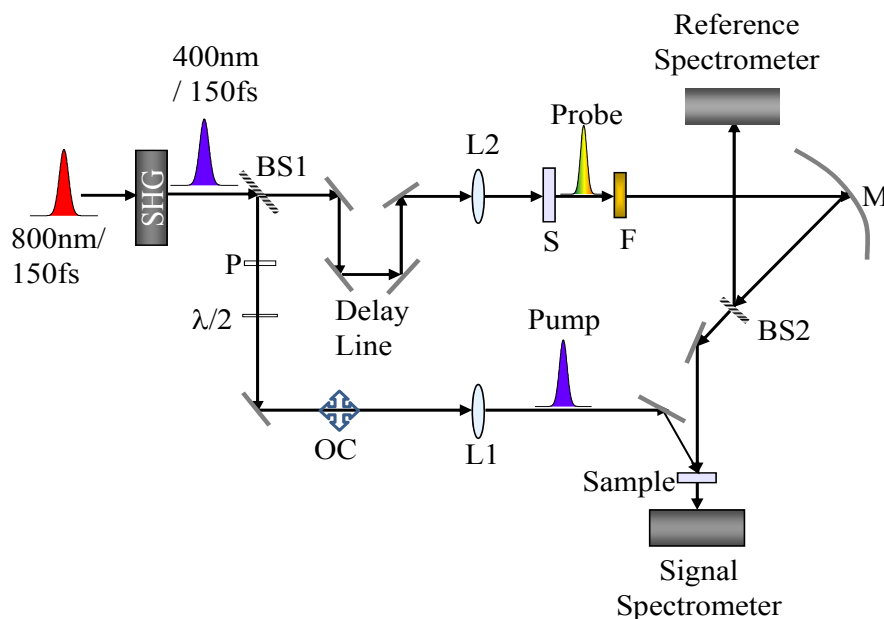


Figure 4.1 Schematic diagram of the pump-probe experimental set-up

The transmitted part of the beam from BS1 (or the 400 nm component in case of the configuration used for measurements with 266 nm) is passed through a variable delay line and focussed onto the sapphire plate (S). The super-continuum pulses having a spectral range of 320-580 nm, generated in the sapphire plate was used as probe. The spectrum of the supercontinuum features a well-pronounced peak at the fundamental wavelength. In order to suppress the contribution from the fundamental wavelength, the continuum is made to pass through a filter (F) filled with a continuously circulating solution of yellow coumarine dye diluted in methanol. Thereafter, the probe beam is focused onto the sample surface by the focusing mirror M. The variable delay line consists of a retro-reflector on a rail system which can be positioned along a precise motorized transitional stage by computer control of a stepper motor. With the help of this arrangement a wide range of delay from -50 ps to 950 ps between the pump and probe can be realised. The probe pulses carrying the information of the transient changes incurred in the sample is detected by a grating spectrometer namely the signal spectrometer. The instability and fluctuations in the white light spectrum necessitates the introduction of another grating spectrometer namely the reference spectrometer [74, 23]. For every measurement, the probe

transmitted from the sample after excitation by the pump-pulse is monitored and normalized with respect to that before excitation. This is made possible by blocking every second pump-pulse by an opto-mechanical chopper (OC) which is synchronized with the repetition rate of the laser system. The grating spectrometers detect the inbound light by disseminating it according to the wavelength of the incoming photon. The signal is then sent to the data acquisition system. The diode lines in the grating spectrometer allow for a spectral resolution of 0.8 nm.

4.1.2 Technical aspects

The spectral profile of the super-continuum probe along with the fundamental beam generating it is shown in Figure 4.2. It is visibly clear that the spectral density is maximum at the fundamental wavelength and decreases rapidly along the wings. A spectrally broad probe is therefore required to maximize the signal to noise ratio at the wings. The quality of super-continuum is critically dependent on the energy of the fundamental pulse and its diameter on the sapphire plate [75]. A spectrally broad and smooth continuum can be produced using high energy pump pulses and when working at distances slightly larger than the focal length. However, this demands a compromise on the spot size of the probe which as a result increases undesirably. The spot size of the probe beam used in these measurements was slightly larger than that of the pump at the sample surface. The pump and probe beam were aligned for spatial as well as temporal overlap thus maximising the signal. The signal to noise ratio can be further increased by averaging over a number of pulses. All time-resolved data presented in this thesis were recorded by averaging over 1000 laser shots.

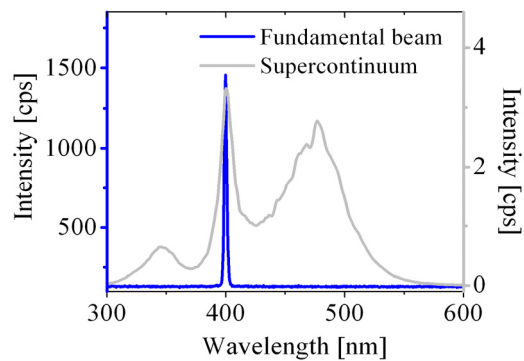


Figure 4.2 Spectra profile for pump at 400nm and super-continuum white light probe

High intensity pump-pulses were required for efficient pumping of the sample at 400 nm while comparatively lower intensities were used for that at 266 nm. This owes to the contrast in the absorption coefficients of ZnO and BTO at 400 nm and 266 nm respectively ($\alpha_{400} = 0.0075 \times 10^4 \text{ cm}^{-1}$; $\alpha_{266} = 16.4 \times 10^4 \text{ cm}^{-1}$). Pump fluences used for the measurements ranged from 15 mJ/cm^2 – 79 mJ/cm^2 for the 400 nm pump; and 2 mJ/cm^2 – 10 mJ/cm^2 for the pump at 266 nm. The fluences used are much lower than the UV damage threshold of the materials which has been reported to be around 115 mJ/cm^2 for ZnO [76, 77] and around 300 mJ/cm^2 for BTO [78]. For the sake of certainty, AFM measurements were performed on the

samples before and after excitation by the pump, and the surface of the samples showed no signs of laser induced deformation after excitation.

4.1.3 Data Acquisition

The transient changes incurred in the sample by the pump-pulse are monitored by comparing the transmission from the sample before and after excitation. This is achieved by calculating the differential transmission or change in optical density which is defined as the negative logarithm of the differential transmission. The transmission before excitation $T_0(\lambda)$ and after excitation $T(\lambda)$ by the pump, normalized with respect to the reference signal is given by equation (4.1) and (4.2).

$$T_0(\lambda) = \frac{I_0^{sig}(\lambda) - I_D^{sig}(\lambda)}{I_0^{ref}(\lambda) - I_D^{ref}(\lambda)} \quad (4.1)$$

$$T(\lambda) = \frac{I^{sig}(\lambda) - I_D^{sig}(\lambda)}{I^{ref}(\lambda) - I_D^{ref}(\lambda)} \quad (4.2)$$

$$\Delta OD(\lambda) = -\log\left(\frac{T(\lambda)}{T_0(\lambda)}\right) \quad (4.3)$$

The intensity components I_D^{ref} and I_D^{sig} are subtracted from the reference and the signal respectively to compensate for contributions that may arise from undesired stray light. These components are recorded by blocking both the pump and probe beams, i.e. just recording any stray light which might be present. A negative logarithm of the differential transmission at each wavelength position (equation (4.3)) generates a change in optical density ΔOD as a function of wavelength spectrum. A positive $\Delta OD(\lambda)$ corresponds to an increase in absorption while negative $\Delta OD(\lambda)$ is a measure of increase in transmission. The entire procedure is repeated for each individual delay time over the set time-range. This results in a three-dimensional recorded data; the three axes being wavelength, delay time and change in optical density as illustrated in Figure 4.3.

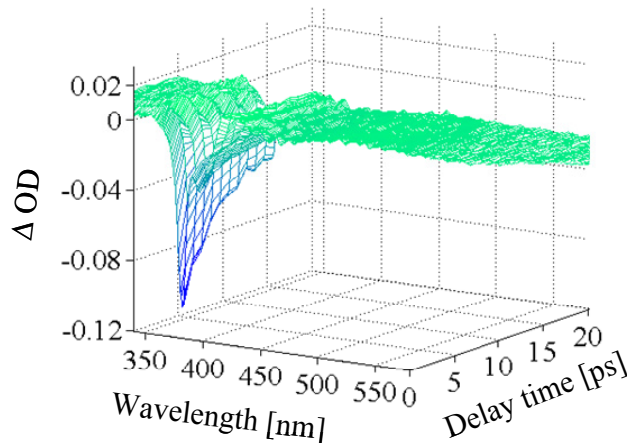


Figure 4.3 Example of three-dimensional experimental spectra measured by using the pump-probe set-up

Different parameters related to the measurements such as the time- range and number of laser shots to be used for the measurements can be manipulated by the use of specially designed software.

Correction for scattered light from pump:

The recorded spectra from all the samples were observed to exhibit a change in transmission at the pump wavelength. This particular feature contributed to the spectra even for negative times i.e. when the pump arrives earlier than the probe at the sample. Since, no signal can be present at negative times, this must be scattering of the strong pump on the sample surface. The transient spectra from the samples were corrected for scattering by subtracting a spectra corresponding to a negative delay time from the spectra at positive times (where real signals can be expected) [23, 74]. All data presented in this work were corrected for scattering.

4.1.4 Time-zero and chirp correction

In pump-probe experiments, time-zero is defined as the time when the peak of the pump-pulse coincides with that of the probe on the sample. By this definition, a negative delay is defined as times when the probe arrives earlier than the pump on the sample and vice versa. Accurate determination of the zero time is indispensable for a reliable interpretation of the observed spectral behavior. Time-zero can be easily determined when the sample is probed using a single wavelength probe; however things get complicated when probing with a supercontinuum pulse. The supercontinuum is chirped due to self-phase modulation and group-velocity dispersion in the material producing it. This leads to different spectral components of the probe reacting with the sample at different times for a specific delay of the pump-probe set-up, which in turn deteriorates the time-resolution from the value which would be expected in limit of the cross-correlation between the pump and probe.

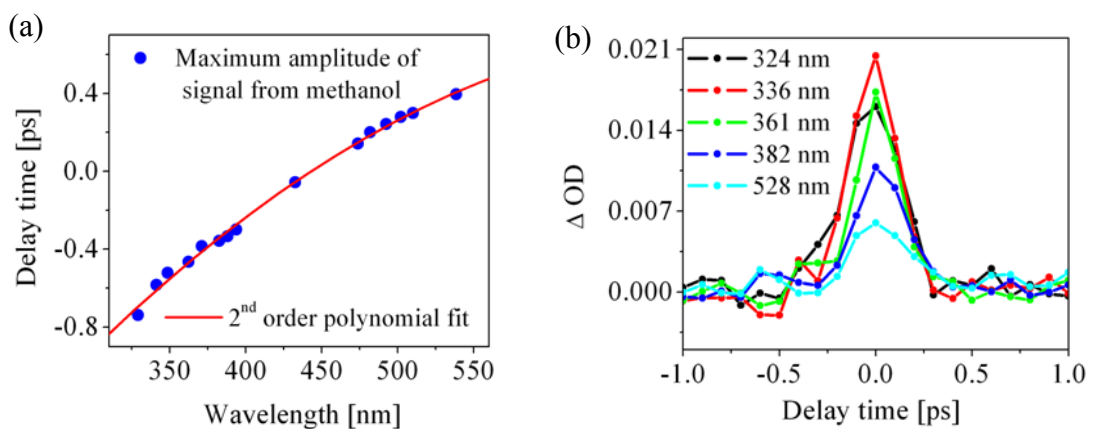


Figure 4.4 (a) Chirp spectrum obtained from methanol (Excitation $\lambda = 400$ nm); (b) Temporal evolution of the methanol signal corresponding to different wavelengths after chirp correction (Excitation $\lambda = 266$ nm)

Methanol exhibits an instantaneous response to the femtosecond pulses at 400 nm as well as at 266 nm [74, 79]. The evolution of the signal's maximum occurring for different wavelength components at different times reproduces the chirp of the white-

light continuum. As an example the spectrum of chirp measured from the signal of methanol initiated by 400 nm pump pulses is shown in Figure 4.4(a). It is evident that the signal is spread over duration of ~ 1.2 ps. All data presented in this thesis was compensated for chirp using the dispersion curve obtained from methanol, in the guidelines of the method proposed by Kovalenko et.al [75]. A temporal resolution of ~ 150 fs and an accuracy of time correction of ~ 50 fs could be achieved after the chirp correction. It should be mentioned here that the experimentally determined dispersion behavior of the supercontinuum and hence the time-resolution does not change upon changing the pump-wavelength from 400 nm to 266 nm. As an illustration the chirp compensated signal of methanol excited by 266 nm pulses is shown in Figure 4.4(b).

4.2 Analysis of time-resolved data

This section focuses on the analysis of the time-resolved data obtained by the experimental technique discussed in the preceding segment. It was observed that a mere visual analysis of the transient spectra is not sufficient for identification and interpretation of the underlying physical mechanisms giving rise to the transient transmission changes in the sample. Moreover for an accurate analysis of the time behaviour of each of these processes, it is essential to deconvolute them from each other first. Thus arises the need for a detailed physical model, by the help of which the time-resolved spectra from the samples can be physically simulated and interpreted. A theoretical model based on the model dielectric function of ZnO (in case of the ZnO samples) and that of ZnO as well as BTO (for the BTO/ZnO samples) was developed for that purpose. In the next subsection, the key results of time-resolved measurements carried out on Z-365 and BZ-370 with an excitation wavelength of 400 nm and a pump fluence of 48 mJ/cm^2 , are presented with the aim of introducing the spectral as well as temporal characteristics of the time-resolved response which the proposed model must be able to describe. This is followed by a detailed discussion of the theoretical model, fitting procedure and illustrations showing the correspondence between the experimental and the calculated differential transmission curves.

4.2.1 Transient transmission spectra of samples (Z-365 and BZ-370)

Time-resolved results from Z-365

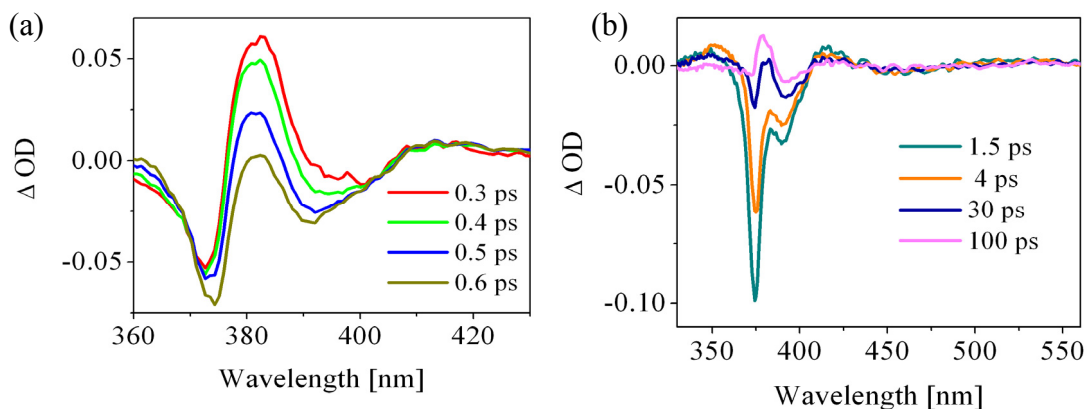


Figure 4.5 (a), (b) ΔOD as a function of wavelength for different delay times

For the purpose of illustrating the **spectral variation** of the time-resolved signals from Z-365, the change in optical density ΔOD as a function of wavelength for different time delays ranging from 0.3 ps to 100 ps is plotted in Figure 4.5 (a) and (b). It is observed that all the spectral features evolve in time. The transient spectra of ZnO reveal an absorption increase at 382 nm simultaneous to a strong bleaching peak at 375 nm. These two features are accompanied by a lower-magnitude but distinct transmission increase at around 391 nm. The absorption increase at 382 nm emerges immediately after excitation and decays rapidly on a time scale of approximately 700 fs. On the other hand, the transmission increases at 375 nm peaks at around 1 ps and diminishes on a time scale of about 100 ps. The contribution at 390 nm reaches its maximum at around 1.1 ps. A slow and gradual decay of amplitude as well as broadening of the peak occurs thereafter before the peak is completely quenched on a time scale of ~ 200 ps.

For very early times up to 0.2 ps, a broad absorption increase (392 nm-600 nm) combined with spectral modulations and a transmission increase at 375 nm is observed. The positive feature decays rapidly on a time scale of 100 fs whereas the bleaching at 375 nm is seen to persist till ~ 100 ps. It is well known that, for time delays within the pulse duration, a simultaneous interaction of the pump and probe takes place with the coherently driven material system. Within this time regime additional signals known as coherent-artifacts superimposed on real signals are known to contribute to transient spectra [80, 81]. While the real signals persist beyond the coherent time regime, the coherent-artifacts are observed to exist only within this time frame. In this light the broad positive feature can be attributed to coherent processes and hence should not be taken into consideration while discussing the relaxation dynamics in the ZnO samples.

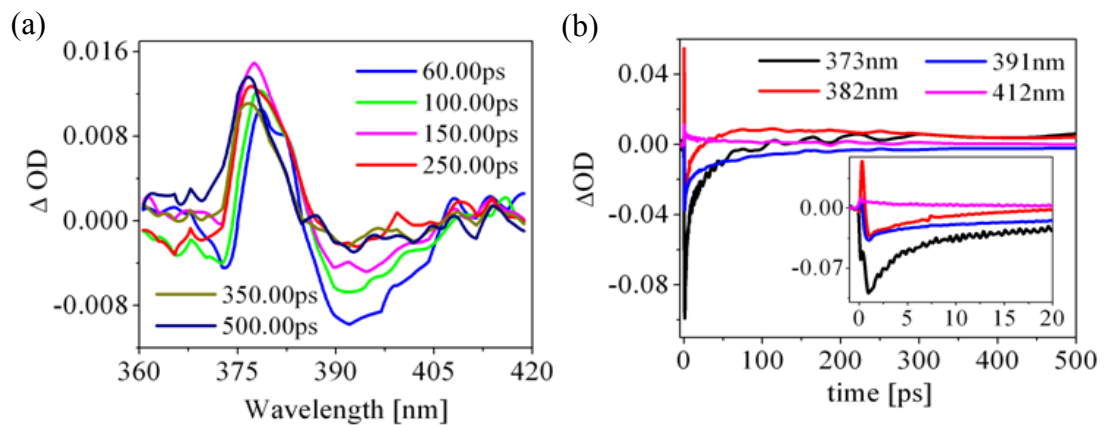


Figure 4.6 (a) Spectral features observed later in the time-resolved spectra;
(b) Temporal variation of different wavelength components

From 60 ps onwards an additional absorption increase centred at 377 nm is visible in the transient transmission spectra of the sample. The magnitude of this feature shows an increasing trend till around 150 ps and shows an almost constant value thereafter. Spectral modulations are observed in the range of 400 nm to 600 nm. The amplitude of the modulations decays with time and reaches a ΔOD value of zero at ~ 150 ps.

For studying the **temporal evolution** of the spectral features, ΔOD is plotted as a function of delay times for selected wavelengths in Figure 4.6 (b). The time

evolution of the various wavelength components exhibit both fast and slow varying components. Very fast dynamics like the rapid decay of the positive contribution at 382 nm are revealed in addition to the gradually decaying contributions like the ones observed at 375 nm and 391 nm. In contrast to the other features, the positive signal at 377 nm is significantly delayed in its appearance and shows a long time behaviour lasting till 500 ps and more.

Time-resolved results from BZ-370

The transient transmission spectra of BZ-370 over a number of delay times ranging from 0.4 ps to 500 ps is plotted in Figure 4.7 (a). It is evident that the strongest contributions to the transient spectra of BZ-370 coincide with that observed in Z-365. However the spectral modulations in the visible region seem to exist in conjunction to a broad positive feature. This feature was not observed for the transient spectra of Z-365 sample. The magnitude as well as period of modulations was also found to be different for the single layered Z-365 sample and the double layer BZ-370 sample.

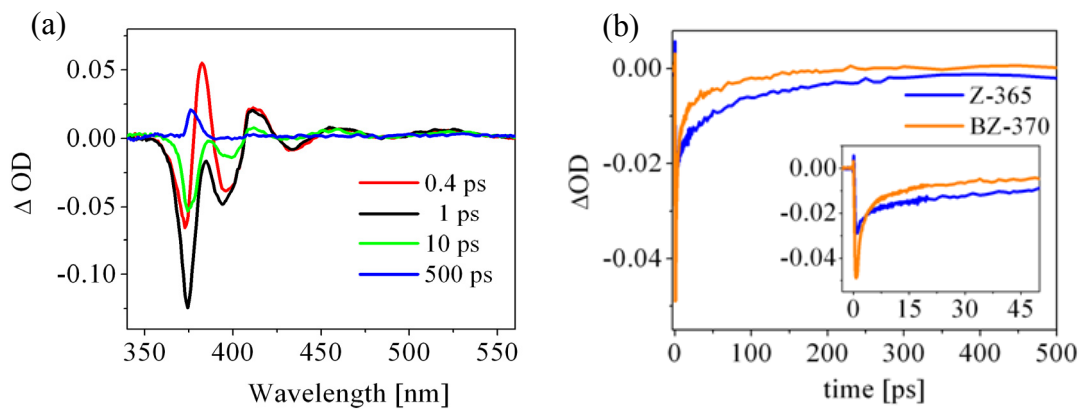


Figure 4.7 (a) Transient spectra of BZ-365 corresponding to delay times from 0.4 ps to 500 ps; (b) Comparison of temporal evolution of the spectral component at 394 nm in the time-resolved spectra of Z-365 and BZ-370

Careful examination of the time evolution of the different spectral contributions in BZ-365 and Z-365, discloses that the time behaviour of the contributing components does not show one-to-one correspondence with each other. As an illustration to this, a comparison of the temporal evolution of the 394 nm wavelength component in the spectra obtained from Z-365 and that from BZ-370 spectra is presented in Figure 4.7 (b). It is visibly clear that the transmission increase at 394 nm in the ZnO sample (depicted by the blue curve in the figure) decays much slowly and gradually in comparison to the one in BZ-370 (depicted by the orange curve).

4.2.2 Theoretical model

The photo-physical processes induced in the sample by the pump-pulse are measured by monitoring changes in its transmission upon excitation. Simulation of the linear transmission spectra is hence a pre-requisite for fitting the differential transmission spectra. Linear transmission spectra from the samples were simulated by using the transfer matrix formulation [30] for ray tracing in thin films.

Any ray can be analytically traced through a thin film system using the laws of reflection and refraction. Figure 4.8 (a) illustrates a schematic of paths traversed by a ray of light incident on a single layer thin film. The ray which enters the ZnO layer suffers multiple reflections from the front and back surfaces of the film. The emerging rays thus interfere with each other giving rise to fringes. The interferometric approach for the calculation of transmission involves adding up the individual contributions from each component. This model works well for a single-layer film, however for systems having more than one layer (as in case of the double-layered BTO-ZnO thin films), the treatment of multilayer film theory based on the continuity relations of the electric and magnetic field components at the interface of two media is more appropriate. Below is described the mathematical aspects of calculation of transmission using this approach.

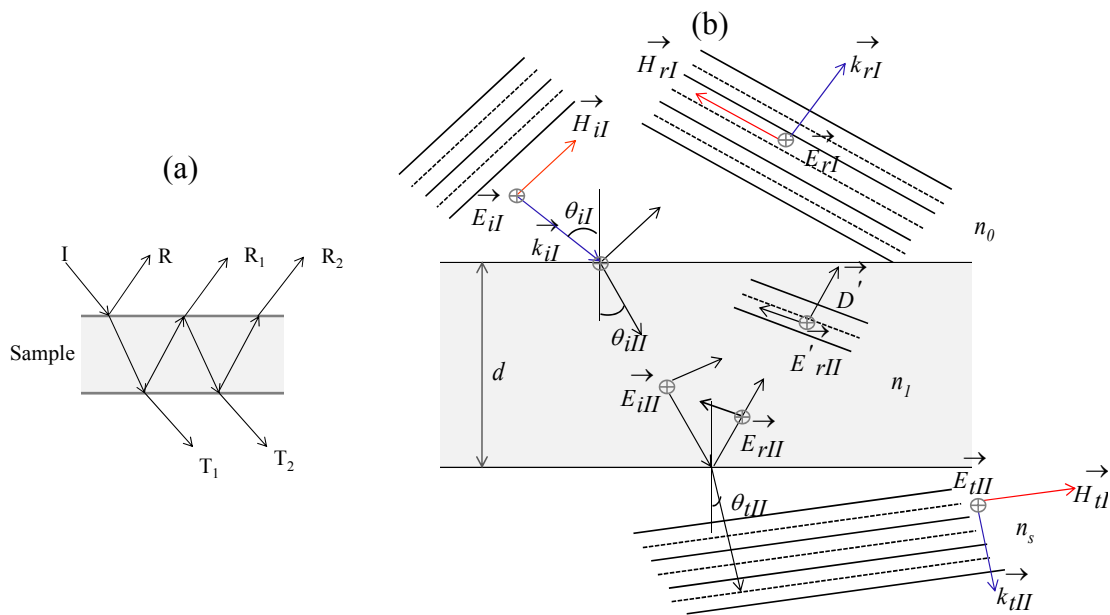


Figure 4.8 (a) Multiple reflection at the interface of two media and (b) field at the boundaries in a thin film system

Mathematical treatment:

Let us consider an electromagnetic wave impinging on a thin dielectric-film sandwiched between two semi-infinite transparent media, one being air and the other being the substrate (as shown Figure 4.8 (b)). Each wave E_{rI} , E'_{rII} , E_{tII} and so forth, represents the resultant of all possible waves travelling in that direction, at that point in the medium. A wave traversing the film once undergoes a shift in-phase $\delta(\lambda)$ given by equation (4.4), where $n_1(\lambda)$ is the refractive index and d is the thickness of the thin film layer.

$$\delta(\lambda) = \frac{2\pi}{\lambda} n_1(\lambda) d \cos \theta_{II} \tag{4.4}$$

For normal incidence θ_{ill} is equal to 1. In addition to that the wave undergoes an absorption loss of $e^{-\alpha(\lambda)d/2}$ corresponding to the optical path covered by a single traversal through the film. $\alpha(\lambda)$ is the absorption coefficient of the sample layer. Taking into account the boundary conditions at the interface of two media, we obtain an expression (given by equation (4.5)) relating the electric and magnetic fields at the interfaces I and II.

$$\begin{bmatrix} E_I \\ H_I \end{bmatrix} = M_I(\lambda) \begin{bmatrix} E_{II} \\ H_{II} \end{bmatrix} = \begin{bmatrix} m_{11} & m_{12} \\ m_{21} & m_{22} \end{bmatrix} \begin{bmatrix} E_{II} \\ H_{II} \end{bmatrix} \quad (4.5)$$

where,

$$M_I(\lambda) = \begin{bmatrix} \frac{1}{2} \left(e^{i\delta(\lambda)+\alpha(\lambda)\frac{d}{2}} + e^{-i\delta(\lambda)-\alpha(\lambda)\frac{d}{2}} \right) & \frac{1}{2Y_1} \left(e^{i\delta(\lambda)+\alpha(\lambda)\frac{d}{2}} + e^{-i\delta(\lambda)-\alpha(\lambda)\frac{d}{2}} \right) \\ \frac{Y_1}{2} \left(e^{i\delta(\lambda)+\alpha(\lambda)\frac{d}{2}} - e^{-i\delta(\lambda)-\alpha(\lambda)\frac{d}{2}} \right) & \frac{1}{2} \left(e^{i\delta(\lambda)+\alpha(\lambda)\frac{d}{2}} + e^{-i\delta(\lambda)-\alpha(\lambda)\frac{d}{2}} \right) \end{bmatrix}$$

$$\text{and } Y_I = \sqrt{\frac{\epsilon_0}{\mu_0}} n_1(\lambda)$$

The matrix M_I relates the two fields at the adjacent boundaries. For a double-layered system there will be three interfaces and two matrices M_I and M_{II} connecting interfaces I-II and II-III respectively. Therefore we have,

$$\begin{bmatrix} E_{II} \\ H_{II} \end{bmatrix} = M_{II}(\lambda) \begin{bmatrix} E_{III} \\ H_{III} \end{bmatrix} \quad (4.6)$$

Multiplying both sides of the equation (4.6) by M_I , we get an effective matrix $M = M_I M_{II}$, relating the electric and magnetic field components at the interfaces I and III. Hence the double-layered system can be treated as a single-layered one having an effective matrix M . The elements of this matrix are a function of the optical constants as well as the thickness of each individual layer in the multilayer structure. Reformulating equation (4.5) in terms of the boundary conditions and expanding the matrices we have,

$$\frac{E_{tII}(\lambda)}{E_{iI}(\lambda)} = \frac{2Y_0}{Y_0 m_{11} + Y_0 Y_s m_{12} + Y_s m_{22} + m_{21}} \quad (4.7)$$

$$\text{where } Y_0 = \sqrt{\frac{\epsilon_0}{\mu_0}} n_0(\lambda) \quad \text{and} \quad Y_s = \sqrt{\frac{\epsilon_0}{\mu_0}} n_s(\lambda)$$

For computation of transmission from the ZnO films, the matrix-elements of the ZnO layer is considered. For BTO/ZnO samples the effective matrix is given by the product of the characteristic matrices of the ZnO and the BTO layer respectively. The matrix corresponding to the sapphire layer was not included in the calculation of the effective-matrix for the following reasons: The thickness of sapphire layer is quite large (\sim hundreds of μm) as compared to the wavelength of the light which will result in interference modulations, the period of which are too small to be resolved by the grating spectrometer used. Hence, a rigorous treatment is not necessary to analyze the propagation of the beam through the sapphire layer and it is sufficient to include the change in the electric field amplitude of the beam upon traversing through the sapphire-air interface. Moreover, due to negligible absorption coefficient of sapphire for the measured spectral range, only the phase change arising from the optical distance traversed by the beam through the sample layer before reaching the sapphire-air interface was considered in this calculation. Therefore we have,

$$E_f(\lambda) = \frac{E_{tII}(\lambda)}{E_{iI}(\lambda)} \cdot t_{sa} \cdot e^{-i\delta(\lambda)} \quad (4.8)$$

where, t_{sa} is the amplitude transmission coefficient at the sapphire-air interface. From the above expression the transmitted intensity can be calculated as:

$$T(\lambda) = E_f \cdot E_f^* \quad (4.9)$$

The ground state transmission was calculated by plugging in the values of the wavelength dependent absorption coefficient and refractive index obtained from the dielectric function of ZnO and BTO as necessitated by the sample under consideration. That the model developed for linear transmission is appropriate for the systems under study is evident from the excellent fit of the experimental and simulated transmission spectra for the ZnO, BTO as well as the BTO/ZnO thin film samples. As an illustration the experimental and calculated curves for Z-365 and BZ-370 is shown in Figure 4.9 (a) and (b) respectively. A small discrepancy which exists around the absorption edge in the transmission spectra for both ZnO and BTO/ZnO systems might be due to contributions from the defect states which exist in the sample sets (confirmed from PL studies) but are not included in the model dielectric function of ZnO.

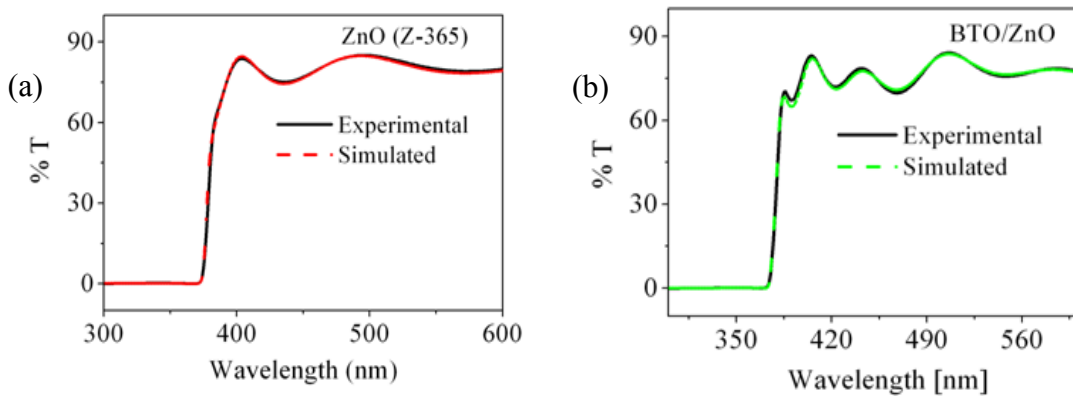


Figure 4.9: Experimental and simulated linear transmission spectra for (a) Z-365 and (b) BZ-370

The ground state transmission spectra correspond to transmission from the samples before excitation by the pump-pulse. The pump pulse is expected to alter the dielectric function of the sample materials which will lead to change of the related optical constants and will be reflected by the changed transmission from the sample after excitation. The change in optical density $\Delta OD(\lambda)$ (equation (4.10)) is defined as the logarithm of the ratio of the transmission before (T_{bp}) and after excitation (T_{ap}) by the pump. A rigorous procedure of variation of parameters (related to contributions in the dielectric function of the concerned materials) was employed to generate the modified transmission and the simulated change in optical density over the entire spectral range. The dielectric function takes into account all the ground state contributions. But, induced processes which may arise upon excitation of a semiconductor material by high-intensity laser pulses (discussed in section 2.2.4) are not included in the formalism as they are induced process. Moreover, contributions arising from intrinsic defect states in ZnO are also not included in the model dielectric function. An empirical way to handle this problem would be to include these contributions, if present, into the model by adding Gaussian or Lorentzian curves at the respective spectral positions of their occurrence. The simulated values for the changes in optical density at each wavelength position are computed according to the expression given in equation (4.11), where w is the width and λ_c the peak position of the added Gaussian curve.

$$sim \Delta OD = \ln \frac{T_{bp}}{T_{ap}} \quad (4.10)$$

$$sim \Delta OD = \Delta OD(\varepsilon(\lambda)) + \frac{A}{w\sqrt{\pi/2}} e^{-2\left(\frac{\lambda-\lambda_c}{w}\right)^2} \quad (4.11)$$

This semi-empirical approach of modelling the transient spectra is capable of taking into account the ground state as well as the induced processes which may arise upon excitation of the ZnO samples with high intensity laser pulses. A meticulous iterative procedure of variation of parameters in the model function is required to obtain a simulated spectrum that matches well with the experimental spectra. This necessitates the use of a fitting routine that determines the best parametric values. A brief description of the fitting procedure is presented in the next sub-section.

4.2.3 Fitting routine for optimization of parameters

The method of non-linear least squares was used to fit the experimental data with the model function using commercially available Matlab software. The transient spectra for a single delay is composed of a set of points represented by an ordered pair $(\lambda_i, \Delta OD(\lambda_i)_{exp})$, where $\Delta OD(\lambda_i)_{exp}$ is the experimental change in optical density corresponding to the spectral position λ_i . The model function on the other hand is a non-linear function $\Delta OD(\lambda_i, \beta)_{sim}$ where β is the set of parametric values to be optimized. The elements of β are varied and optimized by the fitting routine with the goal of obtaining the least possible sum of squared residuals (SSR) defined by equation (4.12) where n is the step size.

$$SSR(\beta) = \sum_{i=1}^n [\Delta OD(\lambda_i)_{exp} - \Delta OD(\lambda_i, \beta)_{sim}]^2 \quad (4.12)$$

The nonlinear fitting procedure is iterative. Starting from the provided set of initial guess values, the method tries to minimize the SSR by successive small variations of parametric values and re-evaluation of the model function until a minimum is reached. The direction and magnitude of the adjustment of parameters depends on the fitting algorithm. The trust-region algorithm [82] was employed to obtain the minimal sum of square residuals. It is capable of solving complex nonlinear problems more efficiently and faster than the other algorithms and represents an improvement over the popular Levenberg-Marquardt algorithm [83]. Moreover it can handle constraints more effectively as compared to the other algorithms, which is necessary for our case given that the spectral positions of the contributions are very close to each other.

An initial value for the chosen set of parameters of the dielectric function which are to be varied is provided while the rest of the parameters are kept fixed. These chosen parameters are then varied simultaneously in the optimization routine to obtain the best possible fit of the experimental data. The optimized values of the ellipsometric parameters are then plugged into the model and thereafter the parameters related to the Gaussians (if added) are varied. Gaussians are added into the model to take into account the signals which cannot be fitted by the parameters of the dielectric function. Hence, it is appropriate to simulate the residual ΔOD with the Gaussians rather than simultaneous variation of all the parameters. This procedure of varying one set of parameters successive to the other ensures that the parameters related to the dielectric function are not under-estimated by the fitting routine (due to the presence of the empirically added Gaussians or Lorentzians). Transient spectra corresponding to each delay in a data-set were fitted with this method. It should be mentioned here that, the same set of chosen parameters are consistently varied for all delays in a data-set. It is observed that maximum change of parameters occurs for early delay times with a subsequent decay back to their original values. Therefore, the optimized values of parameters generated for a transient spectrum at a delay time is fed as the initial estimate for the next successive delay time.

However, every fitting procedure has some limitations due to the nature of the approximation processes used; therefore the following points should be taken note of while assessing the modelled time-resolved results. Firstly, if the fitting routine is unable to converge to a convincing fit of the simulated and experimental curve, it is highly probable that the provided initial values are too far away from the optimal values. In that case a new set of initial values has to be fed into the fitting routine. Secondly and most importantly, the obtained parameters should make sense from the standpoint of the model. For example, a negative value for the width of a Gaussian would be physically meaningless even if the simulated spectra seemingly do fit the experimental spectra very well. Such values should not be considered while description of the ultrafast dynamics from the samples.

As an illustration to the whole procedure, fitting of transient spectra from Z-365 is presented in the next sub-section. For convenience, the contributions to the model dielectric function of ZnO are briefly described at first. This elucidates which of the parameters can be varied and the logic and methodology for choosing the parameters which are to be varied, for obtaining a convincing fit of the experimental spectra. For ease of understanding, the contributions to the dielectric function of BaTiO₃ are discussed later in section 6.1.2.

4.2.4 Simulation of transient-transmission spectra

Contributions to the dielectric function of ZnO:

The dielectric function of ZnO was modelled with the help of the model dielectric function suggested by Adachi. The model takes into account transitions corresponding to the direct-bandgap, and those between the lowest conduction band and the components A, B and C of the valence band in ZnO. In addition to that, excitonic interactions in the neighborhood of the lowest- direct band edge and core-level transitions are also considered. Thermal effects were incorporated into the calculation through a temperature dependent band-gap and exciton broadening [84]. The fundamental contributions to the real and imaginary part of the dielectric function of ZnO together with the overall contribution are plotted in Figure 4.10 (a) and (b) respectively.

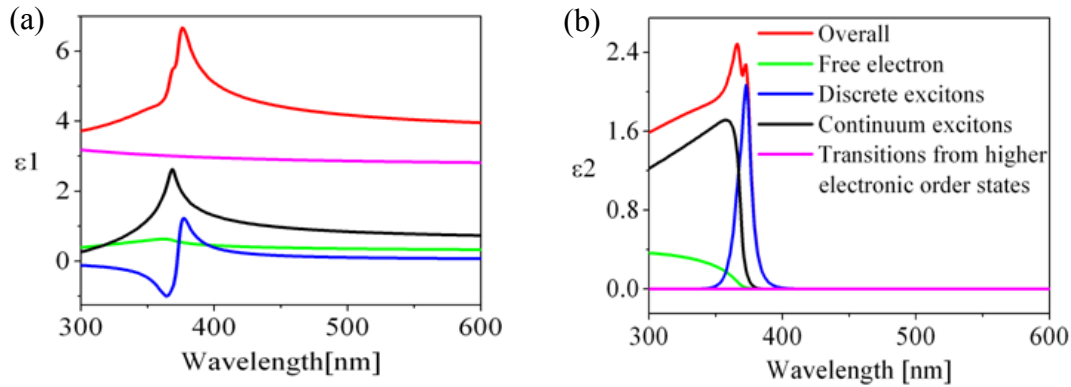


Figure 4.10: Overall and individual contributions to the real (a) and imaginary (b) part of the dielectric function of ZnO

Contribution to dielectric function from discrete exciton states:

The discrete series of exciton states can be expressed as a Lorentzian line shape given by equation (4.13), where $A_{n\alpha}$ is the discrete excitonic strength parameter and $\Gamma_{n\alpha}$ the excitonic broadening. $E_{n\alpha}$ (the discrete-exciton energy) is given by equation (4.14) where G is the 3D exciton Rydberg energy.

$$\varepsilon_{DE}(\lambda) = \sum_{\alpha=A,B,C} \sum_{n=1}^{\infty} \frac{A_{n\alpha}}{E_{n\alpha} - E(\lambda) - i\Gamma_{n\alpha}(\lambda)} \quad (4.13)$$

$$E_{n\alpha} = E_{0\alpha} - \frac{G_{\alpha}}{n^2} \quad (4.14)$$

Three discrete exciton absorptions at ~ 375 nm, 373 nm and 366 nm correspond to transitions from the three valence bands A, B and C respectively to the exciton states. The oscillator strength $A_{n\alpha}$ is proportional to n^{-3} , i.e. the oscillator strength is considerably reduced for higher order excitons as compared to the first or second ordered ones. The exciton states having $n \geq 3$ occur at the same spectral position as

$n = 2$, but with subsequently diminishing amplitudes as shown in Figure 4.11 (a). Thus, a factor 2 was added in the numerator of the third term of equation (4.13) to approximately incorporate the contribution from all higher energy excitonic states. The factor also takes into account the contributions which might arise due to exciton-phonon coupling in the sample. The overall contribution from discrete exciton A is shown in Figure 4.11 (b).

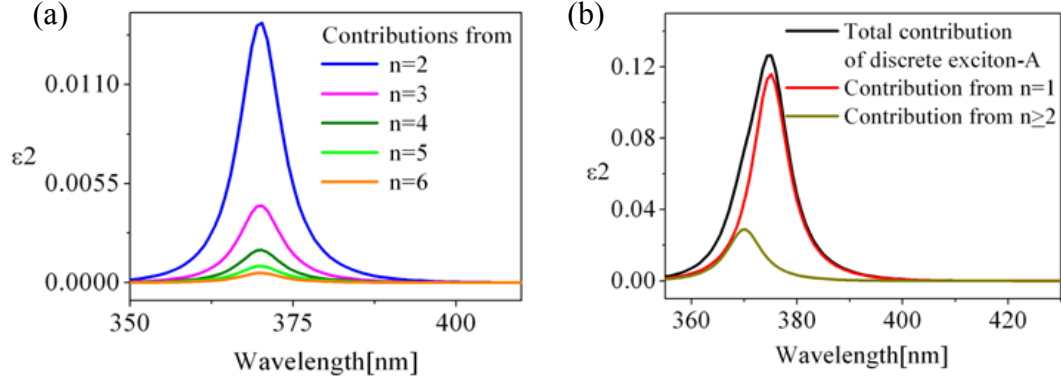


Figure 4.11: (a) Contribution from higher order states and (b) Overall contribution from $n=1$ and higher order states of discrete exciton A

Contribution from Continuum excitons and free electrons:

The contribution of the continuum excitons to the dielectric function ($\epsilon_{CE}(\lambda)$) is given by equation (4.15) where $\Gamma_\alpha(\lambda)$ represents the broadening energy of the band gap $E_{0\alpha}$ and G_α is the exciton Rydberg energy. The line shape of free electron contribution ($\epsilon_{FE}(\lambda)$), given by equation (4.16) shows a square root dependence on the frequency.

$$\epsilon_{CE}(\lambda) = \sum_{\alpha=A,B,C} \frac{A_{c\alpha} B_{0\alpha}}{4G_\alpha \{E(\lambda) + i\Gamma_\alpha(\lambda)\}^2} \ln \frac{(E_{0\alpha})^2}{(E_{0\alpha})^2 - \{E(\lambda) + i\Gamma_\alpha(\lambda)\}^2} \quad (4.15)$$

$$\epsilon_{FE}(\lambda) = \sum_{\alpha=A,B,C} \frac{A_{0\alpha}}{(E_{0\alpha})^{3/2}} \frac{2 - \sqrt{1 + \chi_{0\alpha}(\lambda)} - \sqrt{1 - \chi_{0\alpha}(\lambda)}}{(\chi_{0\alpha}(\lambda))^2} \quad (4.16)$$

$$\chi_{0\alpha}(\lambda) = \frac{E(\lambda) + i\Gamma_\alpha}{E_{0\alpha}} \quad (4.17)$$

Contribution from core-level transitions:

$$\epsilon_{CL}(\lambda) = \epsilon_{1_{off}} + \frac{A_{pol}(E(\lambda))^2}{(E(\lambda))^2 - (E_{pol})^2} \quad (4.18)$$

A constant term $\epsilon_{1_{off}}$ was added in the model dielectric function to take into account higher lying gaps and core excitonic transitions. In addition a wavelength dependent

factor (second term in equation (4.18)) was added to incorporate contributions from transitions in the UV region. These core-level transitions mainly contribute to the real part of the complex refractive index of ZnO.

Fitting of transient spectra

The strongest peak corresponding to negative ΔOD at 375 nm could be simulated by decreasing the amplitude of discrete exciton A (A_{nA}). A decrease in A_{nA} results in minor modulations (on the order of $\sim 10^{-3}$) in the spectral range of 390 nm to 600 nm, in addition to the main bleaching peak at 375 nm. The bleaching peak is asymmetric with higher order excitons ($n \geq 2$) contributing to the extended blue wing as clearly visible in Figure 4.12 (a).

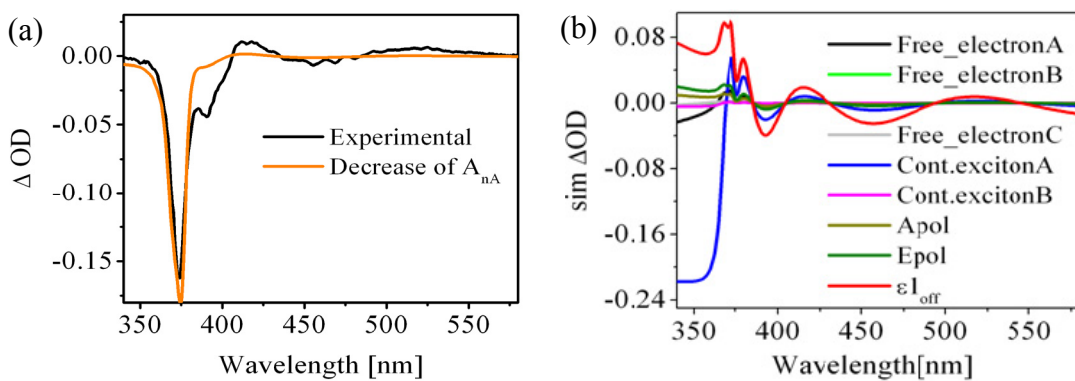


Figure 4.12 (a) Transmission increase at 375 nm due to decrease in amplitude of discrete exciton-A; (b) Contributions from the different parameters which generate modulations between 400 nm and 600 nm

On the other hand, variation of each of the parameters A_{pol} , E_{pol} , continuum excitons-A and B and the free electrons contributions A, B, C yield modulations between 400 nm to 600 nm in the simulated spectra. For a detailed study of the contribution of these parameters, all parameters were varied by 1% and plotted in Figure 4.12(b) for comparison. It is apparent that all parameters do not contribute equally to the change in optical density. The most physically plausible parameter for generating the modulations would be the one which has to be varied the least. The parameter ϵl_{off} contributes most significantly and hence has to be varied lesser as compared to the parameters. This renders it the most suitable parameter for simulating the modulations. However, it also results in a positive component in the UV-region which is not observed for the experimental spectra. To counterbalance this contribution, amplitude of continuum exciton A (which contributes the highest among the negative UV-component generating parameters) was varied in conjunction to ϵl_{off} . This procedure demonstrates the strategy of choosing the strongest parameters that yields the lowest sum of the residuals for the entire spectral range of interest.

Although this fitting procedure simulates most part of transient spectra, none of the parameters in the dielectric function could account for the transmission increase at around 391 nm and the absorption increase at 382 nm. To take these contributions

into account, Gaussian curves centred at ~ 391 nm and ~ 382 nm were added into the model. It should be mentioned here that, because of the close proximity of the different spectral contributions, their spectral positions and widths were allowed to vary over a narrow range of values (based on experimental observation). This allows for the experimental fluctuations, but helps in avoiding the tendency of Gaussian curves to align at the same spectral position and increase (in amplitude) with every iterative step which in turn generates infinitely large and physically meaningless values for the amplitudes and the spectral widths of the contributions. Increasing the temperature in the expression for temperature-dependent band-gap and excitonic broadening, results in absorption increase at around 377 nm. This corresponds to the absorption increase in the transient observed later in the time sequence. However, the amplitude of the experimental peak is comparatively lower than the simulated peak corresponding to the expected rise in temperature (due to heating of the sample). This point is addressed and discussed later in section 5.3.5.

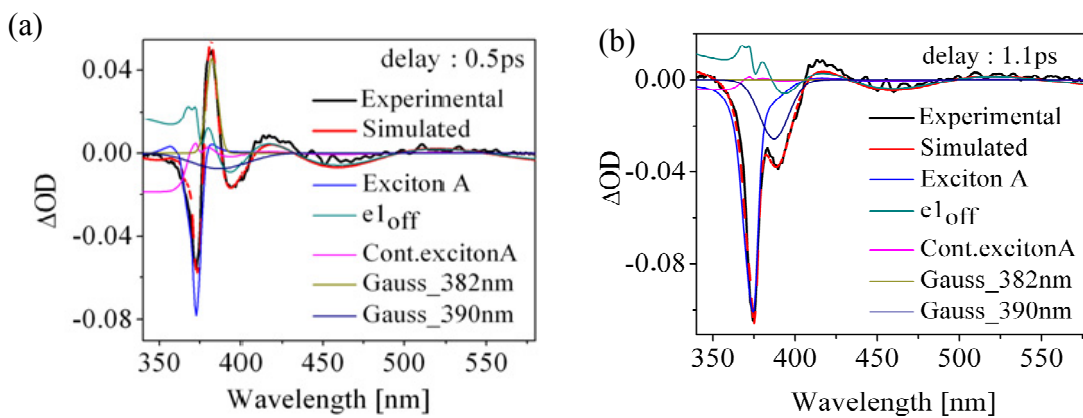


Figure 4.13 Experimental and simulated transient spectra for Z-365 at delay times 0.5 ps (a) and 1.1 ps (b)

From the dynamical point of view, what is most important is the time behaviour of the different contributions. And only those contributing features which have a reasonable time evolution can be included in the self-consistent picture. The differential transmission spectra corresponding to each delay time (in the measured time range) was analysed using the same fitting procedure. As an example, the simulated transient spectra at delays of 0.5 ps and 1.1 ps along with the corresponding contributions are presented in Figure 4.13 (a) and (b) respectively. The goodness of the fits in terms of the sum of squared residuals is of the order of $\sim 10^{-3}$. Based on above considerations and mathematical treatments, a comprehensive analysis of the charge carrier dynamics in ZnO and BTO/ZnO heterostructures will be presented in the succeeding chapters.

Chapter 5. Ultrafast Dynamics of ZnO

In the previous chapters, a detailed procedure for the disentanglement of different contributions in the time-resolved spectra of the samples has been discussed. As a step forward, it would be necessary to ascribe the physical processes which give rise to these contributions. Subsequent to that, a quantitative analysis of their time behaviour must be performed with the objective of obtaining a self-consistent picture of the charge carrier dynamics in ZnO and BTO/ZnO thin films. However, in the course of study it was found that the semi-empirical model described previously could not help in precisely determining the physical origin behind some of the contributions, especially from the empirically included terms. In order to overcome this inadequacy, additional measurements at an excitation wavelength of 266 nm were performed on the samples. These proved to be helpful not only in identifying the unknown contributions to time-resolved spectra of the samples, but also provided the supporting information required for a better understanding of the mechanism of exciton-formation by the below band-gap off-resonant excitation in ZnO. Hereafter, the pump at $\lambda = 400$ nm and that at $\lambda = 266$ nm will be denoted as Pu-400 and Pu-266 for convenience.

The nature of the induced processes as well as their dynamical evolution is expected to be critically influenced by the concentration of excited carriers [85, 10, 46, 86] which in turn varies significantly with the input intensity. Intensity dependent studies were therefore done to further augment the understanding of dynamics. As a further step, time resolved measurements were performed on samples with varying layer thickness. This was done to comprehend the influence of sample's layer thickness as well as microstructure on the proposed dynamical scheme. It is evident from XRD measurements that the crystallite size along the (002) orientation direction changes with the thickness of the sample layer. Consequently, the density of structural defects, grain boundaries etc. may be different in the different samples. Induced processes like stimulated emission and lasing have been reported to be significantly influenced by these properties [87, 88, 46]. Among others, the interference oscillations in the linear transmission spectra have been observed to have one-to one correspondence to the thickness of the samples. Hence, the thickness of the samples is expected to have a strong bearing on its time resolved dynamics.

This chapter focuses on interpretation and analysis of the time-resolved results in ZnO. A detailed discussion of the dynamics of photo-excited charge carriers in BTO/ZnO and the influence of the BTO layer on the dynamics of ZnO are presented later in chapter 6. The opening section of this chapter is devoted to conceptualizing the mechanism of carrier-excitation by the below band-gap off-resonant perturbation of ZnO. The transient changes to the transmission spectra of ZnO incurred upon the

excitation by Pu-400 are described in the subsequent section. For ease of understanding, the time-resolved results of the supporting experiments performed using Pu-266 has also been described in tandem with those obtained by Pu-400. Thereafter, an intensive qualitative as well as quantitative analysis of the different processes is presented, based on which a comprehensive scheme of the dynamics of photo-excited carriers in ZnO thin film samples is proposed. This is followed by an account of the intensity dependence and sample layer thickness dependence of dynamics presented in Section 5.5 and 5.6 respectively.

5.1 Excitation of carriers by Pu-400

The density of charge-carriers excited by the pump-pulse is a function of the absorption coefficient of the material (at the pump wavelength) as well as the pump-fluence. Although the absorption coefficient of ZnO corresponding to $\lambda = 400$ nm amounts to only $0.0075 \times 10^4 \text{ cm}^{-1}$, due to the high intensity pump-pulses used for the experiments it is possible to excite a significant population of carriers to the upper energy states. This in turn gives rise to the time-resolved ΔOD signals. A simple approximation to the number-density of excited carriers can be made using the following relation [85, 89], where the squared factor takes into the account reflective losses at the air-sample interface.

$$n_p = \frac{F_P \cdot \alpha_z(\lambda_P)}{E_P} \left(\frac{2}{1+n_z(\lambda_P)} \right)^2 \quad (5.1)$$

Here n_p is the number density of excited population, F_P the pump fluence, E_P the pump photon energy and α_z , n_z are the absorption coefficient and refractive index respectively of ZnO at the pump wavelength (λ_P). Based on this equation the number-density corresponding to a pump-fluence of 48 mJ/cm^2 (fluence used for time-resolved results presented in section 5.2) was calculated to be $\approx 2.71 \times 10^{18} \text{ cm}^{-3}$. This is a considerable number given that the Mott density of ZnO at room temperature is around $\approx 3.7 \times 10^{19} \text{ cm}^{-3}$ [3]. Moreover, the spectral as well as temporal evolution of contributing components to the transient spectra of Z-365 point to the presence of effects which may arise only when a significantly large density of excited carriers is created by the pump (detailed description of these effects has been given in section 2.2.4). This is in line with the estimated charge carrier density value. This inference is supported by occurrence of the high n_p related contributions at comparable photon energies for the spectra excited by Pu-266, as that excited by Pu-400. Excitation by Pu-266 (photon energy $\sim 4.66 \text{ eV}$), leads to band-to band transition of a large density of carriers even for moderate intensities because of the high absorption coefficient ($16.4 \times 10^4 \text{ cm}^{-1}$) at this wavelength. An approximate excited density of $\approx 4.2 \times 10^{20} \text{ cm}^{-3}$ corresponding to a fluence of 4 mJ/cm^2 (fluence used for time-resolved results presented in the next section) can be estimated using equation (5.1). This amounts to a value one order larger than the Mott density in ZnO. Hence it can be expected that high density effects would be present in the transient transmission spectra excited at this wavelength. The appearance of these contributions at comparable spectral positions (but perhaps more prominent) as that observed for the spectra excited by Pu-400 nm consolidates the view that high

intensity 400 nm pump pulses can efficiently create a large population of excited carriers.

It has also been observed that the femtosecond response of ZnO increases more than linearly with the increasing input-intensity. As an illustration, the maximum amplitude of the transmission increase at the exciton-A resonance (i.e. 375 nm) as a function of pump-fluence is shown in Figure 5.1. For better comparison, an attempt to fit the experimental data points by a linear curve as well as by a second order polynomial equation is demonstrated in the figure.

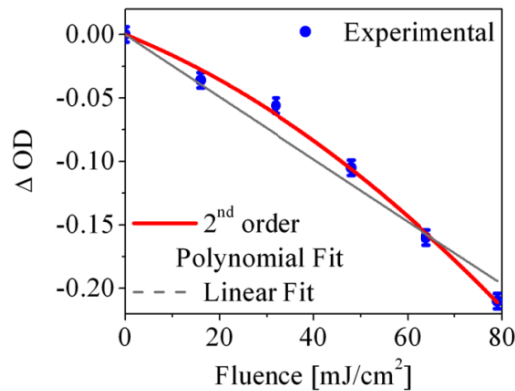


Figure 5.1 Pump-fluence versus maximum of transmission increase at exciton-A resonance

The observation is an indication of multi-photon processes inducing the inter-band transitions; which is indeed expected owing to the sub-band gap excitation of ZnO by Pu-400. In addition to linear absorption, two photon absorption is in all likelihood the non-linear absorption process given the fact that energy of the pump-photons is just less than the band-gap of the material [90-92]. This conjecture is supported by the excellent fit of the non-linear behavior by the second-order polynomial equation. The coefficients to the fit suggest that the linear and quadratic parts contribute equally for fluences ~ 80 mJ/cm². But for input intensities lower than that, the linear contribution dominates. The additional contribution to the excited-carrier population by two-photon absorption could not be estimated because of the unavailability of reliable two-photon absorption coefficient values for ZnO at 400 nm. The next section focuses on the experimental results obtained by the sub-band gap and above band-gap excitation of Z-365 by Pu-400 and Pu-266 respectively.

5.2 Time-resolved results

Time-resolved experiments were performed on Z-365 with Pu-400 and Pu-266 having excitation fluences of 48 mJ/cm² and 4 mJ/cm² respectively. The early time spectral evolution of the signal from the sample excited by Pu-400 and Pu-266 is shown in Figure 5.2 (a) and (b) respectively; while that for delay times ranging from 1.2 ps to 250 ps are plotted respectively in Figure 5.3 (a) and (b).

Excitations of ZnO by both the pumps reveal almost comparable spectral characteristics. These include transmission increases at 375 nm and 391 nm and a positive peak centred at around 382 nm. However, the absorption increase at 382 nm is strongly asymmetric with the red wing extending upto 430 nm on pumping with

Pu-266 (Figure 5.2 (b)) in contrast to the approximately symmetric peak for Pu-400 pumped spectra (Figure 5.2 (a)). An additional bleaching at around 450 nm is also found to contribute to the spectra excited by Pu-266 as clearly visible in Figure 5.3(b). Spectral modulations are observed between 400 nm to 600 nm in both the cases, but for Pu-266-pumped spectrum the modulations appear to be in conjunction with a broad negative feature for early times upto ~ 7 ps. The positive peak at around 377 nm which appears later in the time sequence for the Pu-400 pumped spectra has also been observed for those excited by Pu-266.

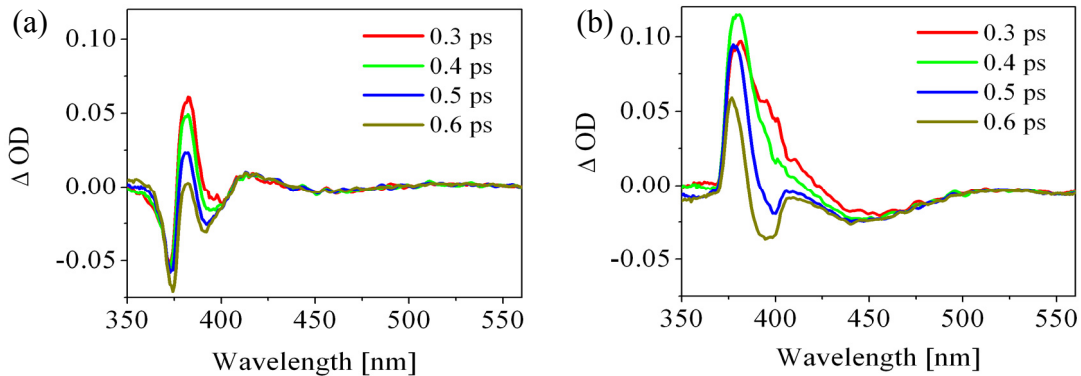


Figure 5.2 Change in optical density as function of wavelength for early delay times upto 0.6 ps for excitation $\lambda =$ (a) 400 nm and (b) 266 nm

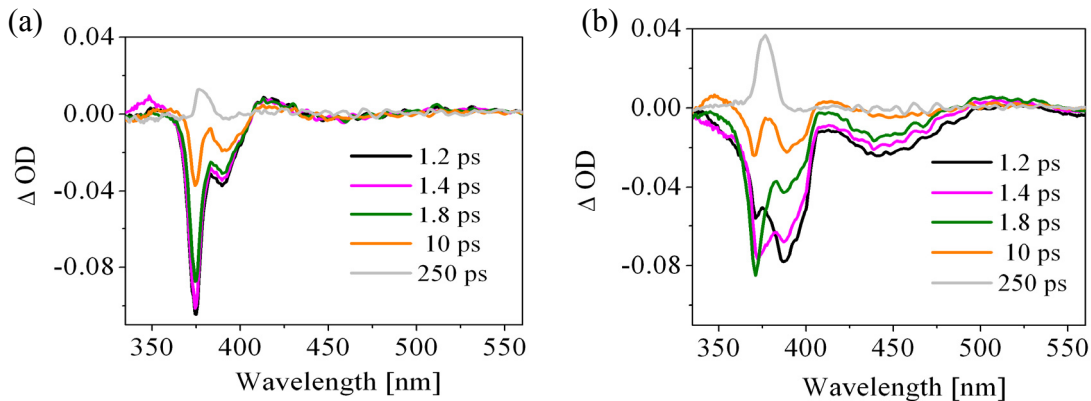


Figure 5.3 Change in optical density as function of wavelength for selected delay times upto 200 ps for excitation $\lambda =$ (a) 400 nm and (b) 266 nm

The changes in optical density as a function of time for selected wavelength components are plotted in Figure 5.4 (a) and (b) for excitation with Pu-266 and Pu-400 respectively. The time evolution of the femtosecond response corresponding to various wavelengths exhibits a rather multifaceted behaviour with a fast contribution at early times followed by a slower decay at longer times. Moreover, the temporal behaviour of the different spectral components, especially the early time-evolution of the components, was observed to be significantly influenced by the wavelength of excitation. Among all, the temporal evolution of the bleaching at 375 nm differs considerably for spectra excited by Pu-400 and that excited by Pu-266. When pumped with Pu-266, the peak-maximum is delayed by around 800 fs (within the limit of an error of ~ 50 fs) in comparison to that which occurs at ~ 1 ps upon

excitation with Pu-400 nm. Furthermore, the contribution decays faster on a time scale of around 30 ps for Pu-266 excitation, in contrast to that observed till around 100 ps for spectra pumped by Pu-400. The maximum of the transmission increase at 390 nm occurs at 1 ps and 1.3 ps for pumping with Pu-400 and Pu-266 respectively. It is evident that the temporal behaviour of the absorption increase at 382 nm shows a similar trend for both the cases.

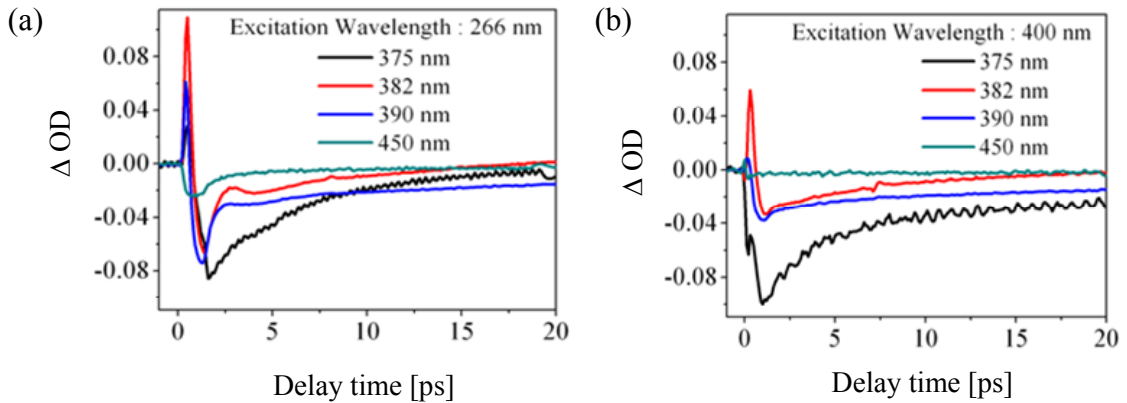


Figure 5.4 Change in optical density as function of delay times for selected wavelengths (excitation $\lambda = 266$ nm (a) and 400 nm (b))

The experimental information on the spectral as well temporal evolution of the contributions to the transient spectra excited by Pu-266 was used to analyse and identify the physical origin behind the contributions to that excited by Pu-400. Detailed discussions of the identified physical are presented in the next section.

5.3 Physical contributions to the transient spectra of ZnO

Each of the experimental spectra over the measured time-range was modelled and analysed according to the procedure discussed and demonstrated in section 4.2. The simulated spectra corresponding to a delay of 0.5 ps (excitation λ : 400 nm) along with all contributing components is shown in Figure 5.5. The resulting sum of squared residuals for each fit amounted to the order of 10^{-3} or below.

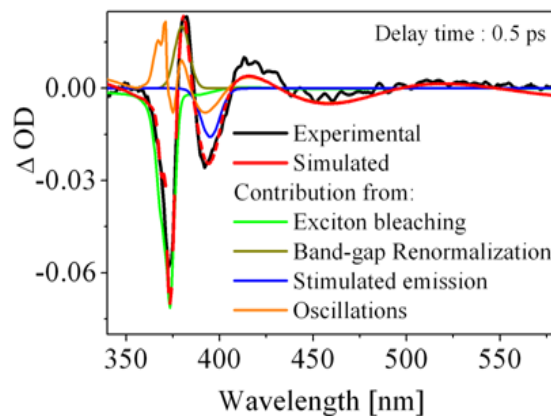


Figure 5.5 Experimental and simulated spectra at 0.5 ps along with the different contributing processes (excitation $\lambda = 400$)

However, a small discrepancy between the experimental and the simulated spectra is found to exist at ~ 420 nm for early delay times. The origin of this mismatch is addressed to in sub-section 5.3.3. The temporal evolution of different contributions (extracted by fitting all the measured time sequences of the optical density changes) was fitted with single or multi exponential decays wherever applicable in order to make a quantitative approximation of the relaxation time scales. It should be mentioned here that all the tabulated decay constants presented further in this thesis are accurate within a relative error of about 8 %.

Also, further in the thesis, the parameters of the dielectric function related to the contributing components are expressed in terms of ‘Normalised Amplitudes’. For ease of understanding, the values of A_{na} , ϵ_{1off} and A_{ca} yielded from the simulations has been normalised such that a value of 1 correspond to their absolute values in the ground state dielectric function. Moreover, the amplitudes of the empirically added contributions are expressed in terms of area under curve, which is nothing but the amplitude of the Gaussian curves incorporated into the model (equation (4.11)). An intensive analysis of each of the contributing components in the time-resolved spectra of Z-365 is presented in the following sub-sections.

5.3.1 Bleaching due to population of exciton states

In semiconductors, intense photo-excitation and subsequent absorption lead to the transition of a large number of charge carriers from states in the valence band to that in the conduction band. If the transitions occur at a rate such that the ground state is depleted before the charge carriers can decay back, further absorption is saturated. Such a phenomenon is known as photo-induced bleaching. The increase in transmission at around 375 nm in the time-resolved spectra of ZnO is attributed to bleaching of exciton states by population of discrete exciton-A states. It is possible to simulate the transmission increase at ~ 375 nm by decreasing the amplitude of discrete exciton-A (A_{na}). The simulated ΔOD for 20 % decrease of A_{na} is plotted in Figure 5.6 (a).

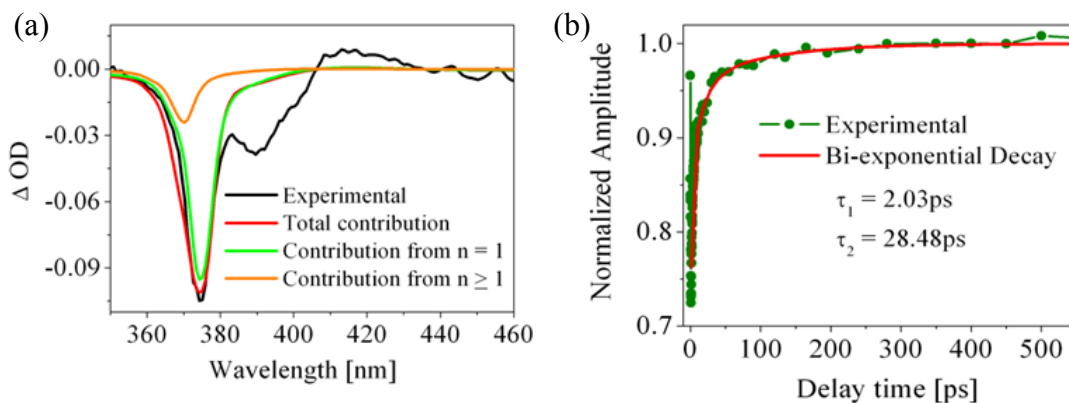


Figure 5.6 (a) Individual contributions from $n=1$ and $n \geq 2$ levels to the overall exciton-A bleaching; (b) Time-evolution of exciton-A bleaching

Since the amplitude of discrete exciton contribution corresponds to the excitonic strength parameter, a decrease in amplitude means reduction in the probability of exciton formation. Excitonic transitions may become less probable either by bleaching or when the states become unstable due to creation of a high-density

exciton population. The instability of the excitonic states ensues when the number density is comparable to or exceeds the Mott density in ZnO. Moreover, when the excited density is in close proximity to the Mott density, existence of excitons in a sea of electron-hole plasma is also plausible [46, 3]. The estimated number density for excitation with 400 nm pump (fluence: 48 mJ/cm²) is well below the Mott transition density in ZnO. Hence, we may safely infer that the bleaching at 375 nm is due to filling of exciton-A levels by the induced exciton population. Contribution from population of first order excitons ($n = 1$) gives rise to the main bleaching peak at 375 nm while that from higher order excitons ($n \geq 2$) cause the asymmetric bulge on the blue-wing of the peak. Decrease in A_{na} results in an increase of amplitude of the simulated peak while the fwhm of the peak remains constant at ~ 9 nm. A maximum change of 33 % in A_{na} corresponding to the maximum amplitude of the transmission increase at 375 nm was observed.

The temporal evolution of exciton bleaching induced by Pu-400 is presented in Figure 5.6 (b). The recovery of A_{na} towards the ground state value reflects the decrease of the induced exciton population or in other words the recombination of excitons. A bi-exponential fit of the temporal evolution reveals decay constants of ~ 2 ps and ~ 28 ps respectively. Such multi-exponential behavior has been previously observed in ZnO systems and can be attributed to the different radiative as well as non-radiative recombination processes. It is well known that intrinsic defect states present within the band-gap is capable of acting as trap states, trapping the electrons before they can radiatively recombine to the respective holes in the valence band. The fast decay constant probably represents the effective non-radiative recombination of charge carriers at room temperature by being trapped at the shallow and deep trap states within the band-gap. The measured time constant of 2 ps attributed to trapping of charge carriers is consistent with the trapping time reported in literature [8, 93]. The larger of the time-constant is attributed to the radiative recombination of the exciton population by processes like inelastic scattering between exciton-exciton as well as that between exciton and free carriers [24, 94]. In both the scattering processes, annihilation of exciton occurs by the emission of a photon thus reducing the amplitude of bleaching. However, it is hard to comment on the time scale of these individual processes. Simultaneous to the above mentioned processes, exciton recombination by emission of one or more longitudinal optical phonons is also probable.

The bleaching at 375 nm induced by the Pu-266 has a lower amplitude as compared that excited by Pu-400. This could be due to the recombination of a majority of excited carriers before the buildup of the exciton-population by processes like electron-hole plasma recombination or the Auger effect, which becomes significant for very high charge carrier densities. The contribution from exciton bleaching is considerably delayed with respect to the stimulated emission contribution at 390 nm in the spectra induced by Pu-266 which supports this argumentation. A more detailed analysis of the temporal-evolution of bleaching corresponding to the above and below band-gap excitation in ZnO is made in section 5.4.1; this leads to important conclusions regarding the mechanism of exciton formation induced by Pu-400.

5.3.2 Stimulated emission

The transmission increase observed at ~ 387 nm in the time-resolved spectra of Z-365 is attributed to stimulated emission. Stimulated emission, being an induced

process, is not expected to be included in the ground-state dielectric function of ZnO. Therefore a Gaussian curve centred at around 387 nm had to be added into the model to account for the contribution. The amplitude as well as width of the Gaussian was allowed to vary but the close proximity (in spectral position) of the emission to other contributing components necessitated the peak position to be constrained over a narrow spectral range (385 nm – 390 nm).

Optically pumped stimulated emission and lasing at room temperature from ZnO epitaxial films has been observed by many researchers [2, 4] and a brief discussion of the different processes which may give rise to such an emission has been presented in section 2.2.4. The spectral position of the contribution corresponds to the P-band luminescence of ZnO [95, 4, 96, 16]. The origin of the P-band is attributed to exciton-exciton scattering processes and is slightly red-shifted with respect to the exciton resonance. Inelastic scattering of first order excitons ($n = 1$) with one another results in one of the excitons being scattered to any of the higher order exciton states ($n \geq 2$) and the subsequent annihilation of the other with the emission of a photon. The energy of the emitted photon (P_n) is given by equation (5.2).

$$P_n = E_{ex} - E_b^{ex} \left(1 - \frac{1}{n^2} \right) - \frac{3}{2} K_B T; \quad (n = 2, 3, 4, \dots, \infty) \quad (5.2)$$

where E_{ex} and E_b^{ex} are the emission and binding energy of the excitons and $K_B T$ is the thermal energy. This explains the red-shift of the emission peak with respect to the exciton resonance at 375 nm in ZnO.

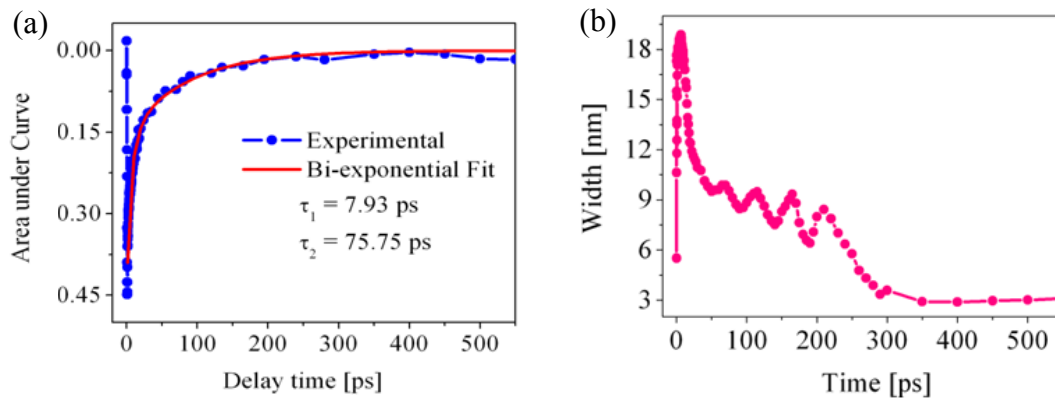


Figure 5.7 Time evolution of (a) area and (b) width of stimulated emission (excitation $\lambda = 400$ nm)

The temporal evolution of area and width of the added Gaussian is shown in Figure 5.7 (a) and (b) respectively. Both area and width of the contributing Gaussian increases on a time scale ~ 1.1 ps with a subsequent decrease thereafter. The area under the curve decays bi-exponentially with time constants of ~ 8 ps and ~ 76 ps respectively indicating the presence of one or more recombination processes (in addition to the exciton-exciton scattering) resulting in stimulated emission at the same spectral position. More than one processes giving rise to stimulated emission at the same spectral position can be expected for moderate to high intensity excitation

in ZnO [12]. The smaller of the decay constants is attributed to the decrease in the exciton population by recombination. The reduction in the exciton population will reduce the number of emitted photons released during the exciton annihilation and hence a decay of the amplitude of stimulated emission. However, the inelastic collisions of excitons are not the only processes which may result in the reduction of the density of exciton population as concluded from the previous sub-section. Consequently we observe different decay time constants for the bleaching and stimulated emission contributions. Reports on time-resolved measurements of the visible emission band in ZnO show that recombination of shallow trapped electrons with deep trapped holes occur on a time scale of several hundred picoseconds [8, 97]. This is comparable to the slower decay of the stimulated emission contribution observed in our case. Thus it is clear that the gradual decay of the amplitude of stimulated emission is due to the recombination of trapped carriers.

The transmission increase centred at 450 nm observed in the transient spectra of ZnO excited by Pu-266 is also attributed to the stimulated emission or gain. This contribution was not observed when the transient transmission changes were induced by Pu-400. Optically active defect levels $\sim 530\text{meV}$ below the conduction band minimum have been reported to exist in ZnO owing to the presence of intrinsic defects like zinc interstitials. Recombination of carriers trapped in these levels could give an emission at $\sim 437\text{ nm}$. However, if this is true then one should also observe an emission upon excitation with Pu-400. With the 266 nm pump we create a high density of excited carriers. Reports on measurements related to the optical gain in ZnO show that the typical gain spectrum at such high excitation densities is not symmetric but has a smooth tail extending towards the longer-wavelength side of the spectrum [47, 98]. The low energy tail is intensity dependent and arises due to an energy dependent broadening known as the Landsberg damping (origin of which damping has been discussed in section 2.2.4). Such a gain spectrum combined with the oscillations observed between 400-600 nm gives rise to negative-amplitude modulations with an enhanced trough centred $\sim 450\text{ nm}$. A schematic diagram demonstrating the occurrence of these modulations as well as the transmission increase at 450 nm is presented in Figure 5.8.

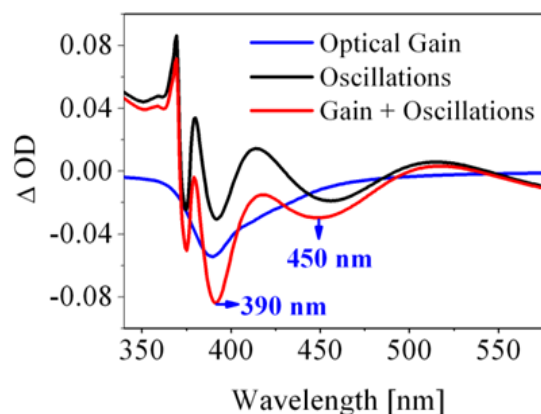


Figure 5.8 Schematic diagram depicting the origin of transmission increase at 450 nm for transient spectra induced by Pu-266

Upon excitation with Pu-400 we create a relatively lower density of carriers and a more symmetric gain profile, which may be the reason that we do not see this feature

for the corresponding time-resolved spectra. A blue shift of transmission increase at 450 nm with time occurs due to the decrease in the energy-dependent broadening.

5.3.3 Band gap renormalization (BGR)

The increase in absorption at ~ 382 nm in the transient transmission spectra of Z-365 can be attributed to renormalization of the band-gap of ZnO as a result of the highly dense population of excited carriers. When an intense femtosecond laser pulse is absorbed by a system, its charge distribution is perturbed instantaneously because of transition of large fraction carriers from the valence band to the conduction band. If the density of excited carriers is large, screening effects resulting from Coulombic and exchange forces induce a narrowing of the band-gap, often termed as band-gap renormalization [9, 29]. This in turn causes a red-shift of the absorption edge and consequently an absorption increase in the vicinity of the band-edge.

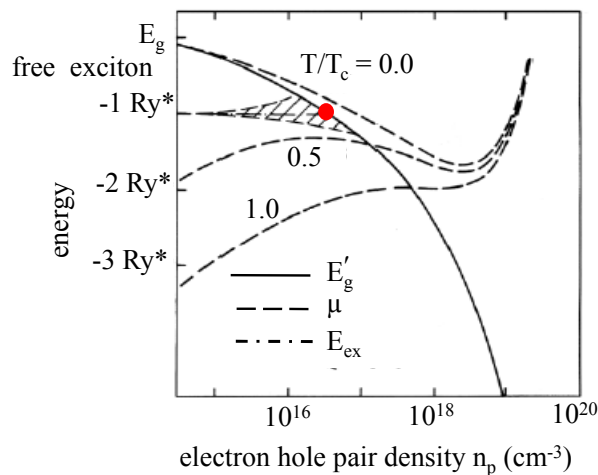


Figure 5.9 Schematic dependence of band-gap E_g' on the excited carrier density n_p (based on the numerical data for CdS) [24]

An effect due to significant carrier density may be expected when the number-density of charge carriers is of the order of Mott density of the semiconductor material. On the other hand, it is also known that the band-gap of a semiconductor material is a monotonically decreasing function of the excited carrier density. The monotonous decrease of band-gap with the increasing excited carrier density in CdS is shown as an example in Figure 5.9. In the representation, the Mott density is the density at which the curves E_{ex} and E_g' cross each other and is marked by a red point in the figure. It is visibly clear that a decrease in energy-gap occurs even when the excited carrier densities are one to two orders less than the Mott transition density. Therefore, renormalization effects can be expected when the ZnO system is excited by Pu-400 because the estimated density of excited-carriers for the excitation is just one order less than the Mott density in ZnO. The onset of absorption (i.e absorption edge) in the ZnO films occurs at around 380 nm and the relative red-shift of the absorption edge results in an absorption increase due to the relative increase in the absorption coefficient at that spectral position. A relatively stronger and broader peak is observed at a similar spectral position for the transient spectra from the sample

excited by Pu-266. This must be due to the comparatively larger density of carriers in that case. This corroborates our educated surmise that renormalization of the band-gap in ZnO must be the origin of the absorption increase centred at ~ 382 nm.

The interaction of free carriers among each other, which becomes important in case of large carrier-densities, is not included in the formalism for the ground state dielectric function of ZnO. Moreover reports on the band-structure calculations demonstrate that the carrier induced band-gap renormalization cannot be described as a rigid shift of the band-edges. This is due to the fact that though the excited carriers lower the energy of both the valence and conduction bands, it is the change in shape of the conduction band that has the strongest effect on the shift in optical transitions [99]. This physically justifies the need to incorporate this contribution as an additional gaussian curve in the model. It is evident from the experimental spectra excited by Pu-266 that the absorption increase is asymmetric with a long-wavelength tail extending upto around 420 nm. A precise simulation of the contribution thus requires not only a single Gaussian curve but a convolution of two or more such curves. However, it was found that except for the small discrepancy around 420 nm, adding a single Gaussian (centred ~ 382 nm) does not result in significant errors in the assessment of its time behaviour. The added Gaussian curve was centred at 382 nm while its amplitude as well width was allowed to change. Even though the contribution exists only for early times, the individual parameters related to it were varied over the entire time sequence to maintain a consistency in the fits. However at later times, this was found to be the cause of underestimation of parameters related to the contributions exhibiting negative optical density. To overcome this problem, constraints were introduced into the fitting routine so that the amplitude of the Gaussian cannot attain negative values. The spectral evolution of the contribution at different delay times is shown in Figure 5.10.

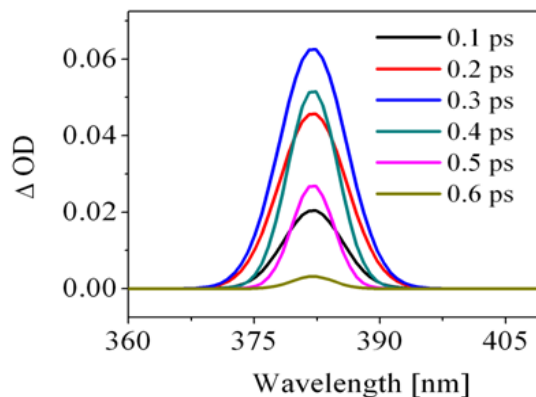


Fig 5.10 Spectral evolution of contribution from band-gap renormalization (excitation $\lambda = 400$ nm)

The contribution is seen to emerge immediately after excitation because of the instantaneous population of the conduction band (or exciton levels) by the excited charge carriers. The area under the added curve then maximizes on a time scale of around 300 fs. The contribution becomes almost zero on a time scale of ~ 700 fs after excitation which could be due to the system reclaiming its original band-gap within this time frame. However, a comparative analysis of the temporal evolution of the

contributing component, corresponding to measurements performed with different excitation fluences (discussed in detail in section 5.5.2), indicate that this is not the case. The amplitude of the renormalization peak is found to increase with increasing intensity; but further increase of the pump-fluence results in a decrease in amplitude as well as a faster decay of the contribution. In consistence with the known theory that band-gap renormalization in semiconductors increase with increasing excited-carrier density, this can be plausible only when the renormalization peak is hidden by the stronger and rapidly rising contributions from stimulated emission and bleaching at higher fluences. The coincidence of the point in time when the contribution from BGR disappears, and that from bleaching and stimulated emission approach towards its maximum supports this argument. In such a situation it is not possible to deduce the time-scale of recovery of the renormalized band-gap. Nonetheless, it can be qualitatively stated that it should occur within the first few tens of picoseconds because of the recombination of a large fraction of the excited population on this time scale as evident from the relaxation behaviour of exciton-bleaching and stimulated emission from the sample.

5.3.4 Refractive index change

The spectral modulations observed between 400 nm and 600 nm in the transient transmission spectra of ZnO are a resultant of change in its refractive index upon excitation by the pump. The electrons and the lattice are driven out of equilibrium by the intense pump pulse which in turn induces a modification of the refractive index. It has been already demonstrated in section 4.2.4 that a combined variation of the parameters ϵl_{off} and A_{ca} in the dielectric function of ZnO is required for simulation of the modulations. Figure 5.11 (a) shows an experimental and simulated spectra corresponding to a delay of 0.9 ps where ϵl_{off} and A_{ca} were varied in order to simulate the spectral modulations. Variation of the parameters results in a decrease of the refractive index, thereby shifting the interference pattern of linear transmission from the sample after excitation. This in turn gives rise to the oscillatory behaviour observed in the transient transmission spectra.

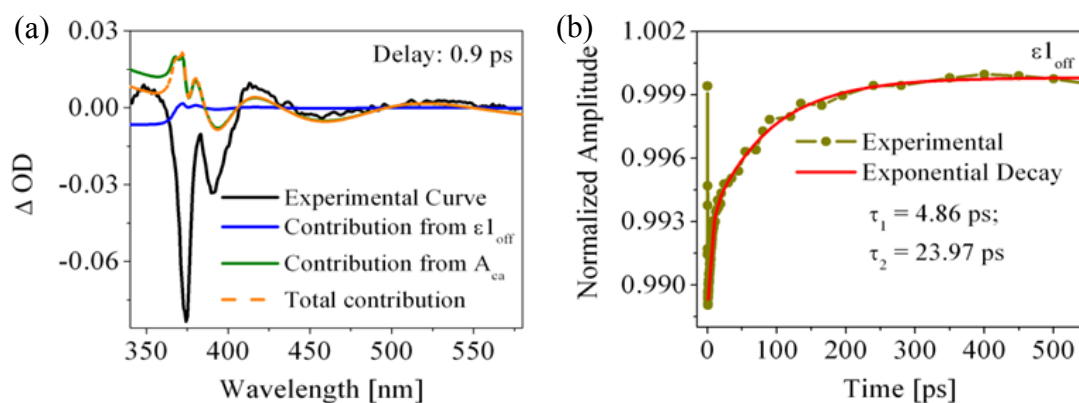


Figure 5.11 (a) Simulation of oscillations between 400 nm and 600 nm by ϵl_{off} and A_{ca} (excitation $\lambda = 400$ nm); (b) Temporal evolution of ϵl_{off}

A maximum change of 1 % for ϵl_{off} whereas that of only 0.15 % for A_{ca} could be estimated from the fits to the spectra exhibiting the highest amplitude modulations.

Therefore, $\epsilon_{1\text{off}}$ can be said to be the dominant of the two parameters, with A_{ca} being significant only at very early times. The parameter $\epsilon_{1\text{off}}$ signifies the transitions from higher lying gaps and core-excitonic transitions [32]. The time-evolution of $\epsilon_{1\text{off}}$ plotted in Figure 5.11 (b) shows a rather complex behaviour with rapid rise followed by a fast recovery for very early times. The change in the refractive index thereby rises again to exponentially decay on a time scale of ~ 5 ps and ~ 24 ps. Due to the nature of the transitions which give rise to the change in refractive index in ZnO, physical attributions to the extracted time-constants could not be realized. A negligibly small residual contribution is observed to persist for later times upto 600 ps and beyond and is attributed to the change in the electron distribution in the sample induced by the rise in its lattice temperature due to absorption of the strong pump pulse.

5.3.5 Carrier cooling and lattice heating

The absorption increase at around 377 nm developed later in the time sequence of the optical density changes (Figure 5.12 (a)) is attributed to the heating of the sample by the thermal relaxation of the hot carriers created by the intense pump-pulse.

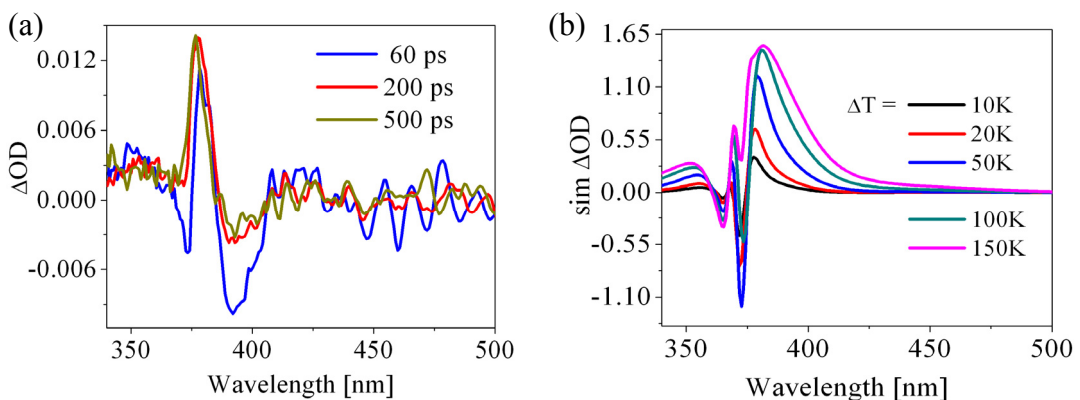


Figure 5.12 (a) Experimental and (b) Simulated spectra depicting the absorption increase caused by heating of sample.

Prior to excitation, the system and the surroundings are at thermal-equilibrium with each other. Excitation by an intense pump-pulse drives the system out of equilibrium. The initially hot carriers then attain a quasi-thermal equilibrium within the first 100 fs - 200 fs by carrier-carrier scattering processes [13, 100]. The thermalized but hot carriers subsequently transfer energy to the lattice and reach equilibrium via phonon-emission leading to an increase in the lattice temperature. This process consists of multiple scattering processes (due to small magnitude of energy carried by the emitted phonons) and therefore requires several picoseconds before the carriers and lattice can reach a thermal equilibrium [34].

Change in electron distribution induced by thermal effects results in a change of the band-gap energy in a semiconductor. In addition to that as the lattice temperature rise, elastic collision of excitons give rise to homogeneous broadening of the exciton resonances. Temperature dependent band-gap and excitonic broadening effects [84] were incorporated into the model to account for the thermal effects. The band-gap is inversely proportional to the rise in temperature; correspondingly we see an

absorption increase at around ~ 377 nm in the simulated transient optical density spectra (Figure 5.12 (b)). The complex spectral variation in the UV region comes from the induced exciton broadening. The simulated spectra exhibits an increase in the amplitude as well a red-shift of the strong contribution ~ 377 nm, and a blue shift of the positive feature at around 350 nm with increasing temperature. Once the carriers and the lattice are in equilibrium, the sample is at a well defined temperature. An approximate change in temperature of the sample upon absorption of the energy of the pump can be deduced from the equation (5.3), where c is the specific heat capacity and ρ is the volume density of ZnO, d is the thickness of the sample layer and F_p is the pump fluence.

$$\Delta T = \frac{F_p}{c \cdot \rho \cdot d} \quad (5.3)$$

Because of the small linear absorption coefficient value of ZnO at 400 nm, only a small fraction of the incident pump will be absorbed (approximately 0.3 %). This corresponds to a rise in temperature of less than 5 K. However amplitude of the peak corresponding to the estimated rise in temperature is slightly higher compared to the experimentally observed changes in optical density values. One possible reason for this could be the conduction of heat to the substrate resulting in lower lattice temperature than estimated by equation (5.3). It should be mentioned here that the amplitude of time-resolved transmission changes is significantly affected by the overlap between the pump and probe. The spot size of the probe is slightly larger than the pump at the sample surface, thus it averages the signal over the heated volume as well as non-illuminated areas. In such a scenario, the recorded amplitude of the contribution is expected to be reduced in comparison to its real amplitude. Further decrease in the amplitude of the recorded signals may occur for the case of an additional misalignment reducing the pump-probe overlap. But, this will in no way affect the spectral position of the observed peak. The coincidence of the peak position of the contribution in the simulated spectra (for the expected temperature increase) to the experimentally observed one indicates that it is indeed a signature of heating of the sample.

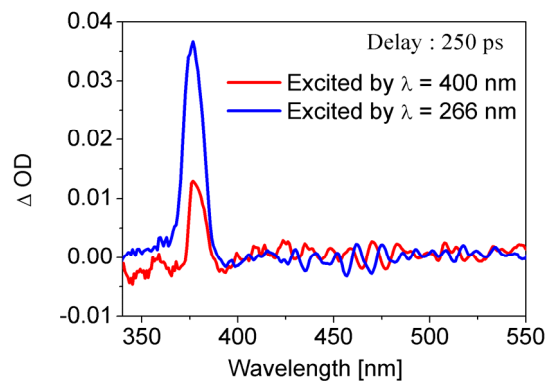


Figure 5.13 Effect of the rise in lattice temperature induced by Pu-400 and Pu-266.

The relative amplitudes of the contribution for excitation by Pu-400 and Pu-266 is plotted in Figure 5.13. Since, the absorption coefficient of ZnO is much larger at $\lambda =$

266 nm than at $\lambda = 400$ nm, the sample will absorb a larger fraction of the pump-energy when excited by Pu-266 and the increment in temperature will be higher. Given the attribution is correct this should result in relatively higher amplitude of the absorption increase at 377 nm when the sample is excited by Pu-266. That this is indeed the case is visibly clear from Figure 5.13.

5.4 Interpretation of dynamics based on the time-behaviour of contributing processes

The previous section identifies the physical processes which contribute to the transient transmission changes induced by ultrafast excitation of Z-365 by Pu-400. This could be achieved by the semi-empirical approach of analyzing the time-resolved transmission changes and (or) supported by the time-resolved measurements performed on Z-365 by Pu-266. It has also been discussed that the contributing physical processes are not mutually exclusive but significantly influence each other both in terms of the spectral as well as their temporal evolution. Thus the need for a comparative analysis of the time-behaviour of the different contributions is obviously required in order to obtain a reliable and convincing picture of the charge carrier-dynamics in ZnO. A detailed discussion of the relative time-behavior of contributing processes, along with their sequence of occurrence is presented in subsection 5.4.2. The key facts revealed by a thorough analysis of the early time behavior of processes induced by Pu-400 and Pu-266 permitted us to make important conclusions about the charge carrier dynamics. It could be inferred that in spite of the off-resonant excitation of ZnO by Pu-400, a fraction of the induced exciton population is formed as if excited resonantly. The following subsection focuses on the observations and arguments which led to this conclusion.

5.4.1 Exciton formation by the 400 nm pump-pulse

Charge-carriers excited to states higher into the conduction band need to relax to the band-minima before recombination can take place. The hot carriers thus created first thermalise by carrier-carrier scattering and attain a quasi-thermal equilibrium. This usually occurs on a time scale of $\sim 100 - 200$ fs. However the amount of energy lost by such scattering processes is not sufficient for complete relaxation of the excited species to the band-minima; and the scattering of carriers is followed by their interaction with longitudinal optical (LO) phonons. The carriers having excess energy relax towards the band-bottom through the cascade emission of multiple-LO phonons [101, 35]. However, at some stage the exciton-LO phonon scattering is suppressed because of the small density of available final states for scattering. Both exciton-acoustical phonons and exciton-exciton collision processes become dominant at this point. It has been reported that it may take a few picoseconds before the carriers can completely relax back to the band-minima [16, 102]. The time taken for relaxation depends critically on the excess energy gained by the excited species and also on the average number of thermalized phonons. Recombination of individual carriers by radiative or non-radiative decay channels can take place only after it has gone through this relaxation stage.

It has been observed that upon excitation by Pu-400, the bleaching peak emerges without a noticeable delay time (Figure 5.14 (a)). In light of the above explained paradigm we may then infer that direct formation of excitons take place. Direct transition of carriers spontaneously populates the exciton states thereby causing

saturation of further absorption and the phenomenon is termed as bleaching. Since the photon-energy of pump is less than the energy difference between the valence band and the exciton levels, these transitions can be possible only when the electrons are excited from the band-tail states to the exciton states. This process is followed by stimulated emission which occurs due to the interaction of the exciton population built up at the exciton states among each other or with free carriers. In addition to the directly formed excitons, a small fraction of indirectly formed excitons via two-photon absorption of the pump is also expected to contribute to the processes later in the time sequence. The experimental evidence in support of this argument is provided by the early time-behaviour of bleaching that occurs at exciton resonance upon excitation of the sample by Pu-266 (Figure 5.14 (b)).

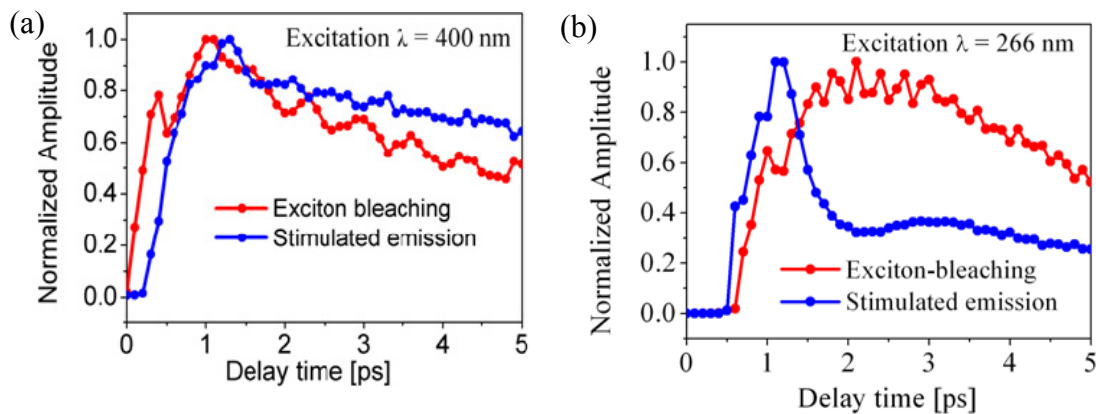


Figure 5.14 Early time behavior of exciton-bleaching and stimulated emission for excitation with (a) $\lambda = 400$ nm and (b) $\lambda = 266$ nm

In contrast to the sub-gap photon energy offered by Pu-400, the photons corresponding to Pu-266 have an excess energy of around 1.35 eV to dissipate before it can relax to the $n = 1$ exciton state. This explains the relatively delayed emergence of the bleaching peak at ~ 800 fs after excitation. It should be noted that the observed time delay is much larger than the error bar of time-zero determination in our case (section 4.1.4), which renders this explanation a reliable one. Stimulated emission in this case occurs at around 1.3 ps, which is well ahead of the time scale of ~ 2.1 ps required for the bleaching contribution to reach its maximum. But stimulated emission due to exciton-recombination processes is most efficient only when the exciton population is maximum in the exciton states [95]. Hence we can say that direct recombination of electron hole pairs existing in the plasma state must be the origin of the observed emission. Given the high-density of excited carriers generated by the 266 nm pump pulse, formation of electron-hole plasma is indeed expected. In this context the transmission increase at 375 nm observed in the transient spectra excited by Pu-266, might be arising from the instability of exciton states and not due to the band-filling effect for early times. As the density of carriers reduces by recombination the exciton states are stabilized and maximum of the bleaching peak (this time from population of exciton states) occurs at around 2.1 ps. However the transmission increase at exciton resonance either from overpopulation (hence unstable) or from population of exciton states does not appear before a delay time of

~ 800 fs. This augments well to our argument regarding the direct exciton formation by the Pu-400 pump pulse which essentially remains valid.

5.4.2 Sequence of processes in the dynamics of ZnO

We have seen that excitons play a crucial role in the charge carrier dynamics of photo-generated carriers in ZnO sample. When the sample is excited by the Pu-400 pump pulse, the strongest contributions to the transient spectra originate from exciton-bleaching, stimulated emission and renormalization of the band-gap in ZnO. The early time behavior of these contributions is plotted in Figure 5.15.

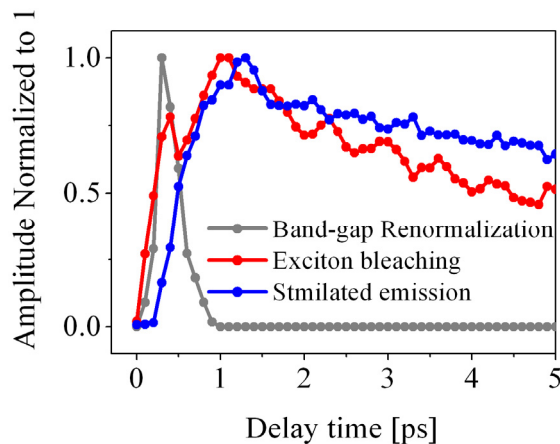


Figure 5.15 Comparison of the early time evolution of contributing processes (excitation $\lambda = 400$ nm)

The parametric values related to each contribution have been normalized to show similar amplitudes (with the maximum corresponding to a value of 1) for a better comparison of the time sequence. While comparing the sequential rise of the contributions we should remember that the response during the early times ~ 100 fs should not be included in the discussion of dynamics because within this time frame both coherent processes as well as incoherent processes contribute to the transient spectra. It is clear from Figure 5.15 that the contributing processes overlap in time forming a continuous chain of events. The contribution from exciton-bleaching and band-gap renormalization are the first to emerge after excitation by Pu-400. Maximum of exciton bleaching is observed at ~ 1 ps and that of the band-gap renormalization occurs at ~ 0.3 ps. Stimulated emission appears later in the time sequence at ~ 0.4 ps and shows a slower rise as compared to exciton bleaching. Keeping in mind the sequence of processes and their decay behavior, the following dynamics of the photo-excited carriers is proposed and the proposed scheme is illustrated by a band picture presented in Figure 5.16.

Excitation of Z-365 by Pu-400 pulse leads to the transition of a large fraction of electrons from the band-tail states to the exciton levels by single photon absorption process. Simultaneous to that a smaller fraction of carriers are excited higher into the conduction band states by multi-photon absorption, presumably two-photon absorption due to the close proximity of the band-edge to the excitation wavelength. The charge carriers excited higher into the conduction band are expected to relax and contribute to the exciton population later in the time sequence. The induced exciton

population leads to bleaching of exciton states and hence a transmission increase is observed at exciton-A resonance (i.e. ~ 375 nm). However, the high density of exciton population leads to the renormalization of the band-gap energy; and so an absorption increase at around 382 nm is observed to grow in concurrence to the rise of the bleaching peak. Renormalization of the band-gap energy further stabilises the exciton states leading to maximum bleaching of the exciton states at ~ 1 ps. In addition to the above mentioned induced processes, the sudden change in the electron distribution by the pump also leads to change in the refractive index of the sample, thus giving rise to spectral modulations almost without a noticeable delay time after excitation.

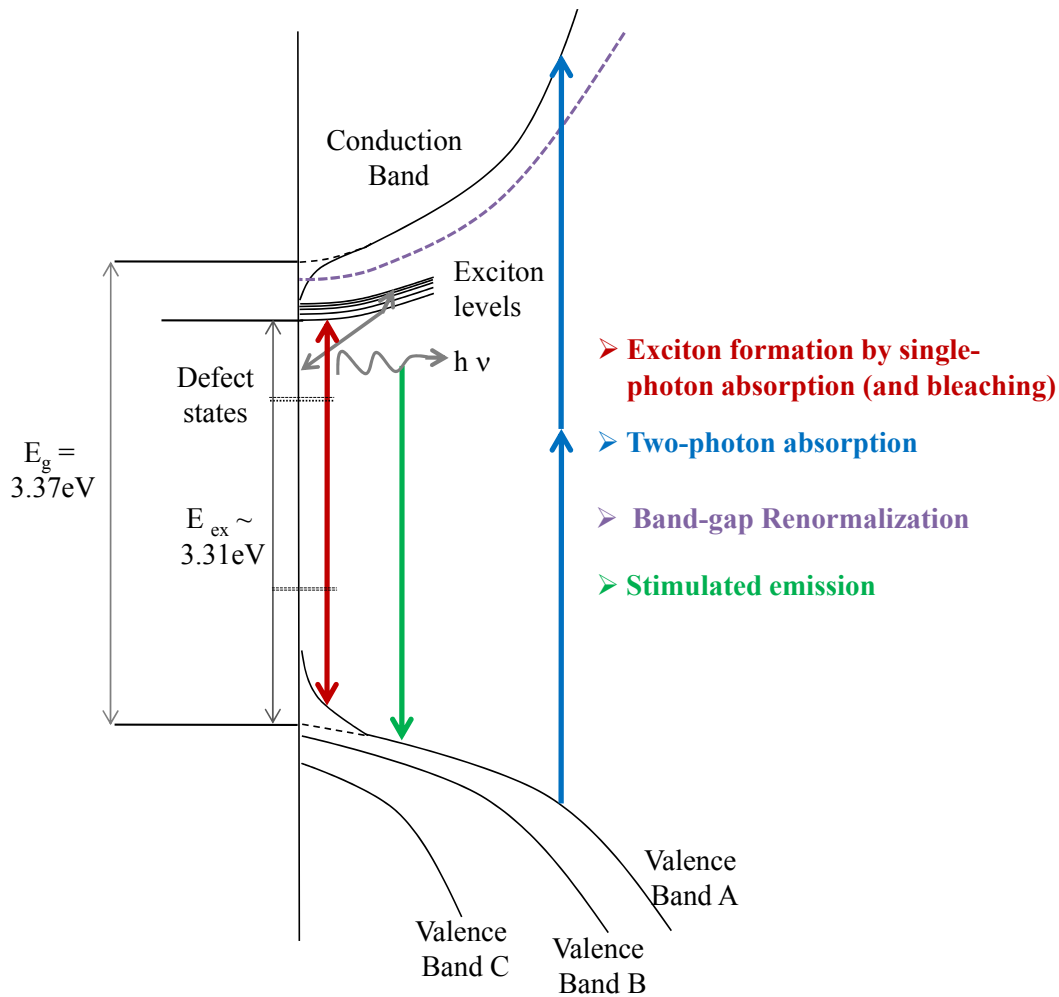


Figure 5.16 Schematic of band-structure illustrating various processes in carrier dynamics of ZnO

The second stage of the dynamics involves the recombination of the excited carriers. Annihilation of the exciton population by means of radiative as well as non-radiative recombination processes occurs on a time scale of ~ 100 ps. The non-radiative recombination processes include the trapping of charge carriers by intrinsic defect states present in the ZnO sample which correspond to a time-constant of ~ 2 ps. The radiative recombination of the exciton-population by the exciton recombination

processes gives rise to the stimulated emission at around 385 nm. A slightly delayed and slower build up of stimulated emission in comparison to exciton bleaching in Figure 5.15 confirms this argumentation. The stimulated emission decays bi-exponentially with time constants of ~ 8 ps and ~ 70 ps on a time scale of around 200 ps. The smaller time constant is attributed to the decrease in the exciton-population by recombination while the comparatively larger time constant is attributed to the slow and gradual recombination of electrons trapped into shallow trap states with the deeply trapped holes within the band-gap. The time-scale at which the renormalized band-gap of ZnO reclaims its original value could not be determined. However, keeping in mind the physical origin of the process of band-gap renormalization, it would not be incorrect to speculate that it should occur well ahead of the complete recombination of the excited population.

The cooling of the carriers (driven out of thermal equilibrium by the intense pump-pulse) via phonon-emission occurs in tandem with these processes. This results in the rise of the lattice temperature on a time scale of around 50 ps. An increment in the lattice temperature leads to a decrease in the band-gap and hence absorption increase at around 377 nm. Complete thermalization of the lattice with the surrounding exceeds the measured time range of 600 ps.

5.5 Intensity dependence of dynamics

To investigate the influence of input intensity on the charge carrier dynamics of ZnO, time-resolved measurements were performed with excitation fluences of 16 mJ/cm^2 , 32 mJ/cm^2 , 48 mJ/cm^2 , 64 mJ/cm^2 and 79 mJ/cm^2 respectively and the experimentally obtained spectra were then modeled and analyzed with care. The contributing processes to the transient spectra were found to be strongly influenced by the input-photon flux. As an archetype of this study the intensity dependence of the transient response of Z-365 is presented here. The following sub-sections focus on the response of the physical contributions to the change in input photon flux.

5.5.1 Exciton-bleaching and stimulated emission:

The amplitudes of exciton bleaching and stimulated emission were observed to increase with the increasing input intensity (Figure 5.17). The bleaching peak at 375 nm could be successfully simulated by decreasing the amplitude of the discrete exciton-A, at all pump fluencies. For simulation of stimulated emission, the amplitude as well as width of the Gaussian taking it into account was varied while the peak position was kept constant at $(387 \pm 3) \text{ nm}$. The time evolution till 20 ps , corresponding to different pump-fluences for exciton bleaching and stimulated emission is shown in Figure 5.18 (a) and (b) respectively.

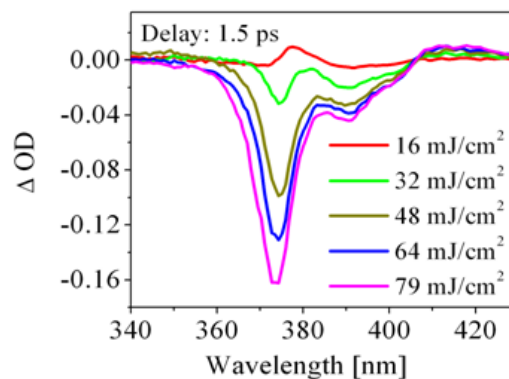


Figure 5.17 : Spectral variation of discrete exciton bleaching and stimulated emission at 1.5 ps with increasing excitation energies

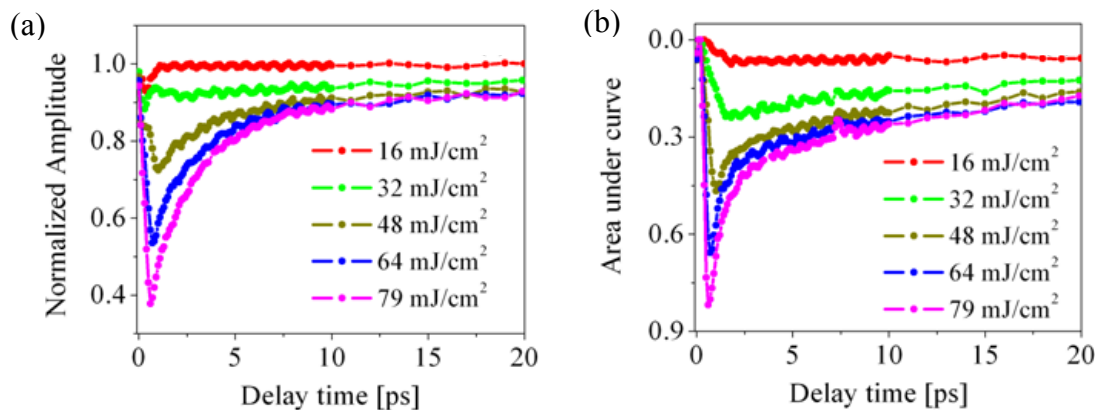


Figure 5.18 : Early time evolution of (a) Exciton bleaching (b) Stimulated emission

The rise time of stimulated emission clearly show a monotonous decrease with increasing excitation energy. This must be due to the enhancement in carrier-generation rate [26] with the increasing photon-flux. Assuming that absorption of each photon directly causes the generation of electron-hole pairs, the generation rate G is can be determined by the following equation.

$$G = \alpha N_0 e^{-\alpha d} \quad (5.4)$$

where α is the absorption coefficient, d is the distance into the material at which the generation-rate is measured and N_0 is the incident photon-flux. For a given thickness and absorption coefficient, the generation rate is found to be directly proportional to the pump-energy. The exciton levels will be thus be populated faster at higher pump-fluences resulting in the occurrence of the exciton-interactions earlier in the time sequence. A similar trend is observed for early time evolution of the contribution from exciton bleaching. It should be mentioned here that the anomalous rise time of bleaching for the low pump energies must be due to competition between the absorption increase from BGR and the weaker bleaching peak at such low intensities.

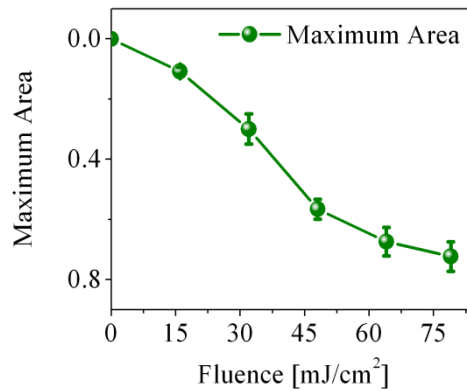


Figure 5.19 : Maximum area of stimulated emission, as a function of pump fluence

It has already been shown in Figure 5.1 that amplitude of exciton bleaching increases non-linearly with increasing intensity. This should be due to the fact that two-photon absorption being a non-linear process will become more efficient at relatively higher intensities. The maximum amplitude of stimulated emission as a function of the pump-energy is plotted in Figure 5.19. The contribution shows a non-linear increase for fluences upto 48 mJ/cm²; but further increase in intensity results in saturation of the emission.

The bi-exponential decay behaviour of both the contributions was maintained at all excitation energies. The decay constants for exciton bleaching and stimulated emission corresponding to the excitation energies from 48 mJ/cm² to 79 mJ/cm² is tabulated in Table 5.1 and Table 5.2 respectively. The input intensity does not seem to have a significant influence on the rate of decay of exciton bleaching except for the amplitudes of the decay components. The ratio of amplitudes of the fast component to the slower component increases with the increasing excitation intensity. This is an indication that the trapping process becomes more efficient with the increasing availability of carriers.

Fluence	Decay constants (ps)		Amplitude Ratio
	τ_{1b}	τ_{2b}	A_{1b}/A_{2b}
48 mJ/cm ²	2	28.5	1.62
64 mJ/cm ²	2.1	29.8	2.56
79 mJ/cm ²	2.3	29	3.62

Table 5.1: Decay-constants (relative error $\sim 8\%$) for bleaching contribution corresponding to different excitation energies

Fluence	Decay constants (ps)		Amplitude Ratio
	τ_{1s}	τ_{2s}	A_{1s}/A_{2s}
48 mJ/cm ²	7.9	75.8	2.49
64 mJ/cm ²	8.2	70.5	2.01
79 mJ/cm ²	11.9	53.7	3.21

Table 5.2: Decay-constants (relative error $\sim 8\%$) for stimulated emission corresponding to different excitation energies

On the other hand, for the case of stimulated emission it is observed that the first decay component becomes slower with increasing input intensity while the slow component becomes faster. The increase in the density of trapped population at higher fluencies due to the increase efficiency of trapping must lead to an increase in their rate of recombination. This explains the trend observed for the slow time component. However a precise interpretation for the trend observed for the smaller of the decay constants could not be ascertained. Nonetheless it can be speculated that two or more decay channels contribute to this time constant at low intensities. As the intensity increases one or more of them might be blocked due to saturation or other effects which leads to an increase of the decay constant at higher fluences.

5.5.2 Intensity dependence of band-gap renormalization:

The absorption increase at ~ 382 nm attributed to band-gap renormalization is observed at all pump-intensities (Figure 5.20(a)). However, the magnitude of the absorption increase shows an interesting trend with increasing input intensity. An enhancement of the peak is observed when the pump-fluence is increased from 16 mJ/cm² to 32 mJ/cm², but on further increase of the input energy, the effect of renormalization seems to be diminished. The excited carrier density increases non-linearly with the increasing pump-fluence (clear from last subsection) and in consistent to the known theory of band-gap renormalization the band-gap energy should decrease monotonously with increasing intensity. In this context the only physically plausible explanation for the experimentally observed behavior could be

that the increase of the BGR peak is masked by the non-linearly increasing peak from optical gain at higher intensities.

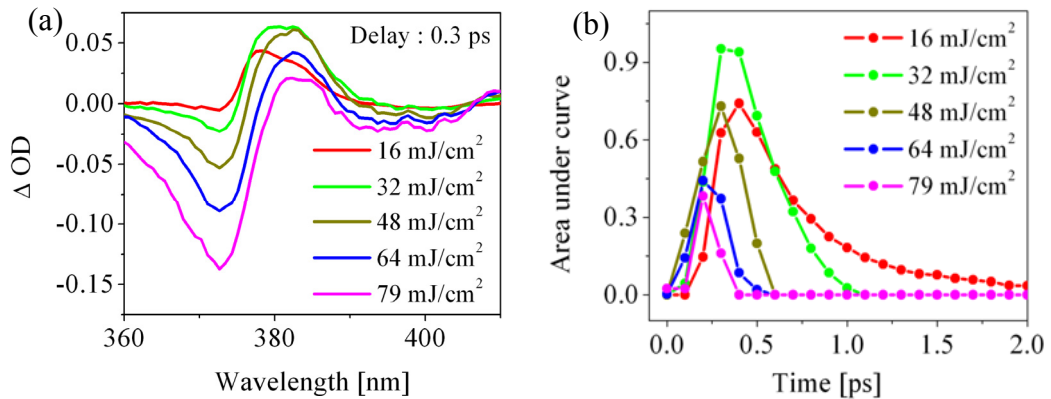


Figure 5.20: (a) Spectral variation at 0.3 ps and (b) Temporal evolution of area as a function of excitation energies for the band-gap renormalization effect

Both width and amplitude of the Gaussian curve added to describe the contribution was varied while the spectral peak position was kept constant at 382 nm. The area under the curve for the contribution as a function of time for different pump-intensities is plotted in Figure 5.20 (b). It is observed that the time scale till which the absorption increase persists before being overtaken by the stronger components, decrease with the increasing input intensity. This can be explained as an effect of the faster rise of the contribution from stimulated emission and exciton bleaching with increasing intensity. The increase in the rise time of the relatively weaker stimulated emission and exciton bleaching peak at lower intensities allows for the renormalization peak to be observed for a comparatively longer duration at lower fluences. This consistency of the temporal behaviour of the BGR and stimulated emission (and exciton bleaching) contribution among each other further reaffirms that our interpretation is indeed correct.

5.5.3 Intensity dependence of refractive index change and rise of lattice temperature

The amplitude of the modulations in the range of 400 nm to 600 nm is observed to increase with the increase in the pump-fluence (Figure 5.21 (a)).

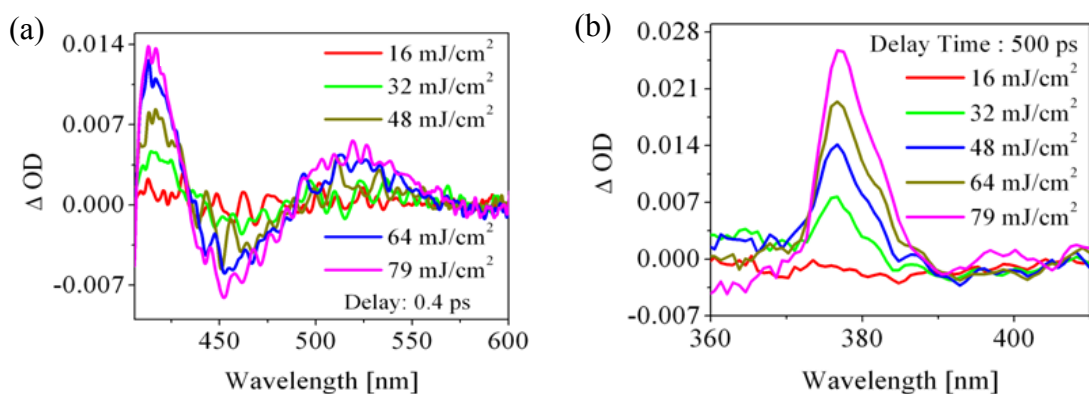


Figure 5.21 Spectral variation of (a) oscillations at 0.4 ps and (b) absorption increase corresponding to thermal effects at 500 ps, for different excitation energies

This would mean that a greater deviation of the refractive index from its original value is induced by the higher intensity pump-pulses. Both $\epsilon_{1\text{off}}$ and A_{ca} were varied in the model for simulating the observed modulations. The evolution of the respective parameters over the measured time sequence corresponding to different input-intensities is shown in Figure 5.22 (a) and 5.22 (b). It is evident from the graphs that the contribution of A_{ca} is almost negligible at low intensities and becomes significant only when the photon-flux increases.

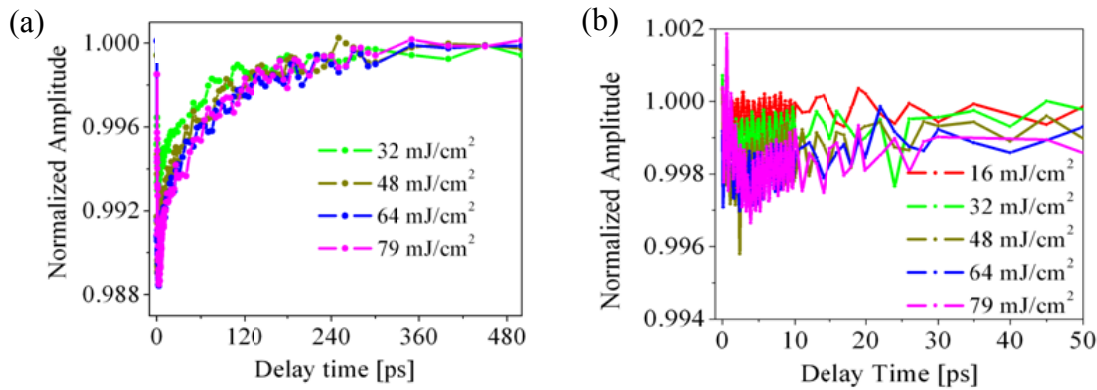


Figure 5.22 Temporal evolution of (a) $\epsilon_{1\text{off}}$ and (b) A_{ca} for different pump-energies

We have already discussed that the long-delay absorption increase in the transient transmission spectra is an effect of increase in temperature of the sample. With the increase of pump-fluence, more energy will be absorbed by the sample due to the increase in the photon flux. This in turn will result in a greater difference of temperature between the sample before and after excitation at higher fluences. The behaviour of the peak at ~ 377 nm is in line with our expectations (Figure 5.21 (b)). Increase in amplitude as well as red-shift of the peak position both of which are signatures of higher lattice temperatures, is clearly visible. Moreover, it was observed that the long time-residual component of the refractive index (attributed to thermal effects) also increases with the increase in pump-intensity further reflecting the higher increase in temperature for higher excitation fluences. In light of above observations we may safely conclude that attribution made to the long-time modulations and the peak at ~ 377 nm is indeed true.

5.6 Effect of layer thickness on the femtosecond response of ZnO films

Time-resolved measurements were carried out on Z-365, Z-186 and Z-100 in order to investigate the influence of sample's layer-thickness on the femtosecond response of ZnO. The samples with their respective thicknesses of 365 nm, 186 nm and 100 nm, were chosen arbitrarily and are comparable in all respects except for their thickness and the crystallite size. The average crystallite size was found to increase with the increasing thickness of the sample layer. All measurements were done under the similar experimental conditions; and the fluence was kept constant at 48 mJ/cm^2 . The transient transmission signals at different delay times for the respective thin film samples are shown in Figure 5.23 (a), (b) and (c).

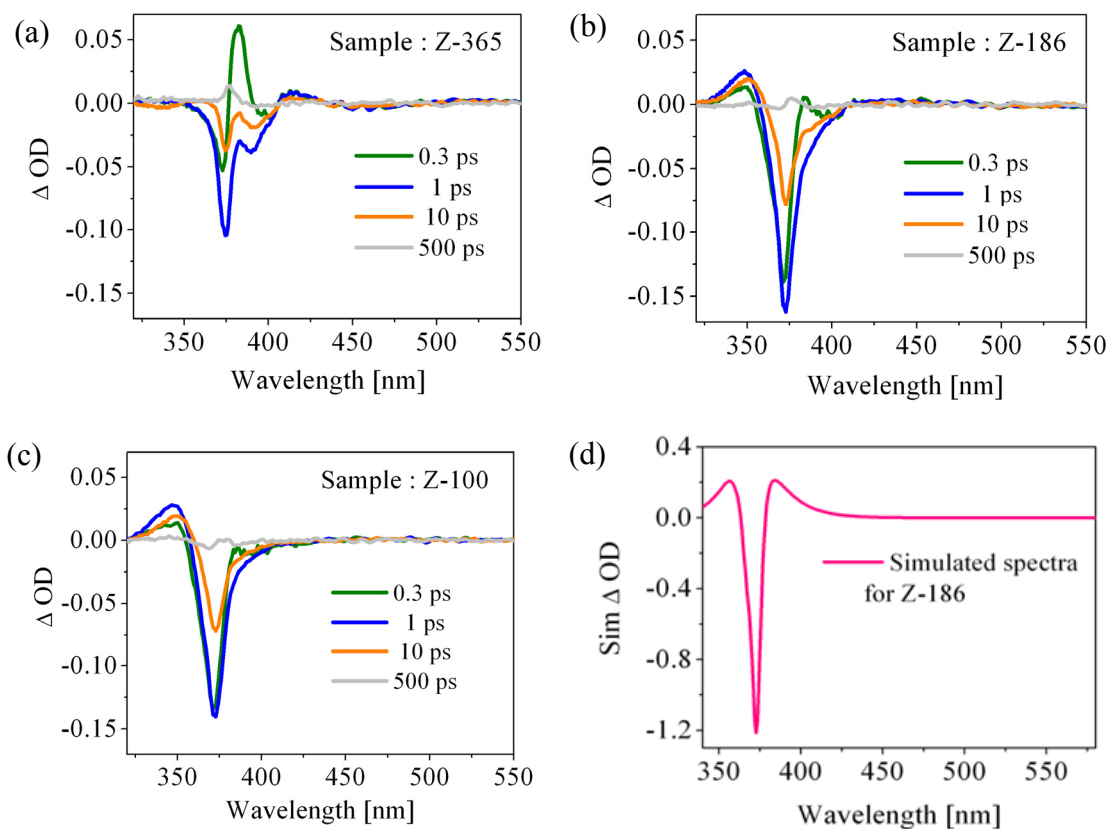


Figure 5.23 Change in optical density as function of wavelength (a) Z-365, (b) Z-186 and (c) Z-100 at different delay times; (d) Simulated spectra of Z-186 for 36 % increase in exciton broadening

The most prominent peak observed for the transient spectra of the samples is the bleaching at 375 nm. The amplitude of the induced transparency is clearly much higher in the thinner Z-100 and Z-186 samples as compared to the thicker Z-365. The amplitude as well as period of the modulations observed from 400 nm to 600 nm also seems to be unique to each sample. Among others, the effect from band-gap renormalization at 382 nm and the transmission increase at 390 nm due to stimulated emission seems to be abated in the thinner samples. The resultant of the lattice

heating (absorption increase at 377 nm) is also observed later in the measured time-sequence by all the samples. In addition to the already identified spectral contributions, an absorption increase in the UV region of the spectrum is observed only for Z-186 and Z-100 samples. This contribution to the spectrum is centered at 350 nm and spans over a spectral range of 328 nm to 362 nm. It is found to emerge immediately after excitation by the pump and contribute to the spectra on a time scale of around 150 ps. The origin of the UV-component (observed for the thinner samples) could not be determined with certainty. Changing the parameter related to excitonic broadening in the dielectric function of ZnO results in a double-winged transmission increase in the transient spectra (shown in Figure 5.23 (d)). The spectral position of the experimentally observed positive optical density peak coincides with the extreme edge of the blue-wing of the simulated feature. Both elastic as well as inelastic collisions among the excitons may occur when a high density of exciton population is generated by an excitation pulse. The inelastic collisions give rise to stimulated emission whereas the elastic collisions result in a broadening of the exciton resonance [103, 1]. Because of the high intensity pump-pulses used excitonic-broadening could be considered as the possible origin of this contribution. The absence of the peak in the spectra from Z-365 sample could be attributed to the complete attenuation of the supercontinuum probe (lower in intensity for the UV wavelengths) on transmitting through the thick and absorbing ZnO layer. However, the high amplitude of the peaks at ~ 375 nm and ~ 380 nm in the simulated spectra (not observed for the experimental spectra) still remains an open issue.

The following sub-sections are dedicated to the analysis of the known contributions to the transient spectra of the different ZnO samples.

5.6.1 Exciton bleaching for different ZnO films

The amplitude of discrete exciton-A was varied in the model for simulating the bleaching peak in the transient spectra. In addition to that, a contribution from discrete exciton-B was also observed for the Z-186 and Z-100 samples. The time sequence of the exciton-A and exciton-B bleaching thus obtained was unable to reveal any specific trend about the influence of thickness on the rate of exciton-recombination. However the difference in magnitude of the contribution can be qualitatively explained on the basis of the difference in the crystallite sizes of the samples. It has been reported that excitonic absorption is significantly enhanced with the decrease in the nanocrystallite size in semiconductors [104, 105]. With the decrease in crystallite size, the confinement imposed on the relative motion of the electron-hole pair enhances the oscillator strength and hence the absorption coefficient at the exciton resonance. The determined crystallite sizes for Z-186 and Z-100 is comparatively much smaller than that for Z-365. This explains the significantly enhanced exciton-bleaching contribution in Z-186 and Z-100 samples.

5.6.2 Influence of thickness on band-gap renormalization

The absorption increase at 382 nm attributed to band-gap renormalization could be observed only for the thicker Z-365 sample (Figure 5.24 (a)). It has already been discussed that the effect of renormalization induced by Pu-400 is much weaker compared to that induced by Pu-266. Therefore, in order to conclusively elucidate the effect of thickness on the band-gap renormalization effect, the spectra from the

samples excited by Pu-266 was additionally compared (Figure 5.24 (b)). It is evident from the plots that, the contribution from band-gap renormalization on the transient spectra becomes more prominent with increasing thickness of the samples. The decrease in the magnitude of the renormalization peak for the thinner films can be attributed to the enhanced influence of the surface properties with the decreasing thickness of the sample layer.

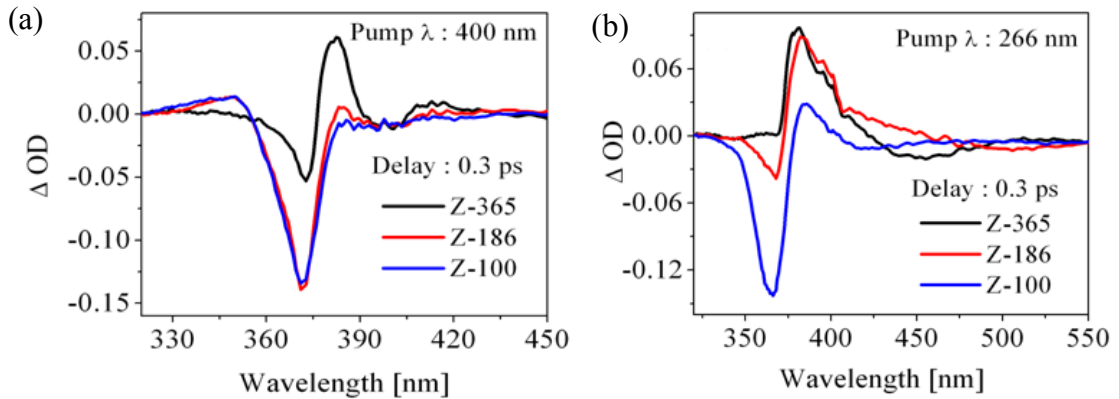


Figure 5.24 : Spectral variation of band-gap renormalization at 0.3 ps for excitation wavelength (a) 400 nm and (b) 266 nm

The frequency of interaction of excited carriers with the surface critically depends on the thickness of the films. Free carriers may be trapped on impinging the surface due to presence of surface states [106, 107]. Smaller the thickness, higher the frequency of the carrier-surface interactions and thus the probability of carriers being trapped increases. Band-gap renormalization is directly dependent on the density of the excited carriers. Hence the reduction in the excited-carrier density via trappings and fast carrier escape from the region of measurement within the first few picoseconds after pumping ought to reduce the effect of band-gap renormalization. This is quite probable because carrier diffusion has been observed to occur on a time scale of $\sim 2\text{-}5$ ps in ZnO [108]. However the rise time of the renormalization peak remains unaffected with the changing thickness of the studied systems.

5.6.3 Increase of stimulated emission with the increasing thickness

The contribution from stimulated emission has been simulated for the different samples. It is evident from the simulated curves presented in Figure 5.25 (a) that the contribution to the spectra from stimulated emission increases with the increasing thickness of the samples. It is well known that for optical energy propagating in an extended medium, the number of photons emitted by stimulated processes is directly proportional to the active length of the medium. This is because of the fact that the number of emitters increase with the increased excited volume of the sample [57]. For this reason, we observe higher amplitude stimulated emission with the increasing thickness of the ZnO layer. In addition to the influence from thickness of the sample layer, difference in crystallite size of the different ZnO samples could also contribute to the difference in their emissive properties. There have been several reports about the strong influence of the crystalline properties like nanocrystal size, grain

boundaries and dislocations etc. on the intensity as well as net rate of stimulated emission in a material [109, 4, 110].

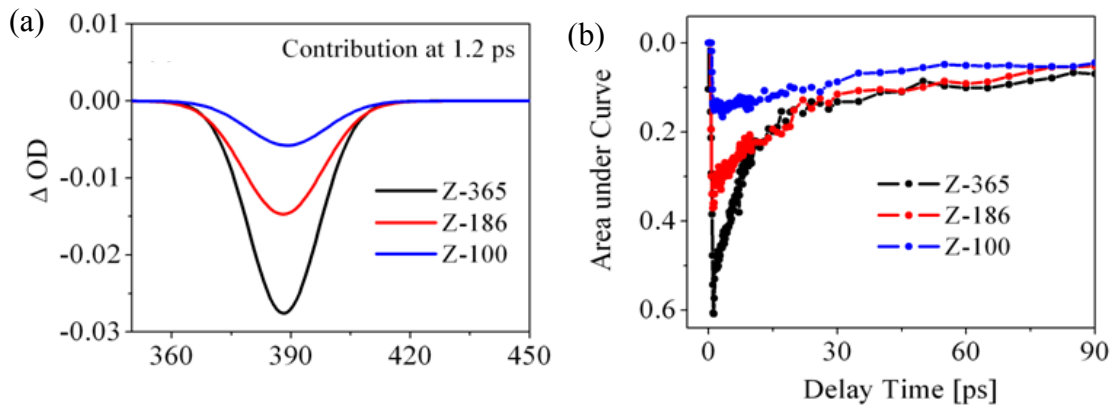


Figure 5.25: (a) Spectral variation at 1.2 ps and (b) Temporal evolution, of stimulated emission for different ZnO samples

Sample	Decay constants (ps)		Amplitude Ratio
	τ_{1s}	τ_{2s}	A_{1s}/ A_{2s}
Z-365	7.9	75.8	2.49
Z-186	16.3	123	2.88
Z-100	30.3	956	3.21

Table 5.3: Decay-constants (accurate within $\sim 8\%$ relative error) for stimulated emission corresponding to different ZnO samples

A poor crystal quality in terms of larger intrinsic defects or grain boundaries results in larger threshold for emission due to the numerous optical losses suffered due to the structural defects. The crystal quality on the other hand is said to become superior with the increasing thickness of samples due to the relative reduction of strain (resulting from the lattice mismatch between the substrate and sample layer). This could be one of the reasons why we see the amplitude of stimulated-emission elevating as the thickness of the sample increases. The temporal evolution of the area under the added gaussian curve for the respective samples is shown in Figure 5.25 (b). Time constants corresponding to the bi-exponential decay behaviour (Table 5.4) of the emission reveal that, the rate of charge-carrier recombination decrease with the decreasing thickness (and/or crystallite size) of the samples.

5.6.4 Thickness dependence of modulations

Among others, thickness of the thin films is expected to have a significant influence on the modulations observed in the transient transmission spectra. The period and amplitude of the modulations in the transient spectra is determined by the

interference modulations in the linear transmission spectra, which in turn is sensitive to the change in thickness as well as refractive index. The amplitude of the spectral modulations shows an enhanced increase with the increasing thickness for the same amount of refractive index change. As an illustration the simulated spectra showing the modulations corresponding to change in refractive index induced by 1% decrease of $\epsilon_{1\text{off}}$ for the different sample layer thicknesses is presented in Figure 5.26 (a). Therefore we observe higher amplitude and smaller period of the modulations for the spectra corresponding to Z-365 as compared to Z-186 and Z-100 (Figure 5.26 (b)). The spectral modulations for all samples were modelled by variation of A_{ca} and $\epsilon_{1\text{off}}$. Temporal evolutions of the obtained parametric values reveal that the decay behaviour of interference contribution to the time resolved spectra is independent of the film thickness.

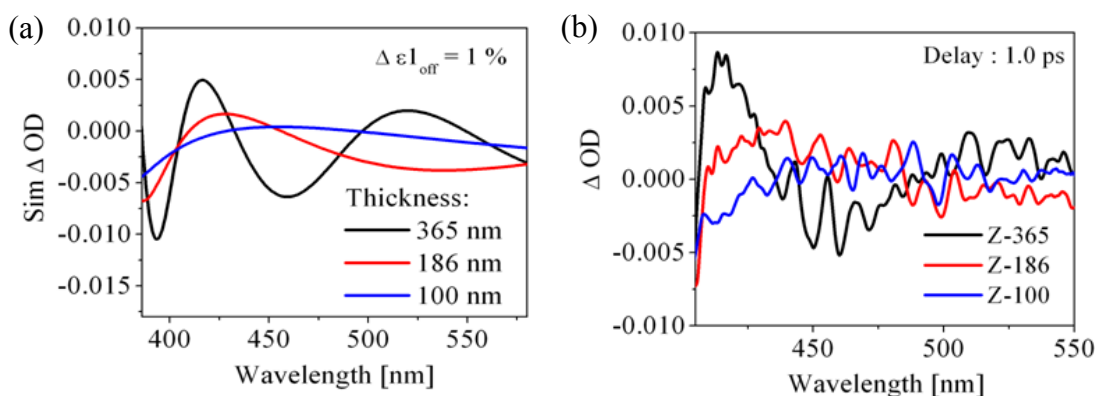


Figure 5.26 : (a) Simulated modulations for 1% decrease of $\epsilon_{1\text{off}}$ and (b) spectral variation of oscillations for different ZnO samples

The amplitude of the contribution at 377 nm ensuing from heating of the sample was observed to be higher for the thicker films. However this does not necessarily mean a higher increase in temperature for the thicker samples. Since we measure the change in ΔOD , even an identical rise in lattice temperature will lead to a larger increase in the measured change in optical density for the thicker samples.

5.7 Summary

A detailed study of the ultrafast charge carrier dynamics of ZnO thin films have been presented in this chapter. Femtosecond time resolved pump-probe spectroscopy was performed on Z-365 using 400 nm ultrashort pulses. The obtained data were analysed and interpreted with the help of a semi-empirical model and similar experiments performed on the sample with 266 nm pump pulses. The different physical processes contributing to the transient transmission spectra were identified and their evolution in time was studied meticulously.

From the study it could be concluded that exciton levels are populated by direct transition of electrons from the band-tail states to exciton levels, leading to bleaching of exciton states. With the increase in population of excitons, exciton-exciton interactions and interaction of excitons with other carriers give rise to stimulated emission. The decay dynamics of exciton bleaching was found to be bi-exponential with time constants of ~ 2 ps (attributed to trapping of carriers by defect states) and

~ 20 ps (credited to exciton annihilation by scattering processes). On the other hand the decay of stimulated emission, which was also found to be bi-exponential, is attributed to a combined affect of the excitonic scattering processes (~ 8 ps) and recombination of trapped carriers (~ 70 ps). Due to the high intensity pump-pulses used and consequently a high density of excited carriers created, many body interactions like band-gap renormalization were quite prominent at early times. Spectral modulations due to change in refractive index of ZnO (brought about by core-excitonic transitions and higher order transitions) has also been observed. The later time dynamics of ZnO is mainly dominated by thermal effects resulting from heating of the sample by the absorption of the strong pump.

All the above mentioned ultrafast processes have been observed to be appreciably influenced by the intensity of excitation. A manifestation of this is the comparatively smaller rise time of exciton bleaching and stimulated emission due to faster build of the exciton population with increasing intensity. Other effects include increase in amplitude of the spectral modulations with the rising input intensity; and a non-linear increase of exciton bleaching and saturation like behaviour for stimulated emission at higher intensities. The contribution from renormalization of band-gap was however masked by the stronger contributions from bleaching and stimulated emission at higher fluences. The time-behaviour of exciton bleaching was found to be unabated by the changing intensity. But the decay constants of stimulated emission for spectra obtained at different fluences revealed that the recombination of trapped occurs faster with increasing input intensity.

The study of layer thickness dependence reaffirmed the fact that the structural properties of a system critically influence its optical properties. The samples having smaller crystallite size showed an enhanced contribution from exciton bleaching. This is thought to be due to the increased exciton oscillator strength in the smaller crystallites because of enlarged confinement effects. On the other hand a comparatively higher stimulated emission for thicker films is attributed to the conjugate influence of improved crystalline quality and increase in the number of emitters in thicker films. A similar behaviour for the renormalization effect has been ascribed to lesser carrier-surface interactions for thicker films resulting in a decreased probability of carrier trapping. The decay of stimulated emission contribution revealed that that the rate of charge-carrier recombination increases with the increasing thickness (and/or crystallite size) of the films. The change in refractive index was found to be uninfluenced by the changing thickness of the ZnO films. The higher amplitude and smaller period modulations for the thicker films was found to be purely an effect from layer thickness of the samples.

Chapter 6. Ultrafast Dynamics of BaTiO₃/ZnO heterostructures

This part of the thesis is dedicated to the study of charge carrier dynamics of BaTiO₃/ZnO thin films which includes the dynamics of the individual ZnO and BaTiO₃ (BTO) layers in the heterostructure configuration, as well as any effects which may occur at the interface of the two materials. A complete understanding of the dynamics of each individual layer in the heterostructure is an essential prerequisite to such an investigation. Since, a comprehensive picture of the charge carrier interactions in ZnO thin films has been discussed in the preceding chapter, this segment begins with a discussion of the pump-pulse induced dynamics in a single-layer BTO film on a-plane sapphire (B-82). In the subsequent sections, results of time-resolved measurements performed on the BTO/ZnO samples and interpretation of the acquired transient data is presented. A thorough analysis of the transient data in cognizance with the knowledge of the dynamics in ZnO and BTO reveals a qualitative picture of the dynamics in the double layered BTO/ZnO samples.

6.1 Femtosecond dynamics of BTO

6.1.1 Experimental response of BTO

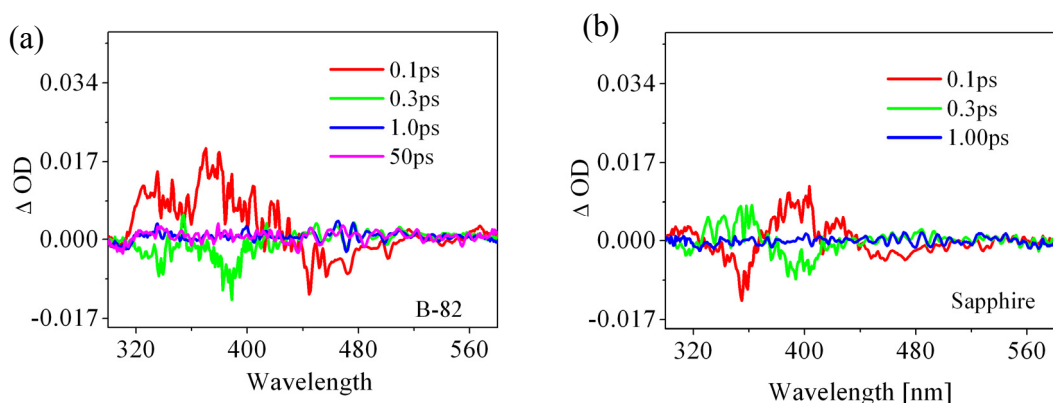


Figure 6.1 Time-resolved spectra of (a) B-82 and (b) a-plane sapphire plate (Excitation $\lambda = 400$ nm)

Time-resolved measurements were performed on B-82 using Pu-400 (fluence: 47 mJ/cm²) as well as with Pu-266 (fluence: 10 mJ/cm²). It was observed that excitation by 400 nm laser pulses, which is far from the resonance of BTO at 337 nm, does not

induce a significant transmission change in the BTO sample. The recorded spectra corresponding to different delays ranging from 0.1 ps to 50 ps is shown in Figure 6.1 (a). The random signals observed for very early times do not arise from the BTO layer but from the coherent interaction of the pump-pulse with the sapphire substrate. This is visibly clear from the time resolved spectra of a-plane sapphire plate presented in Figure 6.1(b). In contrast to that, strong changes in the transmission from the sample could be observed upon excitation with Pu-266, which has photon energy higher than the band-gap energy of BTO. The spectra for selected delay times upto 1 ps and 450 ps are presented in Figure 6.2 (a) and (b) respectively.

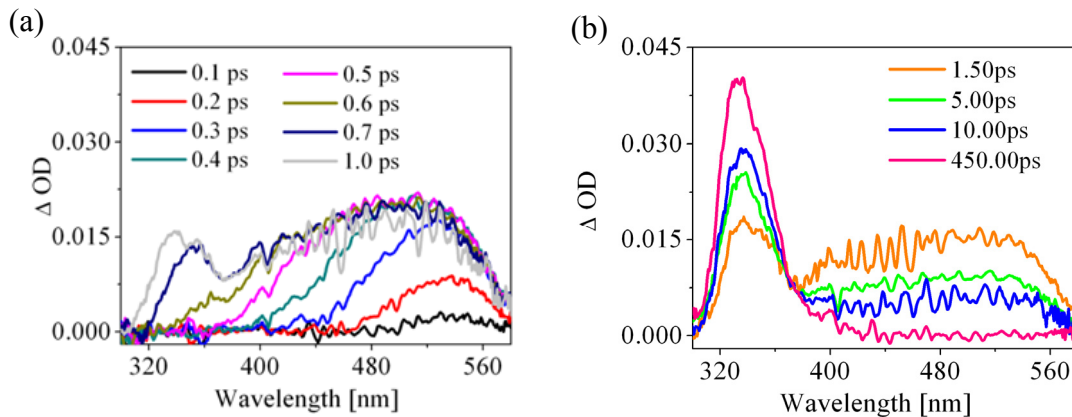


Figure 6.2 Time resolved spectra of B-82 for selected delay times (a) upto 1 ps and (b) from 1.5 ps to 450 ps (Excitation $\lambda = 266$ nm)

The spectral variation is characterised by a broad absorption increase in the visible region and a positive ΔOD peak centred at ~ 340 nm. The enhanced absorption in the visible region (called IA-520 hereafter) rises on a time scale of ~ 0.5 ps. A simultaneous blue-shift from ~ 520 nm to ~ 500 nm and broadening (spanning a wavelength range of 420 nm to 560 nm) of the contributing peak could be seen. IA-520 recovers on a time scale of ~ 30 ps. The absorption increase centred at around 340 nm on the other hand peaks on a time scale of around ~ 70 ps after excitation by the pump pulse and seems to persist well beyond the measured time range. The next sub-section focuses on the analysis and interpretation of the transient changes induced in B-82 by Pu-266 in order to identify the physical mechanisms giving rise to the femtosecond signals.

6.1.2 Interpretation of transient data

Dielectric function of BTO:

The optical constants of BTO necessary for modelling of the transient data was determined from its dielectric function obtained from ellipsometry. The contributions to the model dielectric function of BTO include direct band-to-band transitions, transitions related to higher order states and core-level transitions. Band-to-band transitions were taken into account with the help of the model dielectric function at semiconductor critical points developed by Adachi [111]. Higher order transitions were taken into consideration by including Gaussian line shape functions into the model dielectric function. The core-level transitions on the other hand were included

by means of a wavelength-dependent term given by equation (6.1), where A_{pol} and E_{pol} are fit parameters while $E(\lambda)$ is the photon energy. The real and imaginary part of the dielectric function of BTO along with the different contributions is shown in Figure 6.3 (a) and (b) respectively.

$$\varepsilon_{CL}(\lambda) = \frac{A_{pol}}{(E_{pol})^2 - (E(\lambda))^2} \quad (6.1)$$

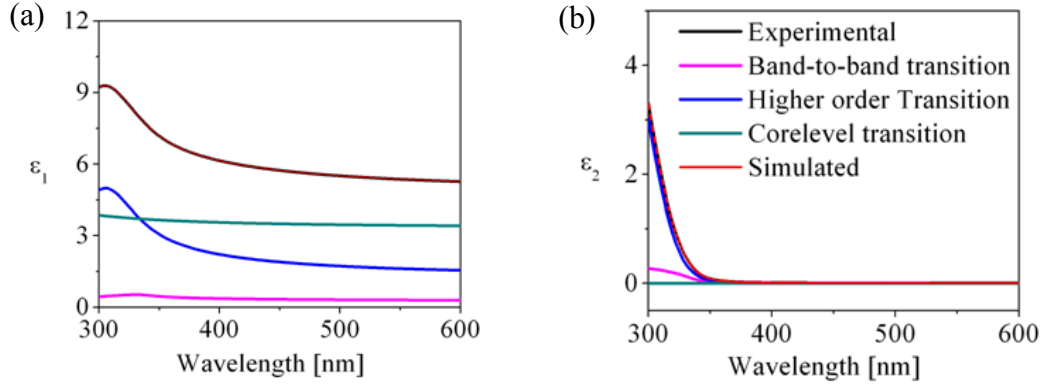


Figure 6.3 Overall and individual contributions to the (a) real and (b) imaginary parts of dielectric function of BTO

Modeling and interpretation of time-resolved spectra:

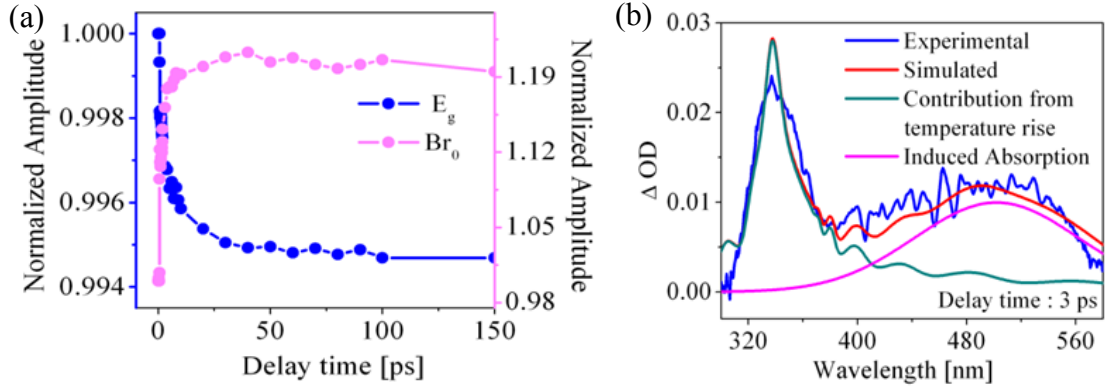


Figure 6.4 (a) Temporal evolution of E_g and Br_0 ; (b) Simulated spectra depicting the different contributions to the transient spectra of BTO

The absorption increase centered at ~ 340 nm could be successfully simulated by a combined variation of the band-gap (E_g) and broadening of band-to-band transitions (Br_0) in the dielectric function of BTO. The contribution results from the decrease in the energy of the forbidden gap and increase in the broadening of band-to-band transitions. It has been discussed in section 5.3.5 that increases in lattice temperature of a semiconductor results in reduction of band-gap energy accompanied by a broadening of electronic transitions. It is also well known that it may take several picoseconds for complete thermalization of the sample. The time evolution of the

transient data reveals a rise time of ~ 70 ps for the contribution. Hence, we may conclude that the absorption increase owes its origin to heating of the sample upon absorption of energy from the pump-pulse. The temporal evolution of E_g and Br_0 plotted in Figure 6.4 (a) shows that maximum broadening of the peak occurs on a time scale of ~ 10 ps; however it takes much longer time for the maximum change in the band-gap energy to take place.

None of the parameters in the dielectric function of BTO could account for the IA-520 component of transient spectra. The spectral position of the contribution indicates that transitions from defect-states lying within the forbidden gap (not included in the model dielectric function) could be a possible origin of the contribution. Therefore, the contribution was taken into account by adding a Gaussian curve into the model. All the three parameters corresponding to the Gaussian curve i.e. peak position, width as well as amplitude were allowed to vary. A simulated spectrum of B-82 at a time delay time of 3 ps after excitation, along with the individual contributing components is shown in Figure 6.4 (b).

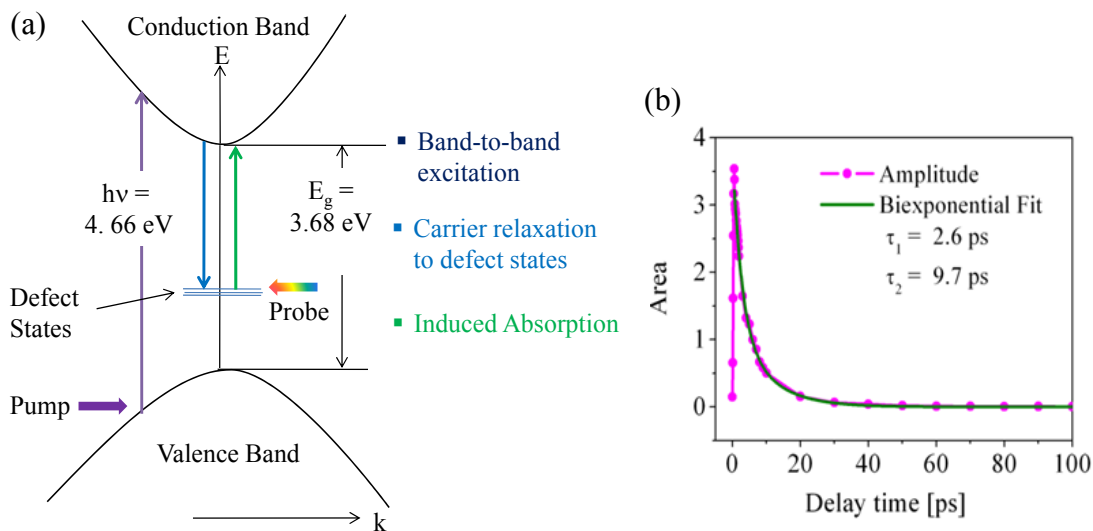


Figure 6.5 (a) Schematic diagram showing the transitions giving rise to IA-520;

(b) Time evolution of IA-520

The increase in absorption at ~ 520 nm can be physically explained on the basis of the model proposed by Ross et al. [112]. A schematic band-diagram demonstrating the proposed scheme is presented in Figure 6.5 (a). Excitation of the sample by Pu-266 directly excites electrons from the valence band into the conduction band. An excited population thus created may recombine directly with the holes in the valence band or into acceptor levels within the band-gap. Recombination at a trap state result in the population of the state by electrons and such electrons can be re-excited by absorption of photons from the weak supercontinuum probe. This will result in an absorption increase in the transient spectra at the corresponding spectral position. The defect levels are assumed to be empty prior to excitation, and are thought to be populated only when relaxation of charge carriers takes place from the conduction band to the defect states. When the sample is excited by Pu-400, such an effect is not observed because the photon energy provided by the 400 nm pump is not sufficient to excite electrons from valence band (or band tail states) into the conduction band.

It has been reported that the conductivity of nominally undoped BTO is dominated by the presence of accidental impurities. Common impurity elements include Mg, Mn, Al and Fe among others [66, 54]. Acceptor levels related to Mn²⁺ ions located at ~ 1.3 eV from the top of the valence band in BTO [54]. Transition of electrons from these states to the bottom of the conduction band can occur by absorption of a photon having energy around 2.38 eV giving rise to the absorption increase at ~ 520 nm. However, it is also evident from the broad nature of the contributing peak that transitions from multiple trapping levels must be involved in the process. This is in consistency with the theory developed for light-induced absorption in BTO which emphasize on the presence of multiple impurity centers in BTO, each of them occurring at different valence states [56, 113, 114]. The trap states are populated by carriers relaxing back to the defect levels from the conduction band. The simultaneous blue shift and gradual broadening of the contribution observed for early times must be due to the relatively faster population of the deep levels (with reference to the valence band) in comparison to the shallow trap states. The temporal behaviour of the amplitude of the contribution is plotted as a function of delay time in Figure 6.5 (b). The induced absorption peaks on a timescale of 0.5 ps after excitation and recovers completely on a time scale of ~ 40 ps. A bi-exponential fit to the decay behaviour yields time constants of 2.6 ps and 9.7 ps respectively. Earlier reports on absorption decay measurements performed on BTO crystals also revealed two-exponential recovery times with time constants of ~ 50 ms and 3-5 ps [115]. However, the reported time constants correspond to the response under CW illumination of the sample. It has been shown that under high intensity illumination from pulsed lasers, the recovery time of induced absorption is considerably reduced [116] which explains the relatively faster recovery of the contribution in our case.

Intensity dependence of the contributions:

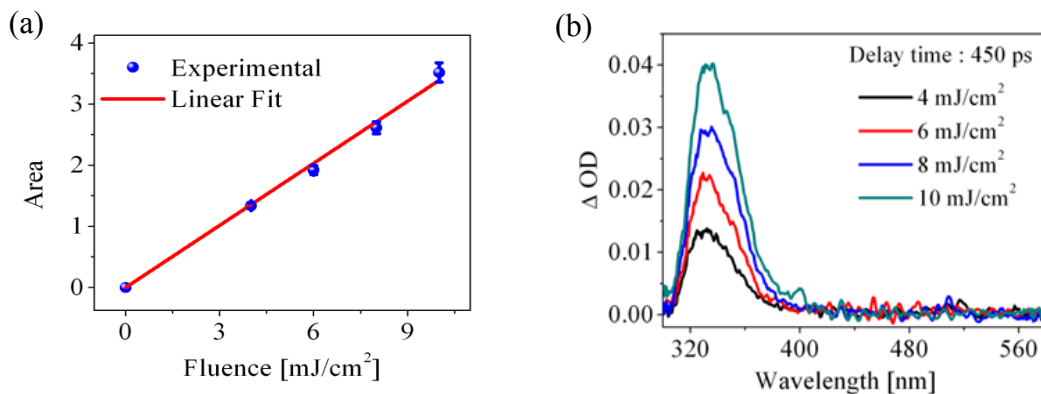


Figure 6.6 (a) Maximum amplitude of IA-520 and (b) Absorption increase at ~ 340 nm at 450 ps, as a function of pump-fluence

In order to probe the intensity dependence of the contributions to the time resolved spectra of BTO, measurements were carried out at four different fluences i.e. 4 mJ/cm², 6 mJ/cm², 8 mJ/cm² and 10 mJ/cm² (pump λ : 266 nm). The maximum amplitude of IA-520 is plotted as function of pump-fluence in Figure 6.6 (a). The linear increase of amplitude with the increasing input photon-flux can be attributed to the increase in effective trap density at higher fluences. Previous reports have also shown that the effective empty trap concentration increase with increasing illumination intensity [56, 117], where a two centre model has been proposed

comprising of primary and secondary trap states. The secondary trap states are assumed to be shallower than the primary centres and highly ionized. At low intensities, only the primary centres contribute to the trapping of carriers while at higher intensities an additional influence from the secondary centres results in an enhancement of the effective trap density. Increase in the incident fluence also results in higher lattice temperatures due to higher amount of absorption. This is reflected in the intensity dependence of the absorption increase at ~ 340 nm shown in Figure 6.6 (b). As an annotation it should be mentioned here that intensity dependent measurements on B-82 with an excitation wavelength of 400 nm yielded similar results as discussed in subsection 6.1.1.

6.2 Time-resolved dynamics of BTO/ZnO thin film samples

A typical double layered heterostructure consists of two participating semiconductors, usually having different band-gap values, which lead to discontinuities in both the conduction band and the valence band. The band-offsets which come forth as a result of this, critically influence the electrical and optical properties of the heterostructure [118, 119]. Therefore, the first step towards understanding the electronic properties of a heterostructure is to gain an insight of the energy-band profile at the interface of the two materials. For an abrupt heterojunction, the energy band-diagram can be determined by the application of Anderson's rule [120], which uses the knowledge of the material parameters like electron affinity, band gap of individual material etc. to determine the band-offset at the heterojunction. A schematic diagram of the energy-profile of the BTO/ZnO heterostructure determined using the Anderson's rule is presented in Figure 6.7.

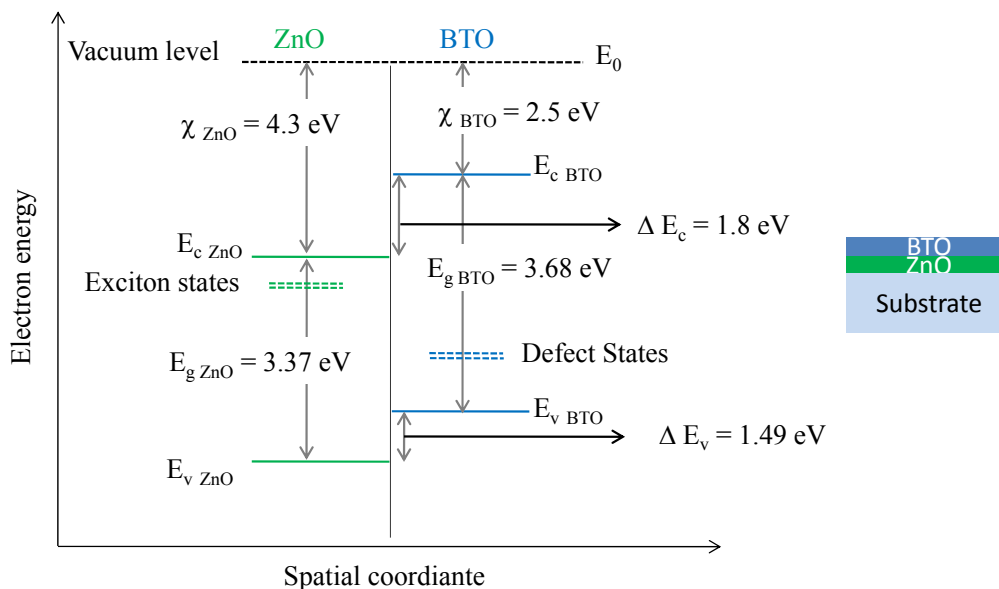


Figure 6.7 Schematic energy-band diagram of BTO/ZnO heterojunction

Using known electron affinity values of 4.3 eV for ZnO [121] and 2.5 eV for BTO [122], a valence band-offset of 1.49 eV and a conduction band-offset of 1.8 eV at the BTO/ZnO heterojunction could be estimated. However, it should be noted that that

the band-alignment at the interface is also influenced by additional factors such as crystal strain, interfacial defects etc. Nevertheless, a qualitative assessment of the dynamics must still be plausible using this simple model.

Pump-probe spectroscopy was performed on the BTO/ZnO thin films samples. The following sub-sections give a qualitative insight of the time-resolved measurements on BZ-370, along with a detailed analysis of the processes induced by ultrafast excitation of ZnO and BTO in the heterostructure configuration and its dependence on input intensity. This is followed by a report on the individual-layer thickness dependence of the ultrafast dynamics, on the basis of the measurements performed on BZ-370, BZ-202 and BZ-91.

6.2.1 Time resolved results from BZ-370

Excitation by Pu-400:

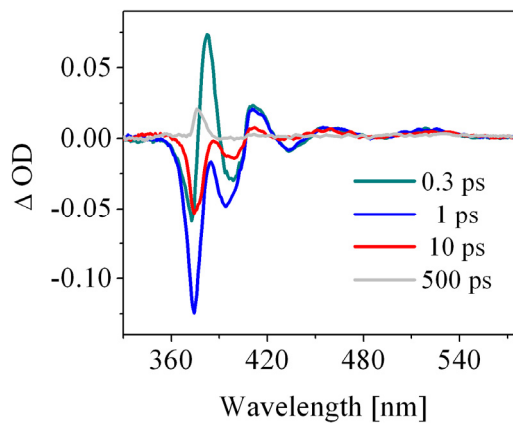


Figure 6.8 ΔOD as function of wavelength over a range of delay times

The transient changes in optical density as a function of wavelength upon excitation of BZ-370 with a pump fluence of 47 mJ/cm² is shown in Figure 6.8. A visual analysis of the spectra reveals that the transient spectra of the double-layered BTO/ZnO sample are principally dominated by spectral contributions from the ZnO layer. Moreover, excitations of the double-layered heterostructure from ZnO side or from the BTO side of the sample show similar experimental results. This naturally can be expected because experiments with B-82 have shown that BTO is transparent to the 400 nm pump pulses. While studying the time resolved results of BZ-370, it is worthwhile and helpful to keep in mind that the ZnO layer in the BZ-370 sample is equivalent in all respects to that in Z-365. The spectral evolution of the contributions from exciton bleaching (transmission increase \sim 375 nm), band-gap renormalization (absorption increase \sim 382 nm) and stimulated emission in ZnO in BZ-370 (transmission increase at \sim 390 nm) is hence comparable to that in Z-365. However, the modulations observed in the range of 400 nm to 600 nm, which arise as a result of change in refractive index, differ in amplitude as well as period as compared to that in Z-365. This again is quite obvious as the spectral behaviour of modulations in the transient spectra is determined by that in the linear transmission spectra which is naturally different for the single-layered ZnO sample and the double-layered BTO/ZnO sample. Another striking difference is the presence of a broad positive

feature existing in conjunction to the modulations for the transient spectra from BZ-370.

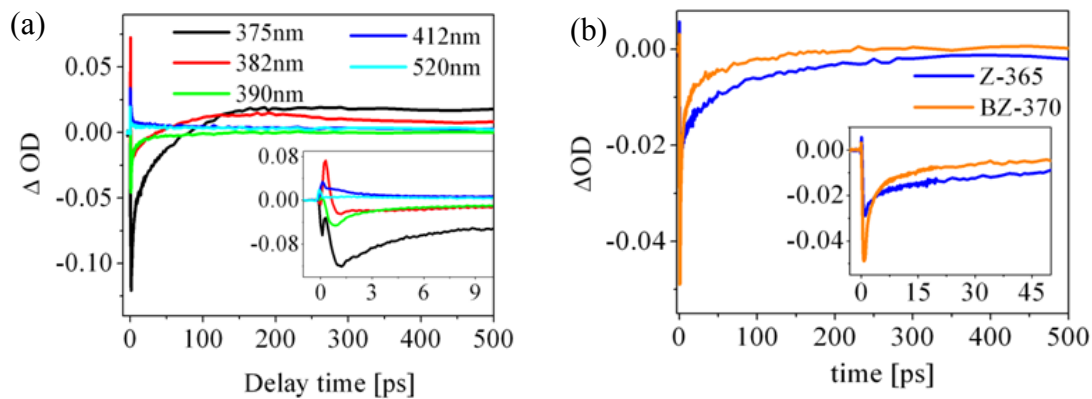


Figure 6.9 ΔOD as function of delay time for (a) selected wavelengths in the transient spectra of BZ-370, (b) $\lambda = 390$ nm for transient spectra in Z-365 and BZ-370

Change in ΔOD as a function of delay time, corresponding to the wavelength positions exhibiting the strongest contributions to transient spectra of BZ-370 is plotted in Figure 6.9 (a). The contribution from band-gap renormalization of ZnO depicted by the red curve in the graph rises on a time scale of 0.3 ps and is observed in the time-sequence upto 0.7 ps. On the other hand, both exciton bleaching and stimulated emission peaks (represented by the black and green curves respectively) becomes maximum on a time scale of ~ 1 ps. Relaxation of the bleaching contribution occurs on a time scale of ~ 100 ps while stimulated emission is seen to contribute till ~ 200 ps. The absorption increase at around 377 nm attributed to heating of the ZnO layer is observed to peak at ~ 70 ps. It is observed that although the spectral variation of the contributions from ZnO layer in the BZ-370 sample is akin to that in Z-365, a significant difference exists in their decay behaviour. As a demonstration to this a comparison of the time evolution of the contribution at $\lambda = 390$ nm in the transient spectra of Z-365 and BZ-370 is shown in Figure 6.9 (b).

Excitation by Pu-266:

Time resolved measurements were performed on BZ-370 with Pu-266 with an excitation fluence of 10 mJ/cm^2 . Both ZnO and BTO interact strongly with the Pu-266, therefore, characteristic contributions from ZnO is observed when the sample is excited from the ZnO side and that from BTO is exhibited when it is perturbed from BTO side of the sample. The individual thickness of both ZnO and BTO layer in BZ-370 (each more than 300 nm) are quite large in comparison to the penetration depths δ_p ($\delta_p = 1/\alpha$) of 60 nm and 28 nm for ZnO and BTO respectively for Pu-266. Owing to this, when the sample is excited from the BTO side, depletion of the pump energy occurs within the BTO layer and the pump does not interact with the ZnO layer. The same holds true for the reverse side too. The transient transmission changes induced in BZ-370 by Pu-266 for incidence from the ZnO side and BTO side is plotted in Figure 6.10 (a) and (b) respectively.

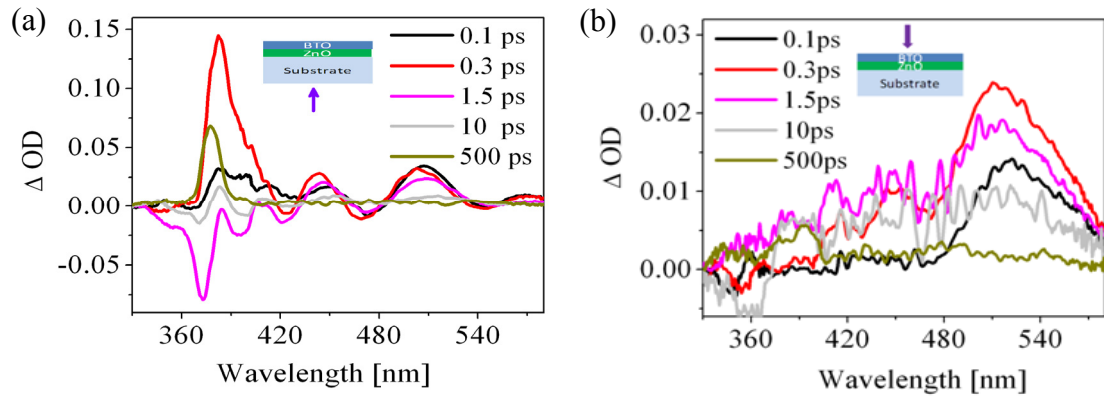


Figure 6.10 Time resolved spectra of BZ-370 for selected delay times for irradiation from (a) ZnO side and (b) BTO side (Excitation $\lambda = 266$ nm)

The spectral variations at very early times (represented by black and red curves in Figure 6.10 (a)) exhibit a strong contribution from band-gap renormalization in ZnO. The absorption increase due to renormalization is asymmetric with the red end extending upto ~ 415 nm for the spectra corresponding to 0.3 ps. Transmission increases due to exciton bleaching and stimulated emission can be identified later in the time sequence (at ~ 1 ps). As in the case of excitation of Z-365, the contribution from exciton bleaching is comparatively delayed with respect to that when excited by Pu-400. The spectral features in the transient spectra of the sample when irradiated from the BTO side include a broad absorption increase in the visible region combined with modulations. The physical origin of the induced absorption in the visible region has been discussed in section 6.1.2. The modulations on the other hand arise due to the change in refractive index as result of the modified charge distribution upon photo-excitation of the photorefractive BTO layer. Surprisingly the absorption increase due to rise in temperature of the BTO layer at ~ 340 nm observed for B-82 is not visible in this case. This must be due to the presence of the thick ZnO layer absorbing the weak probe in the vicinity of the contribution.

6.2.2 Interpretation of transient data via model analysis

This subsection focuses on the interpretation of dynamics via modelling of the transient data obtained by excitation of the sample from the ZnO side. A comparative evaluation of the dynamics of ZnO in the single layered form and the double-layered heterostructure configuration is presented thus revealing the influence of BTO on the charge carrier dynamics in ZnO. The optical constants required for modelling of data were determined from ellipsometry measurements performed on the sample. The ellipsometry data was modelled with the known dielectric model functions of BTO and ZnO [22], which resulted in information on the dielectric function and optical constants of the individual ZnO and BTO layers in the heterostructure configuration.

All contributing components which were observed upon excitation of Z-365 could also be recognized for BZ-370. However, it was found that a discrepancy exists in the visible region of the spectrum with a pronounced peak at around 412 nm (an example shown in Figure 6.11 (a)), which could not be explained by any of the identified processes in ZnO. Two Gaussian curves, one at ~ 412 nm and the other at ~ 520 nm had to be added into the model for compensation of the encountered discrepancy. Both amplitude as well as width of the added Gaussians was allowed to

vary within the fitting routine. A simulated transient spectrum of BZ-370 at a delay of 1 ps along with all the contributing processes is presented in Figure 6.11 (b). The following paragraphs present a detailed discussion and identification of the contributions at 412 nm and 520 nm in the transient spectra.

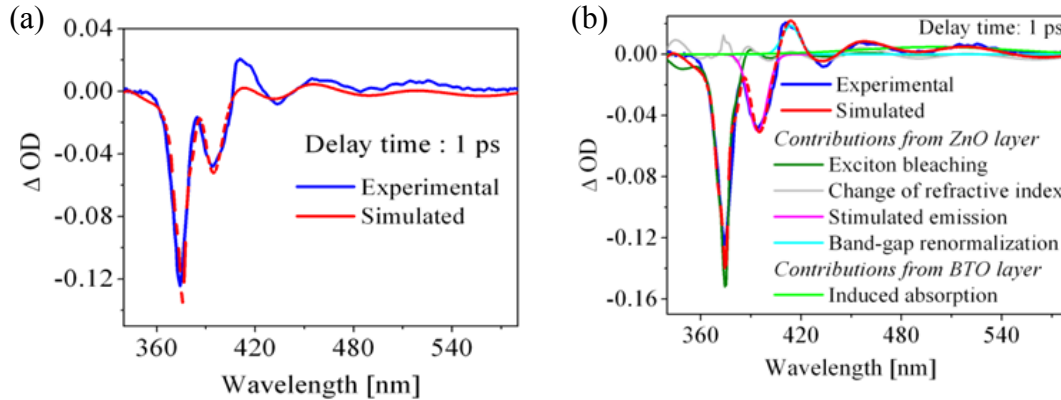


Figure 6.11 (a) Discrepancy between simulated and transient spectra of BZ-370 prior to incorporation of Gaussian curves at 412 nm and 520 nm; (b) Simulated spectra of BZ-370 at 1 ps along with contributions to the spectra, (excitation $\lambda = 400$ nm)

The spectral behaviour of the contribution at 520 nm is comparable to the contribution IA-520 observed in the transient response of B-82. In light of the observation that the BTO layer is non-responsive to Pu-400, it would not be incorrect to surmise that the contribution arises due to population of the defect states by transport of carriers from the ZnO layer to the BTO layer at the interface. It is well known that photo-excited electrons and holes tend to accumulate in different layers in a heterostructure depending on the respective band-alignment at the interface [123]. The resulting charge separation gives rise to interfacial electric field changing the band-alignment and hence leading to interlayer charge transport at the interface. In this light, the induced fields at the interface of ZnO and BTO ought to bend the initial energy profile thus leading to reduction of the conduction band-offset and facilitating electron transport from the conduction band of ZnO to that in BTO. The carriers further relax to the impurity centres in the BTO layer to be re-excited by absorbing photons from the probe and giving rise to an absorption increase in the visible region.

It is visibly clear from the transient spectra excited by Pu-266 that the red end of the absorption increase due to BGR (~ 382 nm) in ZnO extends upto 415 nm. Moreover, analysis of the temporal behaviour of the BGR contribution in Z-365 (discussed in section 5.3.3) revealed that the contribution is overpowered by the stronger bleaching and stimulated emission peaks on a time scale of around 800 fs. Therefore, it is possible that with time the competing and stronger effects from exciton bleaching and stimulated emission mask the blue end of the contribution but not the red end. In that case the red-end of the contribution will still be visible and must be then reflected as a single (or more) peak in the vicinity of 415 nm. In light of the above observations and arguments, it can be said that the absorption increase at 412 nm (called BGR-412 hereafter for convenience) is a residual of the absorption increase due to BGR in ZnO. Since, such behaviour of the BGR effect was not observed in the single layered Z-365 sample, it is obvious that there is a remnant BGR

contribution in case of BZ-370 and is due to the presence and influence of the BTO layer on the charge distribution in the ZnO layer. Remnant renormalization of ZnO band-gap has also been observed by Böntzen et al. by spectroscopic ellipsometry measurements performed on BTO/ZnO heterostructures [22]. The effect was attributed to formation of ferroelectric domains in the BTO layer upon application of an external electric field. Ferroelectric domains are likely to be formed in the BTO layer by the strong electric field component of the high intensity pump-pulses used for our measurements, which in turn can incur a similar effect in the BZ-370 sample.

In order to extract the temporal evolution of the individual contributions, each transient spectrum over the entire measured time sequence was modelled. A comparative analysis of the time behaviour of exciton bleaching in Z-365 and BZ-370 revealed that bleaching of exciton states in ZnO remains unchanged by the additional BTO layer or additional interfacial charge transport. Moreover, similar early time behaviour of the exciton bleaching upon excitation by Pu-266 for both the samples, leads to the conclusion that the mechanism of exciton formation in ZnO (discussed in detail in section 5.4.1) also remains uninfluenced by the presence of the BTO layer. The temporal evolution of stimulated emission from ZnO in BTO/ZnO on the other hand has been found to be considerably altered as compared to that in the ZnO sample as seen in Figure 6.12 (a).

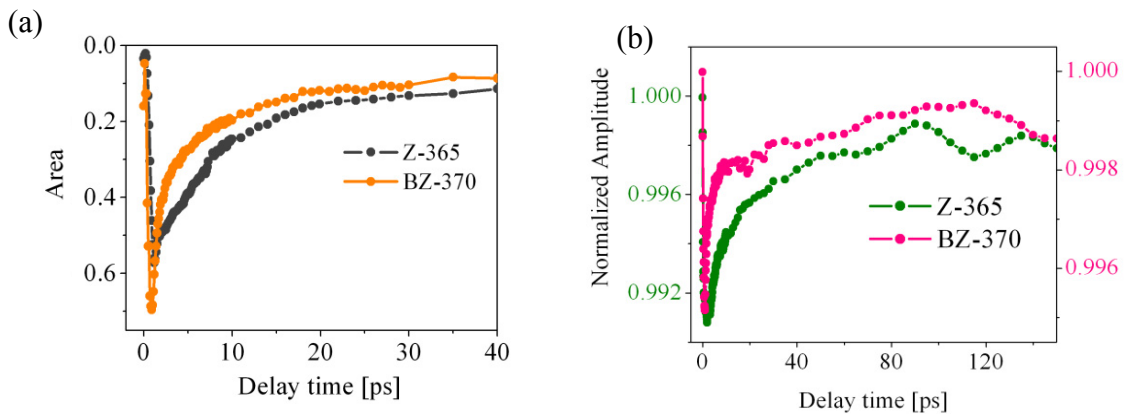


Figure 6.12 Comparison of time behaviour of (a) stimulated emission and (b) refractive index change in Z-365 and BZ-370 samples

A fast relaxation of the contribution occurs on a time scale of around 6 ps which is followed by a slower decay on a time scale of ~ 200 ps. This initial dip in the contribution must be due to the rapid decrease in the number of carriers (excitons or free carriers) by excitonic scattering processes as well as transport of carriers from the ZnO layer to the BTO layer. Furthermore, the relaxation of stimulated was observed to be bi-exponential for Z-365, but a tri-exponential curve was required to fit the relaxation of stimulated emission in BZ-370 yielding time constants of 1.2 ps, 9 ps and 163 ps respectively. Among others the time evolution of the recovery of the refractive index in ZnO is different for Z-365 and BZ-370 (Figure 6.12 (b)). This must be due to the relatively changed distribution of carriers in the ZnO layer due to the presence of the BTO layer.

The time behaviour of BGR-412 and the induced absorption from BTO layer is plotted as a function of delay times in Figure 6.13 (a) and (b) respectively. The rise time of ~ 300 fs for BGR-412 is consistent to that at 382 nm and the recovery of the

contribution takes place on a time scale of around 10 ps. The induced absorption from the BTO layer on the other hand builds up on a time scale of around ~ 2 ps accompanied by a slow and gradual recovery on a time scale of ~ 400 ps. In addition to that, a minor residual of the contribution is also seen to remain beyond the measured time range.

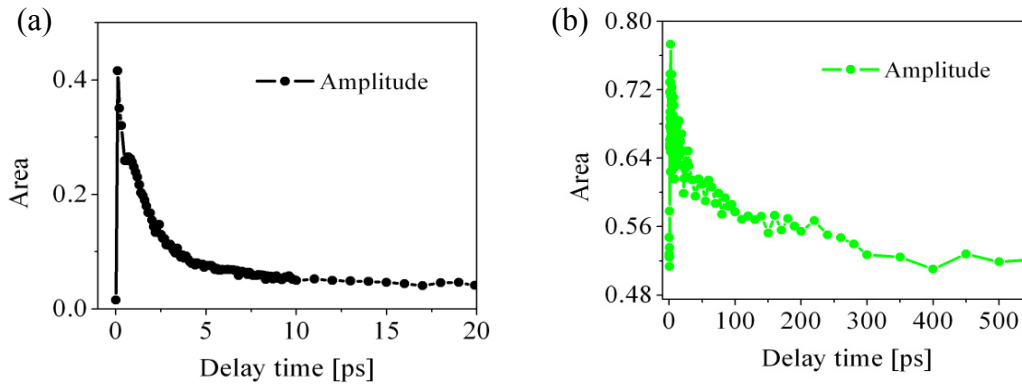


Figure 6.13 Time evolution of (a) BGR-412 and (b) induced absorption from the BTO layer in BZ-370

In short it is clear that the temporal behaviour of contributions (from ZnO) to the transient spectra of Z-365 and BZ-370 are not the identical. This must be due to the fact that the ultrafast dynamics for the double-layered sample is determined by the interplay between relaxation of carriers and their transport across the interface, while for the single-layered ZnO sample only the relaxation of charge carriers is important. A clear demarcation between the time scales of occurrence of the relaxation and transport processes in BZ-370 is perhaps not possible by femtosecond time-resolved experiments in the transmission mode [123] or requires a rather more rigorous theoretical modeling of the time-resolved data. The next sub-section presents a succinct account of the influence of input intensity and thickness of the ZnO and BTO layer on the contributions to the transient response of BTO/ZnO samples.

6.2.3 Intensity and thickness dependence of contributions to transient spectra

Time-resolved pump probe experiments were performed on BZ-370 with Pu-400 and five different fluences of 16 mJ/cm², 32 mJ/cm², 48 mJ/cm², 64 mJ/cm² and 79 mJ/cm² in order to study the intensity dependence of the contributing components. The transient change in optical density from the samples was observed to be strongly influenced by the input photon flux. As a demonstration, the transient transmission spectra of BZ-370 corresponding to different pump-energies are plotted in Figure 6.14 (a) for a time delay of 0.3 ps. Both exciton bleaching and stimulated emission increases non-linearly with the increasing pump-pump fluence which is similar to their behavior in Z-365. In order to learn about the intensity dependence of their time behavior, the estimated decay constants for exciton bleaching and stimulated emission are tabulated in Table 6.1 and 6.2 respectively.

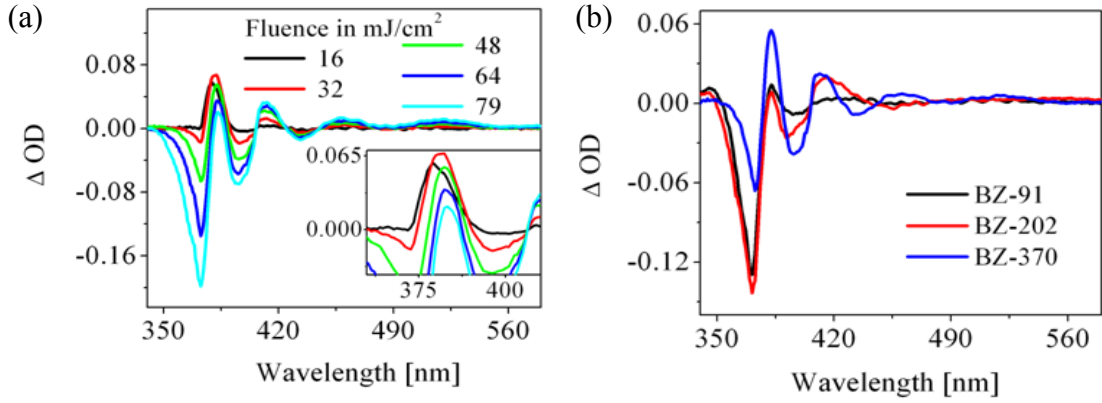


Figure 6.14 Time-resolved spectra (a) of BZ-370 corresponding to different excitation fluences and (b) of different BTO/ZnO films at a fluence of 48 mJ/cm² (delay time = 0.3 ps delay; Excitation $\lambda = 400$ nm)

Pump fluence (in mJ/cm ²)	Decay Constants	
	τ_1 (ps)	τ_2 (ps)
48	2.2	30
64	2.4	27.9
79	2.5	26.6

Table 6.1 Decay-constants (relative error $\sim 8\%$) for exciton bleaching in BZ-370 corresponding to different excitation energies

Pump fluence (in mJ/cm ²)	Decay Constants		
	τ_1 (ps)	τ_2 (ps)	τ_3 (ps)
48	1.2	9	163.1
64	1.1	10.9	140.7
79	1.1	11	112.1

Table 6.2 Decay-constants (relative error $\sim 8\%$) for stimulated emission in BZ-370 corresponding to different excitation energies

The smaller of the decay constants related to exciton bleaching (depicting the trapping of charge carriers in the ZnO layer) remain unaffected by the changing pump-fluence. But the larger of the constants (depicting the radiative recombination of excitons) decrease with the increasing intensity. This is in contrast to the trend observed in Z-365 where both the time constants remain unchanged by the variation of input intensity. The smallest of the three decay constants for stimulated emission remains unaltered by the changing pump-fluence. The other two time constants show a similar evolution as a function of pump fluence as seen for the single-layered ZnO sample. The temporal behaviour of the BGR contribution at ~ 382 nm shows no appreciable change in the double-layered configuration (inset of Figure 6.14 (a)).

However, the residual contribution from BGR at ~ 412 nm increases with increasing input photon flux which is in consistent with the general trend of the renormalization effect due to many body-effects in semiconductors. The amplitude of the induced absorption from BTO layer is also observed to be incremented with the increasing pump-fluence.

Measurements were also done on BZ-91, BZ-202 and BZ-370 with aim of probing the effect of ZnO layer thickness on the time-resolved response of BTO/ZnO samples. For these measurements the pump-fluence was kept fixed at 48 mJ/cm^2 (excitation λ : 400 nm). The transient transmission signals at a delay of 0.3 ps for the three samples are shown in Figure 6.14 (b). The spectral as well as temporal evolution of each of contributing components as a function of thickness is similar to that observed in pure ZnO samples (Z-365, Z-186 and Z-100), a detailed study of which has been presented in section 5.6. Therein it could be perceived that the crystalline properties of the samples, which change with the changing layer thickness, critically influence the optical properties of the sample. In this light we may conclude that the ZnO layer retains its crystalline properties in the heterostructure configuration.

6.3 Summary

We have found that excitation by Pu-400 could not induce any transient transmission changes in B-82. In contrast to that, the above band-gap excitation of the sample by Pu-266 revealed a broad induced absorption in the visible region attributed to transitions from multiple defect states, and an absorption increase at ~ 340 nm ascribed to thermal effects. The thermal effects maximize on a time scale of ~ 70 ps and seem to persist well beyond the measured time range. But the defect related absorption increase peaks on a time scale of ~ 0.5 ps and recovers bi-exponentially on a time scale of ~ 30 ps. The relatively faster decay of the contribution in comparison to that reported in literature is thought to be due to high intensity excitation of the sample by femtosecond pulses. The induced absorption increases linearly with increasing pump-fluence due to an enhancement in the effective trap density at higher intensities.

The contributing components from ZnO layer were found to be the prominent features in the transient transmission spectra of BTO/ZnO samples. A small contribution from induced absorption in BTO layer could be traced in the spectra, and is accredited to transport of charge carriers from the ZnO layer to the BTO layer at the interface. Additionally a remnant contribution from band-gap renormalization in ZnO, due to formation of ferroelectric domains in BTO, could be identified. Recovery of the process takes place on a time scale of ~ 10 ps. The induced absorption from BTO rises on a time scale of ~ 2 ps and is seen to exist till ~ 400 ps in the time sequence. A comparative analysis of the temporal behaviour of the contributions from ZnO in Z-365 and BZ-370 confirmed that the dynamical behaviour of the ultrafast processes in ZnO is significantly altered when it shares an interface with BTO. This is an influence from the additional processes which occur at the interface due to the presence of the BTO layer. The conclusion was further reaffirmed by the findings from intensity dependent measurements on BTO/ZnO. The evolution of each of contributions as a function of the ZnO layer thickness in the double-layered sample elucidates the fact that ZnO retains its crystalline properties in the heterostructure configuration.

Chapter 7 Summary

The ultrafast dynamics induced by below band-gap off-resonant excitation of ZnO, BTO and BTO/ZnO thin films was intensively studied using femtosecond pump-probe spectroscopy. The transient data obtained were analysed and interpreted using a dielectric function based semi-empirical model together with information extracted from similar experiments with above band-gap excitation of the samples by 266 nm ultrashort pulses. All samples were fully characterized for their pertinent properties prior to performing time-resolved measurements on them. The ultrafast excitation of ZnO by 400 nm laser pulses resulted in strong spectral changes in the vicinity of the exciton resonances and spectral modulations in the visible region of the spectrum. In contrast to that the single layered BTO film remained unresponsive to the 400 nm femtosecond pulses. The spectra of the double-layered films were found to be dominated by the spectral contributions from the ZnO layer with minor additional contributions attributed to BTO.

The excitation of ZnO by high intensity 400 nm pulses support transition of a large number of carriers from the band tail states (and from the valence band) to the exciton states (to states higher into the conduction band) by multiphoton absorption. This triggers a mutually inclusive train of events which includes bleaching due to population of the exciton-A states, stimulated emission due to excitonic scattering processes and change in the refractive index resulting from core-level excitonic transitions and higher order transitions. Processes related to many body interactions in a semiconductor like renormalization of the band-gap were also quite prominent. A simple approximation to the relaxation behaviour of the processes was made by fitting their temporal evolution with exponential decay curves wherever applicable. The decay dynamics of exciton bleaching was found to be bi-exponential with time constants of ~ 2 ps and ~ 20 ps respectively. The smaller constant is attributed to trapping of charge carriers by defect states while the larger one is related to exciton annihilation by scattering processes. The contribution from stimulated emission also decays bi-exponentially with respective time constants of ~ 8 ps and ~ 70 ps. The smaller of the decay constants is related to excitonic scattering processes, while the larger time constant is associated with the slow and gradual recombination of electrons (trapped into shallow trap states) with the deeply trapped holes within the band-gap. Exciton recombination takes place on a time scale of ~ 100 ps and complete decay of stimulated emission occurs on a time scale of ~ 200 ps. However, due to the strong influence from other processes the exact time scale of recovery of the renormalized band-gap could not be ascertained. The later time dynamics is dominated by thermal effects induced in the sample as a result of absorption of the strong pump. Complete thermalization of the lattice with the surroundings occurs much later than the measured time range of 600 ps.

That each of the contributing processes is critically influenced by the excitation fluence was confirmed by intensity dependent experiments on the ZnO samples. It was found that increase in the input photon flux results in a faster build up of the excited population because of enhanced generation rates. Bleaching of exciton states and stimulated emission increase non-linearly with increasing input intensity. Furthermore, saturation like behaviour is observed for stimulated emission at higher excitation fluences which is in agreement with the theory of gain saturation at elevated intensities. An increase in amplitude of the spectral modulations with the rising input intensity was apparent too. In contrast, the amplitude of the absorption increase resulting from renormalization of ZnO band-gap showed an astonishing behaviour with increasing input photon flux. The amplitude of the contribution was enhanced with increasing photon flux but to be diminished again with further increase in intensity. This behaviour is attributed to the overpowering of the contribution by the significantly enhanced transmission increase peaks from exciton bleaching and stimulated emission at higher intensities. The decay constants related to exciton bleaching remained unchanged with the varying intensity. Conversely, the stimulated emission arising from recombination of trapped carriers decays faster with increasing input intensity which is consistent with the time behaviour observed by other researchers. The slower decay of emission due to excitonic scattering processes for higher intensities is speculated to be due to saturation of one or more decay channel at higher fluences.

The layer thickness dependence of the ZnO films revealed that the crystalline properties of the thin film samples are crucial to the determination of its ultrafast behaviour. Bleaching of the exciton states was significantly enhanced for the films having smaller crystallite size due to the increased exciton oscillator strength resulting from enlarged confinement effects. A comparatively higher stimulated emission observed in case of thicker films is thought to be due to a combined effect of improved crystalline quality in thicker films and increase in the number of emitters with the increasing sample layer. The contribution from band-gap renormalization was found to become less prominent for thinner films. This has been attributed to the higher frequency of carrier-surface interactions for thinner films, resulting in a reduced excited carrier density due to the increased probability of carrier trapping. The change in refractive index remains unchanged even though the spectral characteristics of the resulting modulations are significantly different in films of varying thickness. The decay behaviour of contribution from exciton bleaching was unable to reveal much about influence of thickness on the rate of exciton recombination. However, from the temporal behaviour of stimulated emission in the different ZnO films it could be concluded that the rate of charge-carrier recombination decreases with the decreasing thickness (and/or crystallite size) of the films.

Since no significant spectral response could be observed upon excitation of single layered BTO film with 400 nm femtosecond pulses, measurements were performed with an excitation wavelength of 266 nm in order to have an overview of the possible transitions initiated by femtosecond pulsed excitation in BTO. The femtosecond response of BTO has a significant contribution from pump-induced transition of carriers from mid-gap defect states to the conduction band. This results in a broad absorption increase in the visible region of the spectrum. The contribution which is linearly dependent on input intensity recovers on a time scale of ~ 30 ps. In addition

to that, thermal effects due to absorption of the pump-energy are noticed in the later part of the time sequence.

Even though BTO is transparent to the 400 nm femtosecond pulses, a contribution from induced absorption in the BTO layer could be distinguished in the transient response of the double-layered BTO/ZnO samples. This is accredited to population of defect states in BTO by transport of carriers from ZnO layer over the interface. It could also be perceived that formation of ferroelectric domains in BTO, due to the presence of strong electric field of laser pulses, lead to remnant effects like a long time existence of the contribution from band-gap renormalization in ZnO. Such a temporal behaviour was not observed in the single layered ZnO sample. The investigation also witnessed the changed dynamical behaviour of the ultrafast physical processes related to ZnO in the single layered ZnO films and that in the heterostructure configuration. This includes the temporal evolution of stimulated emission which exhibits a tri-exponential decay in BTO/ZnO, and the changed time behaviour for the recovery of change in refractive index. The altered behaviour is an obvious consequence to the interplay between relaxation of carriers and their transport across the interface. However a clear demarcation between the time scales of occurrence of each of these processes is out of scope of femtosecond time-resolved experiments in the transmission mode. Both exciton bleaching and stimulated emission retain their non-linear behaviour in the heterostructure configuration. As a natural consequence to the additional processes taking place at the interface, the time constants related to bleaching and stimulated emission reveal a different evolutionary behaviour as a function of the input photon flux. Furthermore, an intensive study of the transient response from BTO/ZnO samples differing in the crystallite size as well as thickness of the ZnO layer confirmed that ZnO retains its crystalline properties in the heterostructure configuration.

In conclusion, we could successfully obtain a comprehensive and self-consistent picture of the ultrafast dynamics induced by below band-gap off-resonant excitation in ZnO. The results of this investigation are expected to be resourceful to the field of ZnO research. This coupled with a detailed understanding of the above band-gap dynamics of BTO, provided the means to comprehend and report, for the first time to the best of our knowledge, preliminary findings about the dynamical processes induced in BTO/ZnO heterostructures by femtosecond pulses. The revelations from the study indicate the need for a rigorous theoretical treatment of the topic for achieving a clearer picture of the electronic properties of the composite system.

References

- [1] Klingshirn C 2007 ZnO: Material, Physics and Applications *ChemPhysChem* **8** 782-803
- [2] Bagnall D M, Chen Y F, Zhu Z, Yao T, Koyama S, Shen M Y and Goto T 1997 Optically pumped lasing of ZnO at room temperature *Applied Physics Letters* **70** 2230-2
- [3] Chen Y, Tuan N T, Segawa Y, Ko H-J, Hong S-k and Yao T 2001 Stimulated emission and optical gain in ZnO epilayers grown by plasma-assisted molecular-beam epitaxy with buffers *Applied Physics Letters* **78** 1469-71
- [4] Zu P, Tang Z K, Wong G K L, Kawasaki M, Ohtomo A, Koinuma H and Segawa Y 1997 Ultraviolet spontaneous and stimulated emissions from ZnO microcrystallite thin films at room temperature *Solid State Communications* **103** 459-63
- [5] Brandt M, Frenzel H, Hochmuth H, Lorenz M, Grundmann M and Schubert J 2009 Ferroelectric thin film field-effect transistors based on ZnO/BaTiO₃ heterostructures. AVS) pp 1789-93
- [6] Ashkenov N, Schubert M, Twerdowski E, Wenckstern H v, Mbenkum B N, Hochmuth H, Lorenz M, Grill W and Grundmann M 2005 Rectifying semiconductor-ferroelectric polarization loops and offsets in Pt-BaTiO₃-ZnO-Pt thin film capacitor structures *Thin Solid Films* **486** 153-7
- [7] Voora V M, Hofmann T, Brandt M, Lorenz M, Grundmann M and Schubert M 2008 Electrooptic ellipsometry study of piezoelectric BaTiO₃-ZnO heterostructures *physica status solidi (c)* **5** 1328-31
- [8] Bauer C, Boschloo G, Mukhtar E and Hagfeldt A 2004 Ultrafast relaxation dynamics of charge carriers relaxation in ZnO nanocrystalline thin films *Chemical Physics Letters* **387** 176-81
- [9] Yamamoto A, Kido T, Goto T, Chen Y and Yao T 2002 Bandgap renormalization of ZnO epitaxial thin films *Solid State Communications* **122** 29-32
- [10] Ichida H, Wakaiki S, Mizoguchi K, Kim D, Kanematsu Y and Nakayama M 2008 Fast photoluminescence dynamics in ZnO thin films under high-density excitation conditions *Journal of Luminescence* **128** 1059-61
- [11] Teke A, Özgür Ü, Doğan S, Gu X, Morkoç H, Nemeth B, Nause J and Everitt H O 2004 Excitonic fine structure and recombination dynamics in single-crystalline ZnO *Physical Review B* **70** 195207

- [12] Klingshirn C F, Meyer B K, Waag A, Hoffmann A and Geurts J 2010 *Zinc Oxide: From Fundamental Properties Towards Novel Applications*: Springer)
- [13] Yamamoto A, Kido T, Goto T, Chen Y, Yao T and Kasuya A 1999 Dynamics of photoexcited carriers in ZnO epitaxial thin films *Applied Physics Letters* **75** 469-71
- [14] Song J K, Willer U, Szarko J M, Leone S R, Li S and Zhao Y 2008 Ultrafast Upconversion Probing of Lasing Dynamics in Single ZnO Nanowire Lasers *The Journal of Physical Chemistry C* **112** 1679-84
- [15] Takeda J, Takagi K, Okabe T, Ko H J and Yao T 2004 Relaxation and diffusion of photoexcited carriers in ZnO epitaxial thin films *physica status solidi (c)* **1** 678-81
- [16] Takeda J, Arai N, Toshine Y, Ko H-J and Yao T 2006 Ultrafast Dynamics of Exciton-Exciton and Exciton-Longitudinal Optical-Phonon Scattering Processes in ZnO Epitaxial Thin Films *Japanese Journal of Applied Physics* **45** 6961-3
- [17] Arai N, Takeda J, Ko H-J and Yao T 2006 Dynamics of high-density excitons and electron-hole plasma in ZnO epitaxial thin films *Journal of Luminescence* **119-120** 346-9
- [18] Wang H-C, Yang C C, Feng S-W, Zhang B-P and Segawa Y 2009 Ultrafast Exciton Dynamics in a ZnO Thin Film *Japanese Journal of Applied Physics* **48** 022402
- [19] Voora V M, Hofmann T, Brandt M, Lorenz M, Grundmann M, Ashkenov N, Schmidt H, Ianno N and Schubert M 2010 Interface polarization coupling in piezoelectric-semiconductor ferroelectric heterostructures *Physical Review B* **81** 195307
- [20] Mbenkum B N, Ashkenov N, Schubert M, Lorenz M, Hochmuth H, Michel D, Grundmann M and Wagner G 2005 Temperature-dependent dielectric and electro-optic properties of a ZnO-BaTiO₃-ZnO heterostructure grown by pulsed-laser deposition *Applied Physics Letters* **86** 091904-3
- [21] Schubert M, Ashkenov N, Hofmann T, Lorenz M, Hochmuth H, v. Wenckstern H, Grundmann M and Wagner G 2004 Electro-optical properties of ZnO-BaTiO₃-ZnO heterostructures grown by pulsed laser deposition *Annalen der Physik* **13** 61-2
- [22] Böntgen T, Schöche S, Schmidt-Grund R, Sturm C, Brandt M, Hochmuth H, Lorenz M and Grundmann M 2011 Optical properties of BaTiO₃/ZnO heterostructures under the effect of an applied bias *Thin Solid Films* **519** 2933-5
- [23] Chouthe S 2010 Ultrafast dynamics of ZnO films using femtosecond pump probe spectroscopy. In: *Naturwissenschaftliche Fakultät II*, (Halle(Saale): Martin Luther University) p 105
- [24] Klingshirn C F 2006 *Semiconductor Optics*: Springer)
- [25] Klingshirn C 2005 *Semiconductor optics*: Springer Berlin Heidelberg) pp 521-52
- [26] Orton J W 2004 *The Story Of Semiconductors*: Oxford University Press)

- [27] Rabe K M, Ahn C H and Triscone J M 2007 *Physics of Ferroelectrics: A Modern Perspective*: Springer)
- [28] Singh J 2006 *Optical Properties of Condensed Matter And Applications*: John Wiley)
- [29] Grundmann M 2010 *The physics of semiconductors: An introduction including devices and nanophysics*: Springer)
- [30] Hecht E and Ganesan A R 2001 *Optics*: Pearson Education)
- [31] Fujiwara H 2007 *Spectroscopic Ellipsometry: Principles and Applications*: John Wiley & Sons)
- [32] Yoshikawa H and Adachi S 1997 Optical Constants of ZnO *Japanese Journal of Applied Physics* **36** 6237- 43
- [33] Kim C C, Garland J W, Abad H and Raccah P M 1992 Modeling the optical dielectric function of semiconductors: Extension of the critical-point parabolic-band approximation *Physical Review B* **45** 11749-67
- [34] Sundaram S K and Mazur E 2002 Inducing and probing non-thermal transitions in semiconductors using femtosecond laser pulses *Nat Mater* **1** 217-24
- [35] Kovalev D, Averboukh B, Volm D, Meyer B K, Amano H and Akasaki I 1996 Free exciton emission in GaN *Physical Review B* **54** 2518-22
- [36] Demtröder W 2005 *Atoms, Molecules and Photons: An Introduction to Atomic-, Molecular- And Quantum Physics*: Springer)
- [37] Chander H and Chawla S 2008 Time resolved spectroscopic studies on some nanophosphors *Bulletin of Materials Science* **31** 401-7
- [38] Jonscher A K and Polignac A D 1984 The time dependence of luminescence in solids *Journal of Physics C: Solid State Physics* **17** 6493-519
- [39] Rothenberger G, Moser J, Graetzel M, Serpone N and Sharma D K 1985 Charge carrier trapping and recombination dynamics in small semiconductor particles *Journal of the American Chemical Society* **107** 8054-9
- [40] Rossi F and Kuhn T 2002 Theory of ultrafast phenomena in photoexcited semiconductors *Reviews of Modern Physics* **74** 895-950
- [41] Diels J C and Rudolph W 2006 *Ultrashort Laser Pulse Phenomena*: Elsevier Science)
- [42] Paschotta R 2007 Laser Sources for Ultrashort Pulses – Oscillators and Amplifiers for Various Applications *Laser Technik Journal* **4** 49-51
- [43] Siegman A E 1986 *Lasers*: University Science Books)
- [44] Akkermans E and Montambaux G 2007 *Mesoscopic Physics of Electrons and Photons*: Cambridge University Press)
- [45] Zimmermann R 1988 Nonlinear Optics and the Mott Transition in Semiconductors *physica status solidi (b)* **146** 371-84
- [46] Zhang X Q, Tang Z K, Kawasaki M, Ohtomo A and Koinuma H 2003 Optical gain in self-assembled ZnO microcrysallite thin films *Journal of Crystal Growth* **259** 286-90

- [47] Bohnert K, Schmieder G and Klingshirn C 1980 Gain and Reflection Spectroscopy and the Present Understanding of the Electron–Hole Plasma in II–VI Compounds *physica status solidi (b)* **98** 175-88
- [48] Landsberg P T 1966 Electron Interaction Effects on Recombination Spectra *physica status solidi (b)* **15** 623-6
- [49] Morgan D V, Williams R H and Institution of Electrical E 1991 *Physics and Technology of Heterojunction Devices*: P. Peregrinus Limited)
- [50] Özgür Ü, Alivov Y I, Liu C, Teke A, Reshchikov M A, Doğan S, Avrutin V, Cho S J and Morkoç H 2005 A comprehensive review of ZnO materials and devices *Journal of Applied Physics* **98** 041301-103
- [51] Sanna S, Thierfelder C, Wippermann S, Sinha T P and Schmidt W G Barium titanate ground- and excited-state properties from first-principles calculations *Physical Review B* **83** 054112
- [52] Salehi H, Hosseini S. M and N S 2004 First-Principles Study of the Electronic Structure of BaTiO₃ using Different Approximations *CHINESE JOURNAL OF PHYSICS* **42** 619-27
- [53] Aygun S M and North Carolina State U 2009 *Processing Science of Barium Titanate*: North Carolina State University)
- [54] Lewis G V and Catlow C R A 1986 Defect studies of doped and undoped barium titanate using computer simulation techniques *Journal of Physics and Chemistry of Solids* **47** 89-97
- [55] Buse K and Krätzig E 1992 Light-induced absorption in BaTiO₃ and KNbO₃ generated with high intensity laser pulses *Optical Materials* **1** 165-70
- [56] Brost G A, Motes R A and Rotge J R 1988 Intensity-dependent absorption and photorefractive effects in barium titanate *J. Opt. Soc. Am. B* **5** 1879-85
- [57] Jagadish C and Pearton S J 2006 *Zinc Oxide Bulk, Thin Films And Nanostructures: Processing, Properties And Applications*: Elsevier)
- [58] Laskowski R and Christensen N E 2006 Ab initio calculation of excitons in ZnO *Physical Review B* **73** 045201
- [59] Zhang D H, Xue Z Y and Wang Q P 2002 The mechanisms of blue emission from ZnO films deposited on glass substrate by r.f. magnetron sputtering *Journal of Physics D: Applied Physics* **35** 2837
- [60] Van de Walle C G 2001 Defect analysis and engineering in ZnO *Physica B: Condensed Matter* **308-310** 899-903
- [61] Kobayashi A, Sankey O F and Dow J D 1983 Deep energy levels of defects in the wurtzite semiconductors AlN, CdS, CdSe, ZnS, and ZnO *Physical Review B* **28** 946-56
- [62] Thonke K, Gruber T, Teofilov N, Schönfelder R, Waag A and Sauer R 2001 Donor-acceptor pair transitions in ZnO substrate material *Physica B: Condensed Matter* **308-310** 945-8
- [63] Reshchikov M A, Morkoç H, Nemeth B, Nause J, Xie J, Hertog B and Osinsky A 2007 Luminescence properties of defects in ZnO *Physica B: Condensed Matter* **401-402** 358-61

- [64] Salehi H, Shahtahmasebi N and Hosseini S M 2003 Band structure of tetragonal BaTiO₃ *Eur. Phys. J. B* **32** 177-80
- [65] Golego N, Studenikin S A and Cocivera M 1998 Properties of Dielectric BaTiO₃ Thin Films Prepared by Spray Pyrolysis *Chemistry of Materials* **10** 2000-5
- [66] Banyal R K and Prasad B R 2003 Light-induced absorption in photorefractive BaTiO₃ crystals *Journal of Applied Physics* **93** 9466-9
- [67] Venkata Voora, Tino Hofmann, Ann Kjerstad, Matthias Brandt, Michael Lorenz, Grundmann M and Schubert M 2008 Interface-charge-coupled polarization response model of Pt-BaTiO₃-ZnO-Pt heterojunctions: Physical parameters variation. *MRS Proceedings* **1074**
- [68] J. Ylänen and P.Vuoristo 2006 Use of Pulsed Laser Deposition in the Production of Thin Films – a Literature Review. In: *Tampere University of Technology: Institute of Materials Science*,
- [69] Lorenz M, Wagner G, Rahm A, Schmidt H, Hochmuth H, Schmid H, Mader W, Brandt M, von Wenckstern H and Grundmann M 2008 Homoepitaxial ZnO thin films by PLD: Structural properties *physica status solidi (c)* **5** 3280-7
- [70] Ilican S, Caglar Y and Caglar M 2008 Preparation and characterization of ZnO thin films deposited by sol-gel spin coating method *JOURNAL OF OPTOELECTRONICS AND ADVANCED MATERIALS* **10** 2578-83
- [71] Muth J F, Kolbas R M, Sharma A K, Oktyabrsky S and Narayan J 1999 Excitonic structure and absorption coefficient measurements of ZnO single crystal epitaxial films deposited by pulsed laser deposition *Journal of Applied Physics* **85** 7884-7
- [72] Podlipensky A V 2005 Laser assisted modification of optical and structural properties of composite glass with silver nanoparticles. In: *Fachbereichs Physik: Martin-Luther-Universität Halle-Wittenberg*) p 102
- [73] Stalmashonak A 2009 Laser-induced shape transformation of silver nanoparticles embedded in glass. In: *Naturwissenschaftlichen Fakultät II: Martin-Luther-Universität Halle-Wittenberg*) p 111
- [74] Warth A 2011 In-Situ-Pump-Probe-Weißlichtspektroskopie der laserinduzierten Formänderung von Silbernanopartikeln in Glas. In: *Naturwissenschaftlichen Fakultät II, (Halle(Saale): Martin-Luther-Universität Halle-Wittenberg*) p 95
- [75] Kovalenko S A, Dobryakov A L, Ruthmann J and Ernsting N P 1999 Femtosecond spectroscopy of condensed phases with chirped supercontinuum probing *Physical Review A* **59** 2369-84
- [76] Museur L, Michel J-P, Portes P, Englezis A, Stassinopoulos A, Anglos D and Kanaev A V 2010 Femtosecond UV laser non-ablative surface structuring of ZnO crystal: impact on exciton photoluminescence *J. Opt. Soc. Am. B* **27** 531-5
- [77] Ku S, Haas S, Schoepe G, Pieters B, E., Ye Q and Rau U 2010 Direct ablation of ZnO with UV and IR laser for thin film solar modules *Journal of optoelectronics and advanced materials* **12** 616-20

- [78] Poprawe R 2011 *Tailored Light 2: Laser Application Technology*: Springer)
- [79] Rasmusson M, Tarnovsky A N, Åkesson E and Sundström V 2001 On the use of two-photon absorption for determination of femtosecond pump-probe cross-correlation functions *Chemical Physics Letters* **335** 201-8
- [80] Dietzek B, Pascher T, Sundström V and Yartsev A 2007 Appearance of coherent artifact signals in femtosecond transient absorption spectroscopy in dependence on detector design *Laser Physics Letters* **4** 38-43
- [81] Vardeny Z and Tauc J 1981 Picosecond coherence coupling in the pump and probe technique *Optics Communications* **39** 396-400
- [82] Powell M J D and Yuan Y 1991 A trust region algorithm for equality constrained optimization *Mathematical Programming* **49** 189-211
- [83] Berghen F V 2003-2004 CONDOR: a constrained, non-linear, derivative-free parallel optimizer for continuous, high computing load, noisy objective functions. In: *Faculté des Sciences Appliquées: Université Libre de Bruxelles*) p 219
- [84] Schmidt-Grund R, Ashkenov N, Schubert M M, Czakai W, Faltermeier D, Benndorf G, Hochmuth H, Lorenz M and Grundmann M 2007 Temperature-dependence of the refractive index and the optical transitions at the fundamental band-gap of ZnO *AIP Conference Proceedings* **893** 271-2
- [85] Ou P-C, Liu W-R, Ton H-J, Lin J-H and Hsieh W-F 2011 Ultrafast relaxation and absorption saturation at near exciton resonance in a thin ZnO epilayer *Journal of Applied Physics* **109** 013102-5
- [86] Toshine Y, Takeda J, Ko H J and Yao T 2004 Conversion of an electron-hole plasma into a high density excitonic state in ZnO epitaxial thin films *physica status solidi (c)* **1** 839-42
- [87] Heiss M, Conesa-Boj S, Ren J, Tseng H-H, Gali A, Rudolph A, Uccelli E, Peiró F, Morante J R, Schuh D, Reiger E, Kaxiras E, Arbiol J and Fontcuberta i Morral A 2011 Direct correlation of crystal structure and optical properties in wurtzite/zinc-blende GaAs nanowire heterostructures *Physical Review B* **83** 045303
- [88] Lim S K, Brewster M, Qian F, Li Y, Lieber C M and Gradedčak S 2009 Direct Correlation between Structural and Optical Properties of III-V Nitride Nanowire Heterostructures with Nanoscale Resolution *Nano Letters* **9** 3940-4
- [89] Hendry E, Koeberg M and Bonn M 2007 Exciton and electron-hole plasma formation dynamics in ZnO *Physical Review B* **76** 045214
- [90] Chan Y-P, Lin J-H, Hsu C-C and Hsieh W-F 2008 Near-resonant high order nonlinear absorption of ZnO thin films *Opt. Express* **16** 19900-8
- [91] Dong Z-W, Zhang C-F, You G-J, Qiu X-Q, Liu K-J, Yan Y-L and Qian S-X 2007 Multi-photon excitation UV emission by femtosecond pulses and nonlinearity in ZnO single crystal *Journal of Physics: Condensed Matter* **19**
- [92] Vivas M G, Shih T, Voss T, Mazur E and Mendonca C R 2010 Nonlinear spectra of ZnO: reverse saturable, two- and three-photon absorption *Opt. Express* **18** 9628-33

- [93] Versteegh M A M, Kuis T, Stoof H T C and Dijkhuis J I 2011 Ultrafast screening and carrier dynamics in ZnO: Theory and experiment *Physical Review B* **84** 1-19
- [94] Morkoç H and Özgür Ü 2009 *Zinc Oxide: Fundamentals, Materials and Device Technology*: Wiley-VCH)
- [95] Zhang Wei-li, Chai Lu, Xing Qi-rong, Wang Qing-yue, K. S. Wong, Ping Yu, H. Wang, Tang Z K and Wong G K L 1999 Femtosecond Time-Resolved Exciton Recombination Dynamics in ZnO Microcrystallite Thin Films at Room Temperature *Chinese Phys. Lett.* **16** 728-30
- [96] Hvam J M 1974 Exciton Interaction in Photoluminescence from ZnO *physica status solidi (b)* **63** 511-7
- [97] Zhang J Z 2000 Interfacial Charge Carrier Dynamics of Colloidal Semiconductor Nanoparticles *The Journal of Physical Chemistry B* **104** 7239-53
- [98] Richters J P, Kalden J, Gnauck M, Ronning C, Dietrich C P, Wenckstern H v, Grundmann M, Gutowski J and Voss T 2012 Modal gain and its diameter dependence in single-ZnO micro- and nanowires *Semiconductor Science and Technology* **27** 015005
- [99] Walsh A, Da Silva J L F and Wei S-H 2008 Origins of band-gap renormalization in degenerately doped semiconductors *Physical Review B* **78** 075211
- [100] Knox W H, Hirlimann C, Miller D A B, Shah J, Chemla D S and Shank C V 1986 Femtosecond Excitation of Nonthermal Carrier Populations in GaAs Quantum Wells *Physical Review Letters* **56** 1191-3
- [101] Ulbrich R 1973 Energy Relaxation of Photoexcited Hot Electrons in GaAs *Physical Review B* **8** 5719-27
- [102] Ichida H, Kanematsu Y, Mizoguchi K, Kim D and Nakayama M 2007 Energy-relaxation dynamics of photogenerated excitons observed from time-resolved photoluminescence of exciton-exciton scattering in CuI thin films *Physical Review B* **76** 085417
- [103] Lelyakov A V 1965 Effect of Exciton–Exciton Interaction on the Free Exciton Absorption and Luminescence Spectra of Si and CdS Crystals under High Intensity Excitation *physica status solidi (b)* **65** 359-72
- [104] Chen W, McLendon G, Marchetti A, Rehm J M, Freedhoff M I and Myers C 1994 Size Dependence of Radiative Rates in the Indirect Band Gap Material AgBr *Journal of the American Chemical Society* **116** 1585-6
- [105] Wang Y, Wang Y, Wang Y, Huang K, He T and Liu F-C 1994 Optical absorption enhancement of CdS nanometer crystallites *Spectrochimica Acta Part A: Molecular Spectroscopy* **50** 2203-13
- [106] Li M, Xing G, Ah Qune L F N, Xing G, Wu T, Huan C H A, Zhang X and Sum T C 2012 Tailoring the charge carrier dynamics in ZnO nanowires: the role of surface hole/electron traps *Physical Chemistry Chemical Physics* **14** 3075-82

- [107] Ou P-C, Lin J-H, Chang C-A, Liu W-R and Hsieh W-F 2010 Thickness effect on ultrafast thermalization of carriers in above-band-gap states in ZnO epitaxial films *Journal of Physics D: Applied Physics* **43** 495103
- [108] Cook C J, Khan S, Sanders G D, Wang X, Reitze D H, Jho Y D, Heo Y W, Erie J M, Norton D P and Stanton C J 2010 Ultrafast carrier relaxation and diffusion dynamics in ZnO. In: *Oxide-based Materials and Devices*, (San Francisco, California, USA: SPIE) pp 760304-14
- [109] Kawasaki M, Ohtomo A, Ohkubo I, Koinuma H, Tang Z K, Yu P, Wong G K L, Zhang B P and Segawa Y 1998 Excitonic ultraviolet laser emission at room temperature from naturally made cavity in ZnO nanocrystal thin films *Materials Science and Engineering: B* **56** 239-45
- [110] Ohtomo A, Kawasaki M, Sakurai Y, Yoshida Y, Koinuma H, Yu P, Tang Z K, Wong G K L and Segawa Y 1998 Room temperature ultraviolet laser emission from ZnO nanocrystal thin films grown by laser MBE *Materials Science and Engineering: B* **54** 24-8
- [111] Adachi S 1989 Optical dispersion relations for GaP, GaAs, GaSb, InP, InAs, InSb, $\text{Al}_x\text{Ga}_{1-x}\text{As}$, and $\text{In}_{1-x}\text{Ga}_x\text{As}_y\text{P}_{1-y}$ *Journal of Applied Physics* **66** 6030-40
- [112] Ross G, Montemezzani G, Bernasconi P, Zgonik M and Gunter P 1996 Strong ultraviolet induced absorption and absorption gratings in BaTiO_3 *Journal of Applied Physics* **79** 3665-8
- [113] Buse K and Bierwirth T 1995 Dynamics of light-induced absorption in BaTiO_3 and application for intensity stabilization *J. Opt. Soc. Am. B* **12** 629-37
- [114] Li J, Li X H, Wu F X, Zhu Y, Wu X and Wang H F 1995 Photorefractive parameters and light-induced absorption in BaTiO_3 *Applied Physics A: Materials Science & Processing* **61** 553-7
- [115] Ramos-Garcia R and Damzen M J 1998 Two-secondary-center modeling of photorefraction and comparison with nanosecond pulse illumination experiments in barium titanate *J. Opt. Soc. Am. B* **15** 2174-84
- [116] Ye P, Blouin A, Demers C, Roberge M-M D and Wu X 1991 Picosecond photoinduced absorption in photorefractive BaTiO_3 *Opt. Lett.* **16** 980-2
- [117] Chi M-j, Dou S-x and Ye P-x 1999 Theoretical study of the intensity dependence of total effective trap density in photorefractive crystals *Acta Physica Sinica (Overseas Edition)* **8** 664
- [118] Jia C H, Chen Y H, Zhou X L, Yang A L, Zheng G L, Liu X L, Yang S Y and Wang Z G 2009 Valence band offset of $\text{ZnO}/\text{SrTiO}_3$ heterojunction measured by x-ray photoelectron spectroscopy *Journal of Physics D: Applied Physics* **42** 095305
- [119] Liang Y, Curless J and McCready D 2005 Band alignment at epitaxial SrTiO_3 -GaAs(001) heterojunction *Applied Physics Letters* **86** 082905-3
- [120] Bhattacharya P 1994 *Semiconductor optoelectronic devices*: Prentice Hall)
- [121] Kyaw A K K, Sun X W, Zhao J L, Wang J X, Zhao D W, Wei X F, Liu X W, Demir H V and Wu T Top-illuminated dye-sensitized solar cells with a room-

- temperature-processed ZnO photoanode on metal substrates and a Pt-coated Ga-doped ZnO counter electrode *Journal of Physics D: Applied Physics* **44** 045102
- [122] McCormick M A, Roeder R K and Slamovich E B 2001 Processing effects on the composition and dielectric properties of hydrothermally derived $\text{Ba}_x\text{Sr}_{(1-x)}\text{TiO}_3$ thin films *Journal of Materials Research* **16** 1200-9
- [123] Glinka Y D, Shahbazyan T V, Perakis I E, Tolk N H, Liu X, Sasaki Y and Furdyna J K 2002 Ultrafast dynamics of interfacial electric fields in semiconductor heterostructures monitored by pump-probe second-harmonic generation *Applied Physics Letters* **81** 3717-9

Erklärung

Hiermit erkläre ich, dass ich diese Arbeit selbständig und ohne fremde Hilfe verfasst, andere als die von mir angegebenen Quellen und Hilfsmittel nicht benutzt und die den benutzten Werken wörtlich oder inhaltlich entnommenen Stellen als solche kenntlich gemacht habe.

Eine Anmeldung der Promotionsabsicht habe ich an keiner anderen Fakultät einer Universität oder Hochschule beantragt.

Snigdhatanu Acharya

Acknowledgement



With immense pleasure and profound sense of gratitude, I take this privilege to express my heart-felt and sincere gratitude towards my supervisor PD Dr. Gerhard Siefert for his invaluable guidance, scientific supervision, critical assessments, patience and his constant support throughout this research work. He had not been just my supervisor but a fatherly figure to whom I could look upon whenever I was down with confidence.

I am also very grateful to all the great people I have had around me during my PhD tenure and who contributed to a fantastic working atmosphere. I would like to thank Dr. Jens Lange who had always been there whenever it came to operating those tricky optical alignments and scientific discussion. Special thanks to Sumedha whose contribution to the work had been invaluable towards getting me started on this project. I would also like to thank Moritz for the help with the AFM measurements and Andrei, Sabitha and Tino for being always there sharing light moments during times of stress. Not to forget are Sabrina and Frau. Otten for the help and support regarding administrative formalities.

I owe sincere and earnest thankfulness to the collaborators of this project Prof. Dr. Marius Grundmann, Dr. Rüdiger Schmidt-Grund and specially Tammo Böntgen for providing the samples for this study and for the help with the XRD, ellipsometry and PL measurements for characterization of the samples.

I take this opportunity to thank Prof. Dr. Heinrich Graener and IMPRS for Nanostructures for providing me with the opportunity to participate in this project. I would also like to thank Prof. Dr. Ralf B. Wehrspohn for his continuous support and encouragement.

I gratefully acknowledge SFB 762 for providing me with the financial assistance during the tenure of my PhD work.

It is a great pleasure to thank all my friends here in Halle for providing a lively and joyful atmosphere during my stay here. I am particularly indebted and thankful to Gaurav who have always stood by my side, particularly during the period of documentation of this work.

A mere expression of gratitude to my mother and my family for bringing me up and giving me strength and values to face and persist in challenges of life would not be enough. I strongly believe that their prayers and wishes have given me the courage and perseverance to carry out this doctoral thesis and all the things that I have accomplished in life till now. I thank them from the bottom of my heart.

And last but not the least I dedicate this thesis to the fond memories of my beloved father. You will be always a part of my breath wherever you may be

Curriculum Vitae

Personal details

Name: Snigdhatanu Acharya
Date of Birth: 24-01-1985
Place of Birth: Tezpur, India
Present Address: Richard Paulick Strasse-13, 06124 Halle (Saale), Germany

Education

2003–2005 B.Sc in Physics, Guwahati University
2005–2007 M.Sc in NanoScience and Nanotechnology, Tezpur University
Master theses:
(i) Synthesis and characterization of ZnO nanoparticles via chemical route
(ii) Fabrication and characterization of ZnO thin films and engineering of its band- gap by Cd incorporation
2007–2008 Research Fellow, ARCI, Hyderabad
Project: Study of photo catalytic activity of titania and silica for self-cleaning surfaces
2008- Present Ph.D Student, Martin Luther University, Halle-Saale
PhD thesis title: Ultrafast charge carrier dynamics of ZnO thin films and BaTiO₃/ZnO heterostructures

Publications and Conferences

- S Acharya, S Chouthe, C Sturm, H Graener, R Schmidt-Grund, M Grundmann and G Seifert, Charge carrier dynamics of ZnO and ZnO-BaTiO₃ thin films, *Journal of Physics: Conference Series*, **210**, 012048 (2010)
- N Y Hebalkar, S Acharya and T N Rao, Preparation of bi-functional silica particles for antibacterial and self cleaning surfaces, *Journal of Colloid and Interface Science*, **364**, 24-30 (2011)
- S Acharya, S Chouthe, C Sturm, H Graener, R Schmidt-Grund, M Grundmann and G Seifert, Charge carrier dynamics of ZnO and ZnO-BaTiO₃ thin films, *International conference on optics of excitons in confined systems 11 (OECS 11), 2009 – Madrid, Spain.*
- S Acharya, S Chouthe, T Böntgen, R Schmidt-Grund, M Grundmann and G Seifert, Ultrafast Dynamics of ZnO and ZnO-BaTiO₃ thin films, *DPG meeting 2011, Dresden, Germany*